UNIVERSITY OF PAVIA
DEPARTMENT OF PHYSICS
M.SCI. PROGRAMME IN PHYSICAL SCIENCES

Irradiation of reconstructed human skin cultivated *in-vitro*: computational dosimetry and preliminary radiobiological evaluations for BNCT studies

Master Thesis of
CLARETTA GUIDI

Supervisor
PROF. SILVA BORTOLUSSI

Co-supervisor
DR. IAN POSTUMA

Academic Year 2018/2019

Contents

Chapter 1

Introduction

1.1 Boron Neutron Capture Therapy

Boron Neutron Capture Therapy (BNCT) is a radiation therapy based on the combined action of low energy neutrons (E $<$ 0.5eV) and a selective uptake of ^{10}B in malignant cells. It is based on the ^{10}B(n,α)^{7}Li reaction, whose cross-section at thermal neutron energies (σ=3840 barns for E_n=0.025eV) is much higher than that of neutron interaction with other elements in biological tissues (Fig. 1.1). The ^{10}B(n,α)^{7}Li reaction occurs with two different branches [1]:

$$\mathrm{n}+{}^{10}\mathrm{B} \;\text{-}\!\!<\; \begin{cases} \alpha + {}^{7}\mathrm{Li}\ (6\%) & \text{Q=2.79MeV; } \mathrm{E}_\alpha\text{=1.78MeV, } \mathrm{E}_{Li}\text{=1.01MeV} \\ \alpha + {}^{7}\mathrm{Li} + \gamma\ (94\%) & \text{Q=2.31MeV; } \mathrm{E}_\alpha\text{=1.47MeV } \mathrm{E}_{Li}\text{=0.84MeV, } \mathrm{E}_\gamma\text{=0.48MeV} \end{cases} \tag{1.1}$$

Both decay branches lead to the production of charged particles with a high average Linear Energy Transfer (LET), that is about 196 $keV\ \mu m^{-1}$ for α particles and about 162 $keV\ \mu m^{-1}$ for ^{7}Li-nuclei [2]. The corresponding

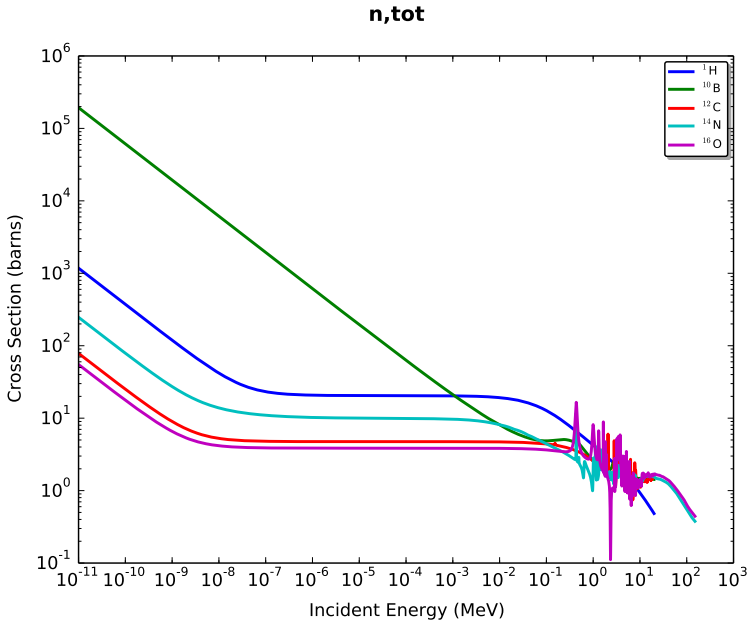

Figure 1.1: Neutron total cross-section for ^{1}H, ^{10}B, ^{12}C, ^{14}N, ^{16}O as a function of neutron energy.

range in tissue (respectively about 9 μm and 5 μm) are comparable with the cell diameter, thus almost all of the energy of these particles is deposited inside the cell where the reaction takes place [1, 3]. For this reason, BNCT selectivity and effectiveness depends on the ability to enrich the tumour with a higher ^{10}B concentration compared to the healthy tissues. This is obtained through the administration of borated compounds to the patient, that must:

- have a low intrinsic toxicity;
- selectively target tumour cells, with tumour/normal tissue and tumour/blood boron concentration ratios preferably higher than 3;
- be expelled relatively quickly from blood and normal tissues, while persisting in tumour for at least the duration of the irradiation [3, 4].

Boron carriers that currently match these requirements are BPA (boronophenylalanine) and BSH (sodium borocaptate) [1]. BPA is a precursor of melanine and in fact it was used for the first time in the treatment of melanomas by Mishima et al. [5, 6]. For the same reason it is also easily absorbed by normal skin. These boron compounds have been approved for clinical use

in different protocols worldwide, with BPA being currently the most used. The work described in this thesis focuses on the effects of BPA-mediated BNCT in normal skin, which is the organ that can limit the dose delivery to the tumours, especially for the deep-seated ones, which require epithermal neutron beams. Epithermal neutrons modearate to lower energies while crossing the patient body, reaching the tumour with thermal energy at which the neutron capture has the highest cross section. Skin is the first layer of tissue absorbing the neutron beam: epithermal neutrons lose their energy by elastic scattering in hydrogen, thus depositing dose. Moreover, the higher boron uptake comparing to other normal tissues, makes neutron capture in boron another source of dose that may damage normal skin. For this reason, dose to skin must be accurately calculated and kept below the tolerance level to avoid side effects.

The other fundamental element for BNCT is the neutron beam, which can be obtained by research nuclear reactors or by particle accelerators. This latter option is currently becoming available, with many facilities being build worldwide. Accelerator Based-BNCT (AB-BNCT) relies on coupling a proton or deuteron beam to a proper target, to obtain neutrons by nuclear reactions such as: $^{7}Li(p,n)^{7}Be$ or $^{9}Be(d,n)^{10}B$. This technology presents many advantages over the reactor-based BNCT, for example it can be installed in hospitals, being smaller and requiring simpler licensing, operation and maintenance [7]. Neutrons produced at the target are then moderated to obtain two kinds of clinical beam, which differ by their mean neutron energy: thermal (25 meV) and epithermal ($\approx$1 keV). Thermal neutron beams are used to treat only shallow tumours, such as skin melanoma, epithermal neutron beams are used to generate a uniform thermal neutron field deeper into the tissue [8], being thus able to treat deep-seated neoplasms.

The high selectivity of BNCT makes it a possible therapeutic option for some malignancies, in particular disseminated or infiltrated cancer. These cases are often impossible to be surgically removed and/or to be treated with other types of radiotherapy, because the tumour target is not localized, too close to a radiosensitive organ, or not discernible from the surrounding normal tissue. The selective effect of BNCT is based on the biological targeting of the boron drug: it is possible to irradiate a large volume and hit neoplastic cells even when the precise position of these is not known [9]. For this reason, BNCT is the only radiotherapy technique that can be applied to metastatic spreads.

1.2 Dosimetry in BNCT

As for all the radiotherapy methods, the safety and effectiveness of the BNCT treatment are determined by the capacity of calculating the dose deposited in tissue with high accuracy. In BNCT treatment planning the dose prescription is set to the most radiosensitive tissue/organ involved in the irradiation, fixing the irradiation time to reach this dose. The dose absorbed in tumour is normally higher, due to higher boron uptake in cancerous cells. Dose calculation in BNCT is not trivial, due to the mechanisms of neutron energy release, producing a mixed radiation field in the biological tissue. Each radiation component has its own characteristics and, hence, its own effectiveness in producing biological damage.

The deposition of energy in tissue by epithermal and fast neutrons is mainly due to hydrogen recoil nuclei, with whom neutrons interact by elastic scattering $^{1}H(n,n')^{1}H$. When scattered, neutrons loose energy, leading to neutron thermalization with depth. Consequently, when irradiating with an epithermal neutron beam, the spectrum is harder in the superficial layers of tissues while it is thermal in the inner depth. This ensures that the probability of neutron capture in boron is maximised at the tumour depth. At thermal energy, in fact, neutrons mainly interact by capture reactions. Taking the tissue atomic composition shown in Table 1.1, the most relevant capture reactions are: $^{1}H(n,\gamma)^{2}H$, $^{14}N(n,p)^{14}C$, $^{16}O(n,\gamma)^{17}O$, $^{17}C(n,\gamma)^{18}C$ and $^{14}N(n,\gamma)^{15}N$. Among these, only the first two induce a significant energy deposition; the others have low cross-sections or occur in isotopes with low abundance in tissues [10]. The hydrogen capture produces a 2.2 MeV photon that deposits its energy far from the production site, whereas the nitrogen capture leads to a 0.583 MeV proton that, together with the 42 keV recoil ^{14}C, produces a local deposition of dose [10].

Hydrogen recoil collisions and neutron capture reactions in H and N produce an unavoidable and non-selective dose delivery during BNCT treatment, affecting both healthy and tumour tissue. The selective dose component consists, instead, of the energy released by the α and lithium ion generated from the $^{10}B(n,\alpha)^{7}Li$ reaction. As said before, these particles deposit energy locally due to their high LET. Thanks to its high cross-section, the $^{10}B(n,\alpha)^{7}Li$ reaction constitutes the most relevant dose component even with small ^{10}B amounts: typical boron concentration obtained in tissues are of the order of

Element	Fraction in tissue (%)
$^{16}_{8}$O	63
$^{12}_{6}$C	23
$^{1}_{1}$H	10
$^{14}_{7}$N	2.3
Others: ($^{23}_{11}$Na, $^{31}_{15}$P, $^{32}_{16}$S, Cl natural, K natural)	1.7

Table 1.1: Tissue composition from ICRU 46 report [11]. Density ρ=1.06$\frac{g}{cm^3}$.

tens of micrograms of ^{10}B per gram of tissue (ppm).

Another source of unavoidable background dose comes from the structural gamma component in the neutron beam, which should be kept as low as possible by using proper shielding materials.

The total dose is the sum of these contributions, each to be calculated in the tumour and in the normal tissues involved in the irradiation. However, as said above, each component has a different LET, thus a different radiobiological effect in tissue.

To summarise, the main physical dose components are:

- D_F = dose from fast neutrons, mainly due to recoil protons from $^1H(n,n')^1H$ scattering;

- D_T = dose from thermal neutron, mainly due to protons and ^{14}C from the $^{14}N(n,p)^{14}C$ reactions;

- D_B = dose from the $^{10}B(n,\alpha)^7Li$ reactions due to alpha and litium nuclei.

- D_γ = dose from background photons and from $^1H(n,\gamma)^2H$ reactions.

The clinical radiotherapy with photons allows the analysis of outcome as a function of the administered dose. It is thus extremely important to express the mixed-field BNCT dose in photon-equivalent units, to compare the treatment planning with conventional photon therapy, enabling predictions on the effects of the irradiation. The way in which BNCT dose has been compared with conventional photon irradiation, consists in multiplying the absorbed

dose component (in Gy) by the correspondent Relative Biological Effectiveness (RBE) or the Compound Biological Effectiveness (CBE) factor, leading to the *biological weighted total dose*, expressed in Gray-equivalent (Gy-Eq) [2].

The RBE factor is defined as the ratio between the absorbed dose due to reference photon radiation and the dose of the radiation under study necessary to cause the same biological endpoint. The CBE factor is the same as RBE, but it refers to the dose component of boron. The boron dose, in fact, also depends on the boron distribution at sub-cellular level obtained with a chosen boron carrier [2]. Both RBE and CBE factors have been considered as dose independent, dose rate independent and they are calculated at fixed endpoints, for example at 1% of cell survival in *in-vitro* experiments [2]. Thus the total biologically weighted dose D_w (in Gy-Eq) is:

$$D_w = RBE_F \cdot D_F + RBE_T \cdot D_T + CBE \cdot D_B + D_\gamma \tag{1.2}$$

This method to convert absorbed dose into biological dose is however a simplification, especially because the RBE and CBE factors are calculated at a fixed endpoint. In 2012 González and Santa Cruz proved that RBE-weighted dose does not explain the BNCT outcome when compared to the conventional photon radiotherapy [12]. In particular, it leads to overestimate tumour dose. This generates the situation in which even very high single-fraction doses do not lead to tumour control, as expected from tumour control probability observed from photon radiotherapy. They developed a more accurate model that calculates *photon iso-effective dose*, expressed in Gy(IsoE), defined as the photon dose that produces the same effect (such as tumour control probability or normal tissue complication probability or cell survival) as a given combination of the dose components of BNCT [13]. In case of cell survival data, the model uses the entire survival curve instead of choosing an arbitrary value, also considering the first-order repair of sub-lethal lesions mechanism (by means of the Lea-Catcheside time factor) and synergism between the different radiation components [12, 14].

Improvements in dose calculation lead to better treatment plans, able to maximise the tumour damage while limiting as much as possible the dose absorbed by healthy tissues. To this end, it is important to develop accurate models, relying on robust radiobiological data. In particular, *in-vivo* models can be used to build Tumour Control Probability (TCP) and Normal Tissue

Complication Probability (NTCP), respectively. Tumour cell cultures are employed to build curves of cell survival as a function of the dose. In general, more experimental data are needed especially for healthy tissues, which limit the irradiation time. For these, a cell survival study is less meaningful, because it is difficult to associate a specific adverse effect to the percentage of killed cells. In fact, normal tissue effects depend on complex physiological mechanisms and interaction between different cells types and structures that are not present in a mono-layer cell culture.

In this work, an innovative biological model has been used to obtain data on the BNCT effects on human healthy skin, starting from tissue cultivated *in-vitro*.

1.3 Skin and SkinEthic^{TM} RHE model

As anticipated before, normal skin represents one of the main organ at risk during a BNCT irradiation. Epithermal energy neutrons, which thermalise in its depth, loose about half of their energy in each scattering interaction with hydrogen nuclei. Moreover skin absorbs ^{10}B, so the dose component due to the $^{10}B(n,\alpha)^{7}Li$ reaction constitutes an important fraction of the total dose. In particular, when BPA is used as boron carrier, skin uptakes a concentration 1.5 times higher than in the blood [6, 2, 15]. The skin is one of the major organs of the body. For example, in a standard man of 70 kg it constitutes the 3% of the total body weight and it has a surface area of about 2 m^2. It has a complex structure (Figure 1.2) and many vital functions, such as: immune system, sensory, physical barrier to protect the body, controlling fluids and body thermoregulation [16].

Human skin consist of two major layers: the epidermis, that is the external one, and the dermis. The epidermis is in turn divided into different layers that are, from the deepest to the most superficial one: basal, spinous, granular, stratum lucidum (a layer of dead cells that is present only in palms and soles) and stratum corneum (consisting mostly of dead cells). The epidermis cells are prevalently keratinocytes (90-95%), which proliferate in the basal layer, migrate superficially and differentiate more and more in each layer until their death and accumulation in the stratum corneum. But there are also other types of cells with important functional roles, such as melanocytes (that are in the basal layer and produce melanin), Merkel-Ranvier cells (that contribute to sensory reception) and Langerhans cells (that are in the spinous

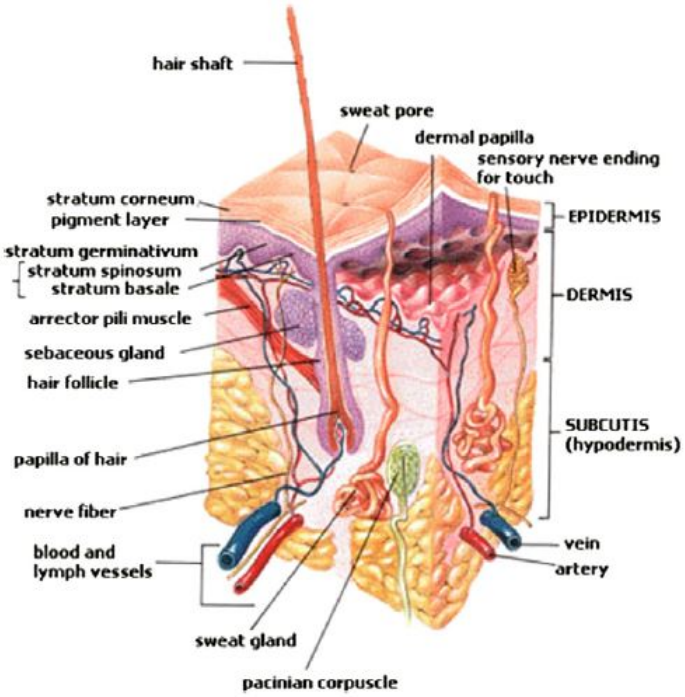

Figure 1.2: Representation of human skin (from [16]).

layer and have immunological functions).

The dermis is composed of two main layers, which are the papillary and the reticular dermis, and it is located between the epidermis and the subcutaneous tissues. The major cells of the dermis are macrophages, adipocytes and fibroblasts, which produce collagens, elastic fibers and other proteins that confer to the skin its flexibility, strength and elasticity [17].

The irradiation effects in skin include erythema, permanent epilation, dry and moist desquamation, dermal necrosis and telangiectasia and they can be observed from a few hours (early erythema) up to 52 weeks post irradiation (telangiectasia or late necrosis) [2, 16]. It is therefore extremely important to understand the normal skin reaction as a function of the absorbed dose, in order to develop an adequate radiobiological model that can predict skin injuries in BNCT treatments.

The work described in this thesis aims at studying skin radiobiological effects by experimental measurements using a model of in-vitro tissue that has never been employed for BNCT research. To obtain a realistic dose response evaluation for the normal skin, we chose the SkinEthic^{TM} Reconstructed Hu-

man Epidermis (RHE) as the radiobiological model. It is a three-dimensional *in-vitro* model of normal epidermal keratinocytes of human derivation, realised by EpiSkin^{TM} laboratory in France, for research purpose only. It consists of different organised layers (basal, spinous, granular and a multilayered stratum corneum), comparable with the *in-vivo* human tissue ones, cultured on a 0.5 cm^2 surface inert polycarbonate filter at the air-liquid interface in a chemically defined medium [18]. The inserts containing tissue models are shipped at room temperature in a multi-well plate filled with an agarose-nutrient solution, that has to be replaced with the SkinEthic Maintenance Medium (SMM), or SkinEthic Growth Medium (SGM), shipped together with the tissues. With every batch, the laboratory provides also a quality control data sheet that includes histology (Figure 1.3), viability and biological safety data.

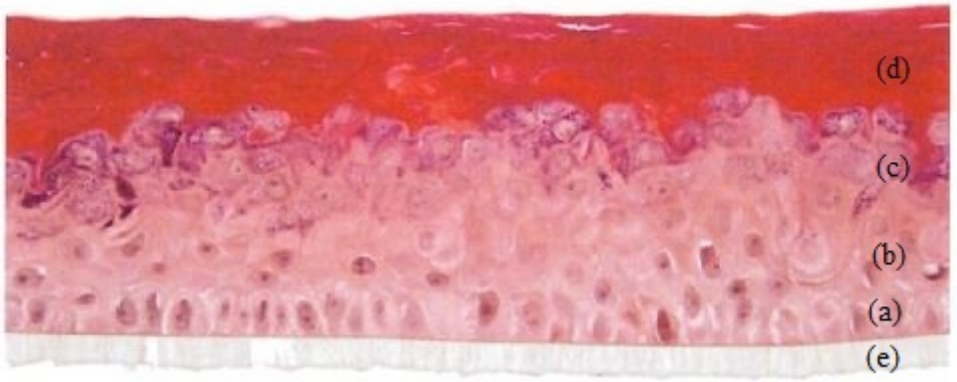

Figure 1.3: Histology of the 17-RHE-094 batch, received for one of the experiments performed in Pavia. The different layers are clearly visible: (a) basal, (b) spinous, (c) granular and (d) corneum and also the filter section (e).

The RHE model was used to study the healthy skin response to the irradiation, applying the well known irradiation protocols of cell cultures [19, 20]. The aim is to obtain dose-effect curves as a function of the absorbed dose, for irradiation with gamma rays (reference radiation type), with neutrons only and with neutrons in presence of boron. For the first evaluations, we have measured the cell viability (measured by MTT assay) and possible morphological or structural changes induced in the tissues samples (studied by histology). For each endpoint, we observed the effects at different times: immediately after the irradiation (T0), after two days (T2), after five days (T5)

and after seven days (T7). Different timing aims at understanding how damages in the skin evolve and become evident as a function of the elapsed time from the irradiation [2]. The chosen model does not allow longer observation times because the life of the RHE is guaranteed only for a week. Another interesting endpoint will be investigated in future studies: the ability of cells to proliferate, that can be assessed by the BrdU assay. In fact, it is more representative of the actual tissue damage because cells that appear alive in the MTT assay may not be able to proliferate, thus dying at the end of their cell cycle. The observation of the hystological sections in comparison with MTT results also help in pointing out this effect.

Irradiation with neutrons took place in the Thermal Column of the TRIGA Mark II reactor of the University of Pavia, at different powers and for different irradiation times, in order to deliver increasing dose. For the irradiation in presence of boron, the absorbed dose depends significantly on the boron concentration present in tissues. For this reason, to make a reliable dose calculation, it is extremely important to measure the ^{10}B concentration present in tissue in each irradiation experiment. We have measured boron concentration by neutron autoradiography technique. The same technique was employed to obtain imaging of boron distribution in the samples. Absorbed dose was calculated by Monte Carlo simulations of the irradiated set-up by the radiation transport code MCNP. Particular care was devoted to the assumptions made for the dose computation. In fact, mixed-field dose calculation is not trivial, due to the complexity of the geometry, and to the small volume of the tissue samples. This could imply that charged particle equilibrium, often assumed to calculate dose by multiplying fluence by kerma factors, does not hold in this situation. Irradiation with a reference photon source took place at the San Matteo Polyclinic, using an X-Ray blood irradiator equipped with two photon beams of average energy between 60 and 80 keV. Dosimetry was accurately studied also in this set-up to assess the correction factor between the nominal dose given by the calibration procedures and the actual dose absorbed in tissues.

The thesis is divided into five main chapters, besides this Introduction. Chapter 2 describes the boron administration method, the boron concentration measurements and the imaging of boron distribution in RHE samples. Chapter 3 and 4 are dedicated to computational dosimetry, which assesses the dose rates absorbed by RHE samples in the different irradiation config-

urations. Details are given about the transport strategies adopted to make the calculations more efficient and more accurate. Chapter 5 shows the preliminary radiobiological results of MTT tests and hystological evaluations as a function of the dose. Chapter 6 briefly summarises the work and outlines the future perspectives of this research.

Chapter 2

Boron measurements

A representative radiobiological response to the BNCT dose depends on the possibility to obtain a ^{10}B distribution as uniform as possible in the SkinEthic^{TM} Reconstructed Human Epidermis (RHE). In fact, with non-uniform distributions it is difficult to establish a correlation between the observed effects and the absorbed dose. Moreover, clinical practice with BPA showed that boron distribution is substantially homogeneous in normal tissues. As described in Chapter 1, RHE is a three-dimensional model composed by well differentiated cells, thus it is very different from the mono-layer cell cultures in which boron administration protocols have been optimised so far, in Pavia and elsewhere. Starting with a new model required to investigate the BPA treatment protocols, i.e. the optimal contact time and administration modality. BPA solution is obtained by combining ^{10}B-enriched, L-isomer BPA with a 10% molar excess of fructose in water [21]. The pH is raised to 9.5–10 with NaOH, the mixture is stirred, and after a few minutes, adjusted to 7.4 with HCl. The solution thus obtained is mixed to the culture medium, according to the initial ^{10}B concentration desired for the experiment. Normally RHE samples grow in a set-up where culture medium stays below the surface of the tissues. However, it is possible to expose the samples in a configuration that allows RHE to be surrounded by the culture medium. The two different configurations to be tested are: medium reaching the tissue through the polycarbonate filter only (*bottom*) and both through the filter and the stratum corneum (*bottom/top*), as shown in Fig.2.1. Although the former solution is more similar to what occurs in patient (boron uptake through blood supply), our purpose here was to obtain a uniform distribution for the irradiation. It is in fact very difficult (and not meaningful for our purpose)

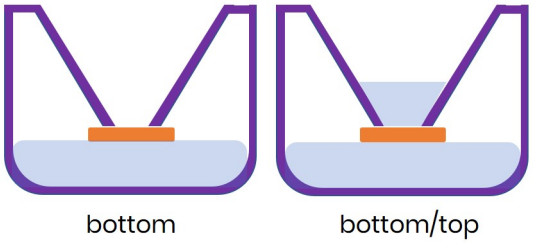

Figure 2.1: Scheme of the *bottom* and *bottom/top* administration protocols. The walls of the multi-well and of the RHE holder are represented in purple, RHE samples in orange and medium enriched with boron in pale blue. Elements are not to scale.

to mimic precisely the supply of drugs to skin through blood circulation in this very simplified model.

At the end of the contact time with the BPA enriched medium, treated samples are washed twenty times with PBS in order to remove boron that has not been internalised and that may remain on the surface of the tissue. Measurements of ^{10}B concentration in the RHE samples were performed by the neutron autoradiography technique, that allows obtaining qualitative and quantitative results.

2.1 Neutron autoradiography

Neutron autoradiography is a non-destructive technique based on the structural damage that charged particles induce along their tracks in a Solid State Nuclear Track Detector (SSNTD). For boron concentration measurements, samples are irradiated in a thermal neutron field in contact with the detector; the neutron capture reactions in boron produce charged particles that cause the damage in the sensitive film. After the irradiation the tracks are latent (not visible), but a proper etching solution at a given temperature corrodes the detector more intensively in the damaged regions, i.e. along the particle tracks. In this way, tracks are chemically enlarged and can be photographed with an optical microscope. This method is used for qualitative and quantitative boron concentration measurements in biological samples. In our case, images are achieved by coupling a SSNTD called CR-39 (polyallyldiglycol carbonate, 75mm x 20mm of area and 0.5mm thick) to a biological

sample (Figure 2.2) and subsequently irradiating the system in the thermal column of the Triga Mark II reactor at LENA (University of Pavia). Tracks in the SSNTD are produced mainly by charged particles derived from the neutron capture reaction in ^{10}B, produced inside the biological sample. The amount of alpha particles and lithium ions reaching the detector will determine the kind of analysis. For quantitative analysis tracks must be well separated, to allow the counting of the tracks per unit area using a dedicated software. The track density is then correlated to the concentration of ^{10}B through a calibration curve. This curve was obtained using standard samples with different known boron concentrations, providing the track density ($tracks/mm^2$) as a function of boron concentration in ppm ($\mu g/g$). For quantitative boron concentration analysis, samples are exposed to a thermal neutron fluence of $2{\cdot}10^{10}$ cm^{-2} [22, 23].

To obtain boron distribution imaging, samples are irradiated with a thermal fluence of $2.5{\cdot}10^{12}$ cm^{-2}. In this way, tracks overlap to form a map of areas with lower and higher ^{10}B concentration in grey shades [24]. Total neutron fluence is not the only difference between qualitative and quantitative neutron autoradiography. In the first case the irradiated CR-39 is etched in a PEW40 solution [1] at 70°C for 10 minutes and then rinsed with water. For imaging, the CR-39 is etched for 20 minutes in a 6.25M NaOH solution at 70 °C. Figure 2.3 is a picture of the thermostatic bath were the chemical etching is carried out.

After irradiation and etching, image are acquired with a LEICA MZ16A microscope connected to a lamp (LEICA CLS150X), a PRIOR OPTISCAN II xy stage and a LEICA DMC4500 camera, as shown in Figure 2.4. The entire system is connected to a PC and the software for analysis is Image Pro Plus 7, capable of acquiring images and calibrating the stage movement, enabling the automatic sampling of different areas of the CR-39 [23].

For qualitative neutron autoradiography the image of the entire sample is taken for analysis. For quantitative autoradiography, a representative portion of the sample is imaged (approximately 12 mm^2). This area of interest is scanned to take 40 (8x5) sequential pictures, where track density is measured. From this density, boron concentration is computed through the calibration

[1] PEW40 in mass percentages: 15% KOH + 40% $C_2H_6O_2$ + 45% H_2O

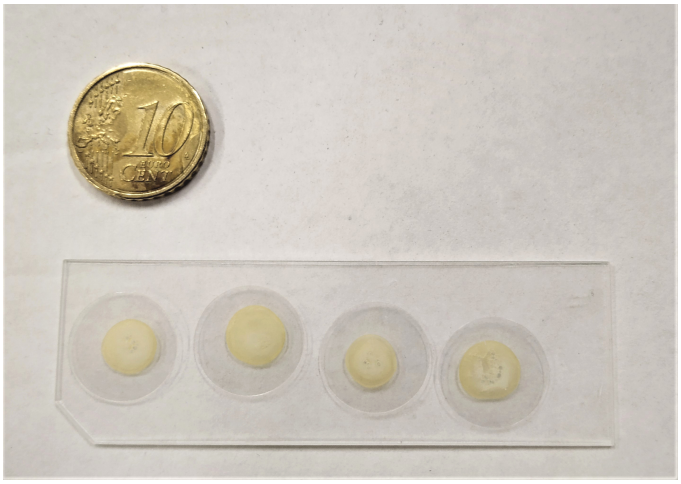

Figure 2.2: Example of samples onto the CR-39 film detector.

Figure 2.3: The sensitive films are immersed in the etching solution (PEW or NaOH for qualitative and quantitative autoradiography respectively) at a constant temperature in a thermostatic bath. The picture shows the set-up used in the described experiments.

(a)

(b)

Figure 2.4: Image acquisition set-up: a) the entire acquisition equipment. b) picture of the Leica microscope.

curve obtained by Postuma et al. [23]. As the calibration was obtained in cell samples, it is necessary to take into account that tissues could lose different percentages of water when drying. In fact, fresh-to-dry mass ratio is an important factor that normalises the boron concentration measured in dried samples to their original mass [22, 23]. In the case of SkinEthic^{TM} RHE, the dry to fresh ratio was measured: 0.30 ± 0.01. With this set-up the average boron concentration within the scanned area and the distribution of boron in RHE were obtained.

2.2 RHE irradiation and sample preparation protocol

As shown in Chapter 1, RHE is more complex than the common cell pellets irradiated for boron uptake measurements. The described techniques have been optimised for this new model and used to choose the best boron administration route.

First of all, control samples without boron treatment were analysed, to point out a possible ^{10}B background in tissue or in the polycarbonate filter. No contamination was observed: the boron concentration was below the detection limit (1 ppm) and the images were indistinguishable from the

background, for this reason it is not meaningful to report them here.

RHE has a variable thickness, approximately between 100 and 150 μm. Consequently, not all alpha particles and lithium ions emerge from the tissue sample during neutron irradiation. Only particles coming from a depth equal to the range of alpha particles can reach the detector. Thus, the measurement points out ^{10}B present in a layer of approximately 30-40 μm in the dried sample corresponding to approximately 10 μm in the fresh RHE. Since the samples are constituted by different cell layers, that may uptake different boron concentration, it was interesting to obtain neutron autoradiography of both sides. However, one side of the RHE is constituted by biological material (stratum corneum), while on the other side RHE is attached to the polycarbonate filter. It was thus important to explore the quality of images according to the side of the sample laid on the CR-39 film. Images where obtained by sandwiching RHE between two CR-39 as shown in Fig. 2.5. In this way, as shown in Section 2.2.1, it was possible to determine whether the filter influences the capacity to measure boron, i.e. if it stopped the charged particles coming from the tissue. Once this issue was settled, we optimised the boron administration protocol, by evaluating if boron uptake was more homogeneous when RHE was put in contact with BPA trough the polycarbonate filter (*bottom*) or both trough the filter and external part of the skin sample (*bottom/top*), as shown in Section 2.2.2. Finally, in Section 2.2.3, the optimal contact time was evaluated, by subjecting different RHE samples to variable contact times with the boron enriched medium.

2.2.1 RHE position on the CR-39

To study the quality of the images according to their position with respect to CR-39, RHE samples were exposed for 4 hours to the culture medium enriched with 80 ppm (i.e. 80 micrograms of ^{10}B per gram of medium) of boron[2], with the medium reaching the tissue through the filter and through the stratum corneum. Then, to evaluate the effects of the polycarbonate layer on the measurement of boron uptake, the samples were sandwiched between two CR-39s for the irradiation, as shown in Figure 2.5. Both qualitative and quantitative analysis were performed.

[2]This is the standard protocol applied in monolayer cell cultures.

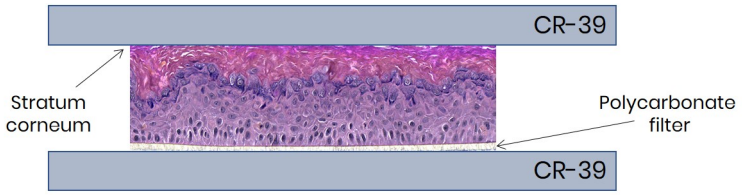

Figure 2.5: Scheme of sample positioning on the CR-39s. Elements are not to scale.

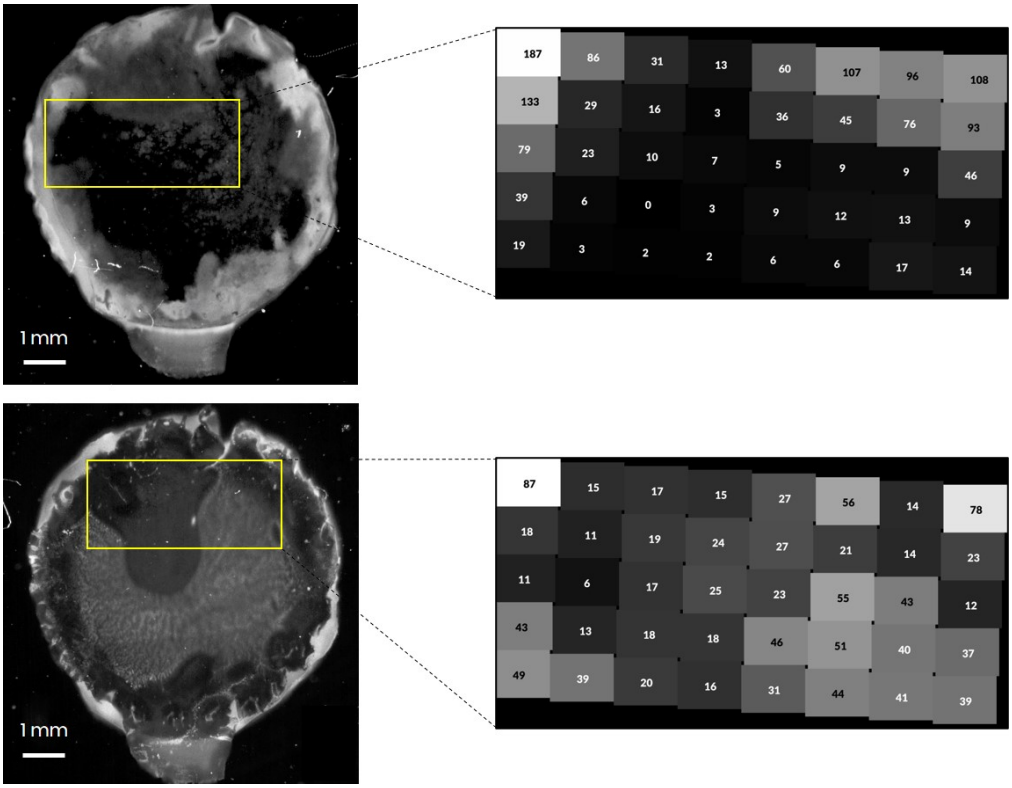

Figure 2.6: Top: sample facing the CR-39 with the polycarbonate filter. Left: qualitative image, right: quantitative measurement of a portion of the sample. The portion scanned to take pictures is highlighted in yellow in the qualitative image. Each rectangle in the right picture represents the number of tracks measured in each picture taken. Bottom: sample facing the CR-39 with the RHE stratum corneum. Left: qualitative image, right: quantitative measurement of a portion of the sample.

Figure 2.6 shows the results of imaging (left) and boron quantification (right), analysing the two sides of a representative RHE sample. The right part of the picture represents the area in which the 80 pictures were taken, and the numbers are the number of tracks counted for each picture. Clearer rectangles correspond to a higher number of tracks. On the top, the qualitative neutron autoradiography image of the CR-39 facing the polycarbonate filter is shown together with the respective track analysis. Boron is more concentrated along the edges of the RHE sample, while in the central part there is apparently no uptake (dark areas on the left and very few tracks detected in the central rectangles on the right). On the bottom part of the Figure, the qualitative neutron autoradiography of the CR-39 facing the stratum corneum is shown together with the respective track analysis. In this case, boron is clearly visible also in the central part of the sample (clearer areas on the left and more tracks in the rectangles on the right). The images show that, although charged particles can reach the CR-39 through the polycarbonate filter, the best resolution and the best quality of information is obtained by laying the stratum corneum on the CR-39. For this reason, we adopted this set-up to get a better representation of boron distribution in RHE tissues.

To better represent the boron distribution in the sample, quantitative analysis by track density measurement in the whole tissue area can be transformed into colour-map images. Figure 2.7 is the map of boron distribution measured in the sample shown in Figure 2.6, with the stratum corneum laid on CR-39. Yellow areas correspond to parts of the sample taking up higher boron concentrations.

2.2.2 Boron administration protocol

Once fixed the positioning of RHE on CR-39, the BPA administration protocol was studied. In particular, BPA was administered in the normal cultivation set-up with the enriched medium below the surface (*bottom*), or medium reaching the tissue through the filter and through the stratum corneum (*bottom/top*) as previously shown in Fig.2.1.

All the samples were exposed for 4 hours to the culture medium containing a boron concentration of 80 ppm. Qualitative and quantitative analysis were performed.

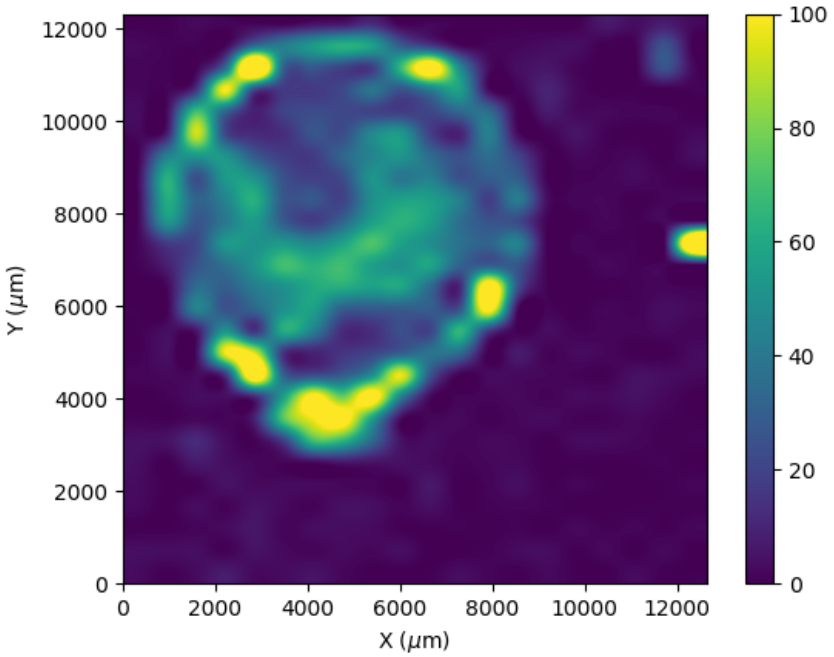

Figure 2.7: colour map of the track density measured in each picture of the image shown in Figure2.6, bottom. The high boron concentration in some part of the sample edges corresponds to yellow spots.

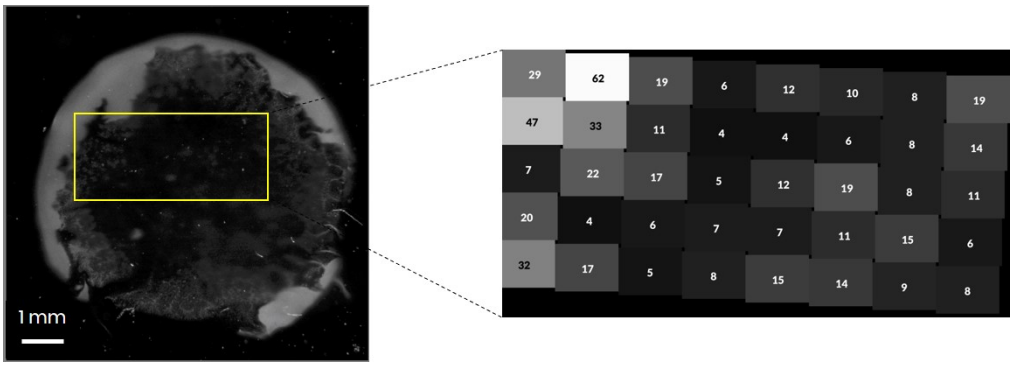

Figure 2.8: Sample treated with borated medium with the *bottom* protocol. Left: qualitative image, right: track analysis.

Figure 2.8 shows the qualitative and quantitative neutron autoradiography images of a representative sample treated with the *bottom* protocol, while the *bottom/top* configuration was shown above (Fig. 2.6). The *bottom/-top* protocol was confirmed the one that guarantees a more uniform boron distribution in the RHE sample, and also a higher average track density, corresponding to a higher boron uptake. Therefore, the BPA administration route chosen for the experiments is the *bottom/top* protocol.

2.2.3 BPA contact time

Using the best irradiation (CR-39 facing RHE stratum corneum) and administration (*bottom/top*) protocols, two exposure time to BPA were studied: 4 hours and 24 hours. The first exposure time was selected because it is the standard time used for cell cultures treatment; 24 hours is the longest possible exposure to have a viable RHE sample for studies going up to 7 days. Figure 2.9 shows a representative RHE sample exposed to BPA-enriched medium for 24 hours. With respect to the sample exposed to BPA for 4h, shown in Figure 2.6, the differences in boron distribution within the sample are negligible. In particular, the differences are very low in the central portion of the samples. In this experiment, the average boron uptake after 24h was 30±5 ppm, while for the 4 hours treatment it was 35±5 ppm. Consequently, we decided to use the 4 hours administration protocol to limit the treatment time and maximise the follow up time.

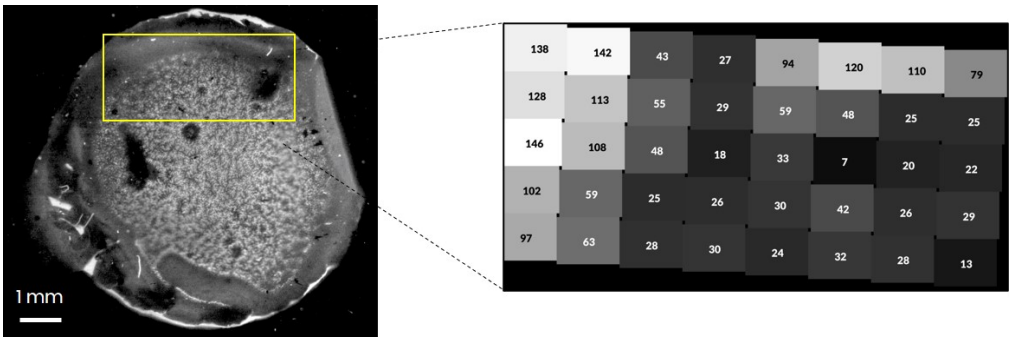

Figure 2.9: Sample exposed to BPA-enriched medium for 24 hours. Left: qualitative image, right: track analysis.

In these preliminary measurements it was observed that the peripheral parts always uptake more boron than the centre. This is probably due to the intrinsic structure of the edges, which will be further discussed in Chapter 5. Anyway, the region of interest of the sample is the central part, which better models the human skin structure.

2.3 Boron measurements in irradiation experiments

The previous section describes the study carried out to optimise the experimental conditions. This assessment has enabled the boron measurement in the second phase of the experiment, i.e. the irradiation of tissue samples to measure the effects as a function of the dose. As said in Subsection 2.2.3, boron concentration in the same RHE samples is never completely uniform for many reasons. Moreover, biological variability affects boron uptake in samples, especially if they belong to different batches. Boron uptake variability is extremely important even in patients treated with BNCT. In modern clinical trials, tumour to normal tissue boron concentration ratio is evaluated before the irradiation by means of ^{18}F-labelled BPA combined by Positron Emission Tomography (PET) [25, 26]. It is well known that healthy and tumour tissues of different patients, even though of the same type, do not respond in the same way to BPA administration. Each RHE batch derives from a different donor, and this constitutes a possible cause of boron uptake variability.

Experiment number	Average ^{10}B concentration (ppm)
1	53 ± 4
2	47 ± 9
3	12 ± 1
4	39 ± 1

Table 2.1: Average boron concentrations measured for each irradiation experiment performed.

Therefore, while preliminary experiments as those described above showed that there are no relevant differences in boron uptake in the same batch, average boron concentration in tissues belonging to different batches could vary. For this reason, boron concentration in samples was measured for all the irradiation experiments: three RHEs per batch were dedicated to this purpose each time. They underwent the same administration protocol of other tissues but, instead of being irradiated, they were left to dry and underwent qualitative and quantitative neutron autoradiography. Quantitative results were averaged over the three samples and considered representative of the boron concentration in the irradiated samples. Average boron concentration for each batch are reported in Table 2.1.

Results in Table 2.1 show that average boron concentration in samples belonging to different batches can vary by up to 300%. Since boron concentration measurements could not be performed before samples irradiation and since they present this strong variability, it was difficult to chose the adequate reactor power and irradiation time necessary to obtain dose points regularly spaced to build the dose-effect curves. Therefore, some assumption were made. First, for each irradiation session, boron concentration in RHEs were supposed on the basis of the measurements gradually acquired. Then, for each experiment, the most suitable combination of irradiation time and reactor power was chosen to provide potentially well-distanced dose-effect points.

Table 2.1 clearly shows that it is not possible to assume that RHEs always absorb the same average amount of boron, even if subjected to the same administration protocol. Such assumption would lead to estimates of the dose quite unreliable. Therefore it must be stressed the necessity to measure the real ^{10}B mean concentration in samples for each experiment performed. The same variability had been previously observed in other *in vitro* experiments

with mono-layer cell cultures. Also in that case, it is crucial to measure boron concentration in cells cultivated in the same conditions as the one that undergo neutron irradiation.

Chapter 3

Calculation of absorbed dose - neutron irradiation

The dose absorbed by SkinEthic^{TM} RHE models during neutron and photon irradiation was calculated by Monte Carlo simulations, employing the MCNP6 code (version 6.1 [27]). MCNP simulation allows reproducing the whole experimental set-up and calculating the dose in the desired volume by following each particle in its interactions and energy deposition. Moreover, it is possible to separate the different contributions to the quantity of interest, particularly important in the case of mixed field dosimetry. To correctly interpret the simulation results, it is necessary to understand the approximations assumed in each calculation strategy. These approximations range from the accuracy of the geometrical and material model, to the precision of the transport of the secondary radiation. For example, if only the primary radiation is transported, MCNP deposits the energy of the secondary particles in the point where they are created, causing a possible overestimation of the dose. In many cases it is impossible to transport all secondaries because this would require an extremely long computation time. To optimise the transport strategy and the type of calculation, it is necessary to analyse the problem of interest, in particular its geometrical dimensions and the interactions occurring at the energies involved.

For the dosimetry of RHE neutron irradiation, the whole reactor geometry with the tissues in irradiation positions was modelled with MCNP. The efficiency of the calculation was improved through the implementation of variance reduction techniques, to obtain statistically meaningful results while reducing the calculation time. The quantities to be scored (*tallies*) were se-

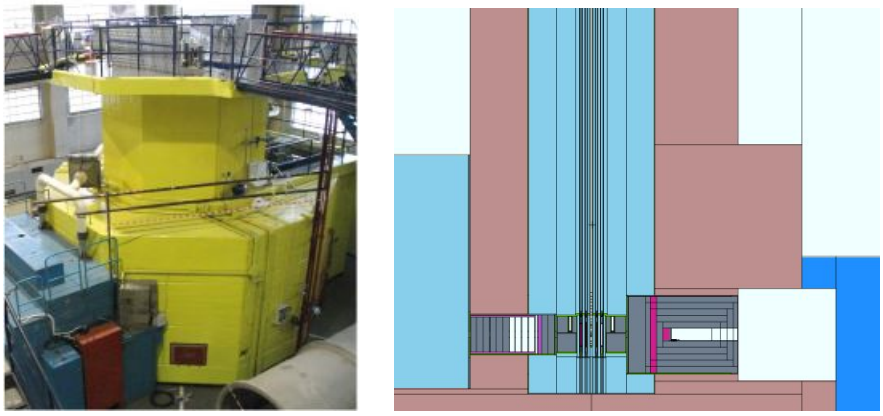

Figure 3.1: On the left Triga Mark II reactor in Pavia. On the right section (XZ plane) of the MCNP reactor model where thermal column is visible at the bottom right.

lected to obtain a dosimetry as precise as possible. In particular, the problem was separated into two main components: the dose of charged particles, produced in the neutron capture reactions in boron and nitrogen and through neutron scattering in hydrogen nuclei, and the dose of photons, produced in neutron capture in the materials (such as ${}^1H(n,\gamma)^2H$) and in the fission reactions occurring in the reactor core. The validity of the assumption of charged particle equilibrium (CPE) was explored in the specific case of the tissue geometry. Regarding the dose due to photons, the electron dose deposition was studied by varying the parameters governing the electron transport, also testing the difference between condensed history transport and single event transport.

3.1 Geometry

The TRIGA Mark II reactor model was previously developed and validated [28] (Figure 3.1). The neutron source is calculated in the reactor core using the KCODE feature, especially designed in MCNP to reproduce fission. This source had been previously validated [29] and updated more recently to take into account the fuel burnup. The experimental set-up with RHE models and culture medium was simulated in the irradiation position.

RHE tissues are irradiated at the end of the thermal column in a multi-well plate. This is a polyethylene plate (12.7 cm x 8.5 cm area and 2.1 cm

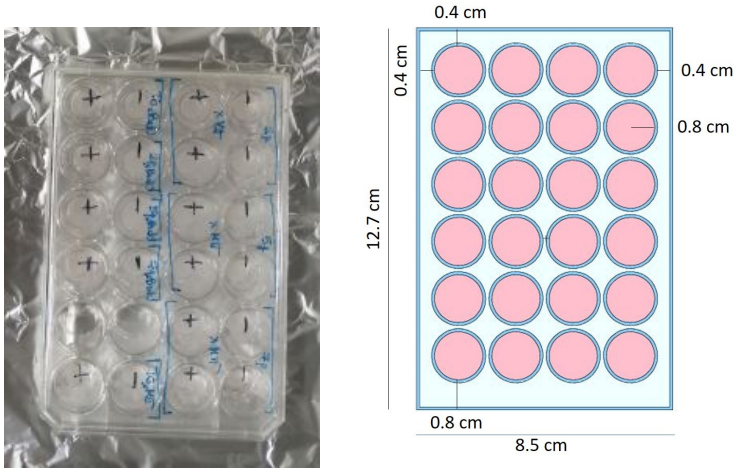

Figure 3.2: On the left real multi-well plate, with culture medium and RHEs inside. On the right the MCNP reconstructed one (XY plane).

width) with 24 wells 1 mm spaced one another, located in 4 rows of 6 units, each containing 300 μl of culture medium and one RHE tissue (Figure 3.2). This geometry was reproduced as faithfully as possible, approximating the multi-well plate to a parallelepiped with cylindrical wells, with radius of 0.8 cm and height of 1.9 cm along the Z-axis. Inside each well, three cylinders one above the other, represent from the bottom to the top: the culture medium (0.15 cm high), the RHE filter (made of polystyrene, with a radius of 0.399 cm and 17 μm high) and the RHE tissue (with a radius of 0.399 cm and 106.2 μm high) (Figure 3.3).

The height of the filter and tissue was measured in pictures of histological sections, as described in Chapter 4. The elemental composition of culture medium is unknown, due to the fact that EpiSkin^{TM} laboratory does not provide the details of the formulation. For this reason, the composition of the common medium used for cell cultures was simulated.

By default, MCNP treats particle interactions with the elements as if they were a free gas. If the energy of the incident neutrons is large compared to the binding energy of the atoms in a molecule, then atoms can be considered unbound, and nuclei interact independently with neutrons. In this case, supposing a molecular formula like X_wY_z, the scattering cross-section for the molecule can be expressed as [30]:

$$\sigma_{free} = w\sigma_X + z\sigma_Y \tag{3.1}$$

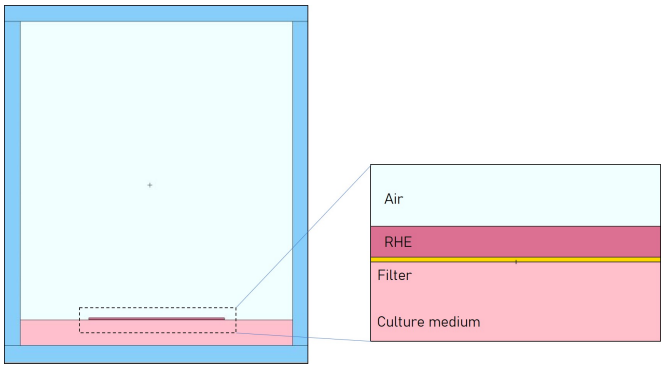

Figure 3.3: On the left single well geometry (YZ plane). The dashed rectangle indicates the zoomed geometry on the right. Culture medium (pink), RHE tissue (red) and filter (yellow) are visible.

where σ_X and σ_Y are the scattering cross-sections of the atomic species X and Y in the molecule. However, if the energy of the incident neutrons is of the order of or less than the binding energy, then molecular bonds cannot be neglected. In this case, the scattering cross-section of the molecule is related to σ_{free} by [30]:

$$\sigma_{bound} = \left(\frac{A+1}{A}\right)^2 \sigma_{free} \tag{3.2}$$

For heavy nuclei σ_{bound} is very similar to σ_{free}, whereas for light nuclei (such as hydrogen) σ_{bound} is much higher than σ_{free}. Therefore, the effect of molecular bonds in neutrons interactions is prominent for low neutron energies and for molecules containing light nuclei [31]. Moreover, when neutrons interact with a crystal structure through inelastic scattering, they can excite vibrational modes of the lattice (*phonons*) or gain energy from them. The energies of such vibrational modes are quantized. If a neutron energy is at least equal to a phonon energy, the incident neutron can excite the crystal, loosing one or more energy quanta. Conversely, for energies below a phonon energy value, neutrons are not able to excite the lattice, but they may instead gain one or more energy quanta, accelerating.

To take into account the chemical binding and crystal structure effects, MCNP provides the *thermal treatment*, through the card *MT* added to the specification of materials of interest: skin tissue, polyethylene and culture medium in this case. This card makes MCNP consider, at energies below 4 eV, the interactions with the molecular structure in the materials. The

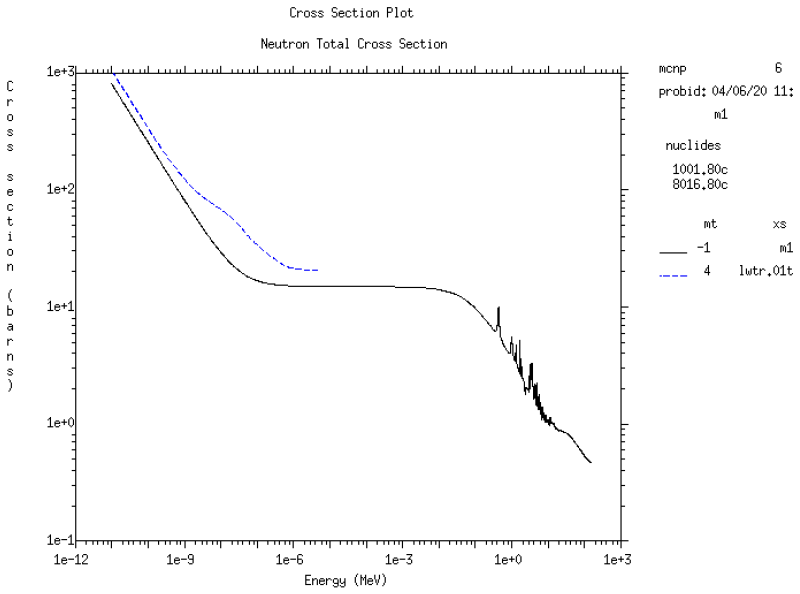

Figure 3.4: MCNP total cross-section for neutrons on water, using the MT on hydrogen for low neutron energies (blue dashed line) and without the MT card (solid line).

following distributions:

- lwtr.01t in the skin tissue and in the culture medium;

- poly.01t in the polyethylene.

take into account the hydrogen when is in water molecule and in polyethylene lattice. For tissue, the same distribution as the one of water was assumed [27]. Figure 3.4 shows the differences between the total cross-sections for neutrons in water, with or without the thermal treatment.

The materials used in the geometry of interest are listed in Table 3.1. Figure 3.5 shows the model of the multi-well plate, positioned at the end of the thermal column of the reactor.

Material	Density (g/cm^3)	Element/Formula	Mass (%)
Air	0.001124	$^{14}_{7}$N	78.11
		$^{16}_{8}$O	20.96
		Ar natural	0.93
Culture medium	1	$^{23}_{11}$Na	0.305
		Cl natural	0.377
		C natural	0.069
		$^{1}_{1}$H	11.016
		$^{8}_{16}$O	88.233
Skin	1.09	$^{1}_{1}$H	10
		C natural	20.4
		$^{14}_{7}$N	4.2
		$^{16}_{8}$O	64.5
		$^{23}_{11}$Na	0.2
		S natural	0.2
		$^{31}_{15}$P	0.1
		$^{32}_{16}$S	0.22
		Cl natural	0.3
		K natural	0.1
Polyethylene	1.06	$(C_2H_4)_n$	
Polystyrene	0.92	$(H_8C_8)_n$	

Table 3.1: Materials in the geometry of interest. Skin composition from ICRU Report 46 [11].

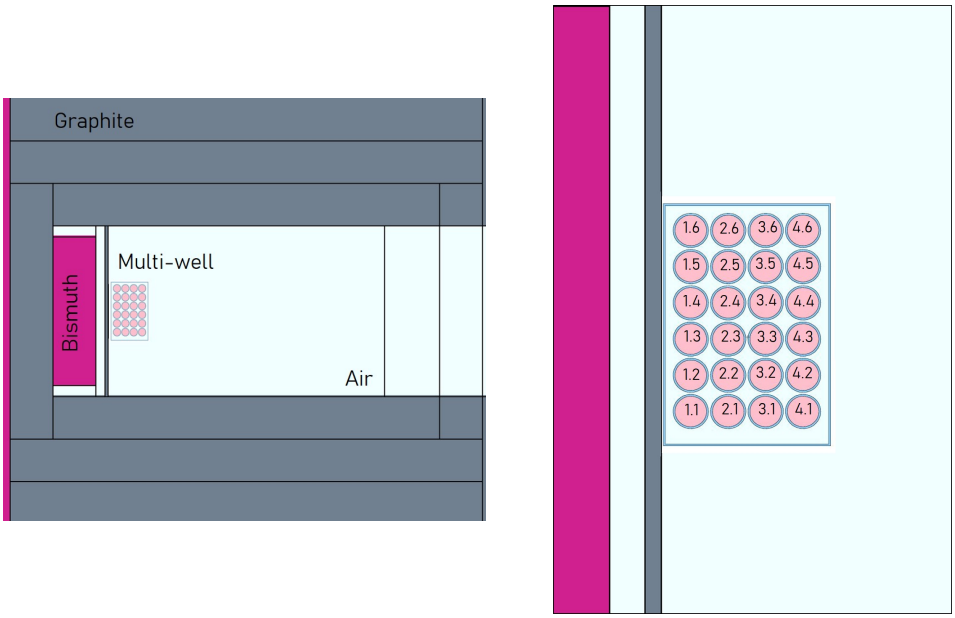

Figure 3.5: Left: multi-well plate in the thermal column model (XY plane). Right: zoom of the multi-well plate with numbered wells.

3.2 Variance reduction

MCNP transports particles between physical events until they disappear for physical interaction or because they exit the geometry of interest, sampling the probability distributions governing the events. When the particle history is complete, the quantities of interest, set by user as a *tally* in the input file, are scored together with the statistical uncertainty. When all the source particles have been run, the final result is calculated averaging the scores obtained in the specific volume or surface requested. The behaviour of the particles in the physical reality is estimated from the average behaviour of the particles in the simulation, using the central limit theorem. The tally is normalised per starting source particle and it is associated to its relative error, defined as the ratio between the standard deviation of the mean and the estimated mean of the required quantity. The relative error is proportional to $1/\sqrt{N}$ where N is the number of source particles run in the problem. The higher is N, the better is the statistical precision of the simulation. Increasing N, however, requires longer computational times. MCNP provides some computational strategies named *variance reduction techniques* to increase the precision of the tally (i.e. to decrease its relative error) without excessively

increasing the computational time and, of course, without affecting the results. When variance reduction is implemented, the calculation is *non analog*, i.e. each particle does not represent anymore a physical entity but instead it becomes a statistical track. MCNP assigns to each track a weight, which is 1 when no variance reduction is applied, and that changes with variance reduction. The weight is the instrument used to avoid biasing of the results when non analog transport is performed. The strategy chosen for this work is based on the association of a parameter called *importance* to the cells considered more relevant for the results, for example those between the source and the tally. Cells are the geometrical units in MCNP, they are uniform in material and density and they are defined by the bounding surfaces. When particles cross the surface between two cells with different importance, they undergo *Geometry Splitting* or *Russian Roulette*. If a particle with initial weight w crosses a surface between two regions with importance ratio equal to M>1, it is split in M virtual particles, each weighting w/M, having the same energy and flight direction, and each following different random walks. Conversely, if the second region is less important than the first (M<1), the particle plays the Russian Roulette, in which:

- the particle survives with probability M and assumes a weight w/M

  or

- the particle is killed with a probability (1-M).

Thus, when variance reduction is turned on, particles that undergo splitting decrease their weight, particles that survive Russian Roulette increase their weight to balance the weight lost due to Russian Roulette killing. In this way, total weight is statistically conserved and the final results are normalised by weight to avoid bias.

The increased number of histories obtained by splitting allows reducing the standard deviation of the tally because the number of contributing particles is higher, whereas the Russian Roulette allows sparing computing time, avoiding the transport of many particles in low interesting regions, condensing them in few, high-weight tracks. Geometry Splitting and Russian Roulette are based only on the ratio between the importance of adjacent cells and splitting or killing occur independently of the particle weight. Another variance reduction strategy, called *Weight Windows* (WW), is particle weight dependent. The weight of the particles is maintained in a fixed range

of values defining the (*window*), specified for each cell of the geometry. If a particle entering, or created, in a cell has a weight below the specified lower limit, then the Russian Roulette is applied. If the particle survives it acquires a weight that falls into the window. If its weight is above the upper limit, splitting is applied, and the created particles have weight inside the window. In all other cases, the particle weight remains unchanged. This strategy helps in keeping the weight of particles under control, avoiding over-splitting or the creation of extremely heavy particles, which may affect the statistical convergence of the problem. It has been shown that the best efficiency is achieved when the weight of particles throughout the geometry is maintained constant, i.e. when variance reduction balances the loss of particles due to physical interactions.

In our problem, the *Weight Windows Generator* was used to automatically create lower WW limits for the whole geometry (reactor model with the multi-well plate in the thermal column). The Weight Windows Generator card has the form:

WWG:x I_t I_c W_g j j j j I_E

where:

- x is the particle type for which create the WW;
- I_t is the number of the tally cell for which the WW must be optimised;
- I_c specifies if WW are cell-based or mesh-based (mesh-based would be independent from geometry and superposed). If cell-based, it has to be equal to a reference cell number; in our case it was a cell in the reactor core;
- W_g is the lower weight limit for the reference cell (or mesh). In our case was it set to 0.5;
- I_E specifies energy-dependent (0) or time-dependent (1) WW. In our case it was set to 0.

The WW generation can be iterative: after the run with the WWG on, a set of WW is calculated optimising the transport for I_t starting from the importance set defined in the input file. Afterwards, the WW limits can be incorporated in the input file with the WWG still on. This will produce a new set of WW limits, further optimised. The production of WW can be

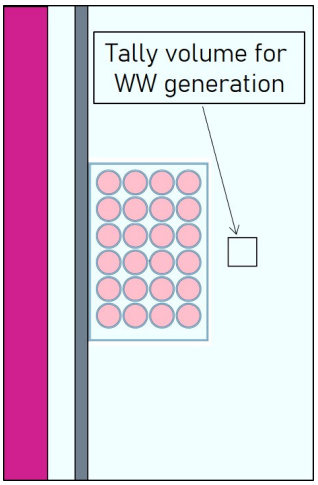

Figure 3.6: Multi-well plate in the thermal column, with the air cube tally used to obtain the Weight Windows limits (XY plane).

iterated until satisfying, then the WWG is turned off and the transport only calculates the tallies requested.

To set I_t, a cell representing an air cube was created on purpose, located behind the multi-well plate (Figure 3.6). In fact, the optimisation of the Weight Windows is not efficient using the real tally in the RHE cylinders. Being calculated in small volumes far away from the neutron source, the tally is in fact characterised by low statistics. The generation of a fictitious tally which is placed behind the geometry of interest, allows obtaining a good set of WW also in the multi-well plate, and consequently in the RHE cylinders.

Weight Windows lower limits have been obtained for neutrons and photons. The upper limits are managed with the following instruction:

```
WWP:x 5 3 5 0 0 0
```

where x is the type of particle. This card sets the upper values of the windows. In fact, the first entry says that if the particle weight goes above 5 times the corresponding lower weight bound in the WWN card, the particle will be split. The second sets the weight of the particles that survive the Russian Roulette: MIN(3 times the lower weight bound, WGT*5). The third entry sets the maximum splitting allowed: no particle will be split more than 5-for-one or be rouletted more harshly than one-in-5. The last 0 parameters tells MCNP where to perform the weight check (at the surface of the new cell entered by the particle), where to get lower bonds (from WWN) and if

WW are energy or time-based (energy-based, in this case, even if we have generated WW only for the total energy range).

Using the final set of generated WW, it was possible to obtain statistically significant results in shorter time compared to the time needed using only cell importance in the problem. The effectiveness of Weight Windows can be shown running the same input file with WW and with cell importance only. For this purpose, a neutron flux tally was calculated in the air cube below the multi-well plate in two input files containing the whole reactor geometry, one of these with the generated WW and the other only with the starting cell importance used to create the WW. In both files, a neutron source running 5e5 source particles was defined. The input file with WW completed 260 source particles per second, leading to a reliable tally that passed all of the 10 statistical tests that MCNP makes to verify the reliability of the results. In particular, the computed value for the neutron flux was: $9.18 \cdot 10^{-7}$ neutrons/cm^{2}s with a relative error of 0.74% with a Figure of Merit (FOM) of about 12. The FOM is defined as:

$$FOM = \frac{1}{R^2\, T} \tag{3.3}$$

where R is the relative error of the tally and T is the computer time in minutes. This quantity measures the efficiency for MCNP calculations: the more efficient the calculation is, the larger the FOM, because less computer time is required to reach an appropriate value of R (that must be less than 10% to be considered statistically reliable). The input file with cell importance completed 4345 source particles per second, computing a neutron flux of $4.59 \cdot 10^{-7}$ neutrons/cm^{2}s with a relative error of 70% and an associate FOM of about 0.03. However, despite the higher number of particles per second compared to the previous one, the tally did not pass 3 of the 10 statistical tests (variance, variance of variance and slope, see the Manual of the code), therefore the result is not reliable (in fact the tally is about half that calculated with WW). The lower value of the FOM clearly indicates that WW ensures a more efficient calculation: running the importance input for the same calculation time as the WW input, the relative error of the tally would be about 18%, still too high to accept the result.

Flux per source particle (x10^{-6} cm^{-2})

RHE Row	RHE Column					
	.1	.2	.3	.4	.5	.6
1	(1.777 ± 0.007)	(1.148 ± 0.006)	(1.163 ± 0.007)	(1.155 ± 0.005)	(1.162 ± 0.005)	(1.136 ± 0.005)
2	(1.087 ± 0.007)	(1.082 ± 0.006)	(1.084 ± 0.004)	(1.084 ± 0.004)	(1.088 ± 0.004)	(1.082 ± 0.004)
3	(1.031 ± 0.007)	(1.025 ± 0.005)	(1.028 ± 0.004)	(1.026 ± 0.004)	(1.023 ± 0.004)	(1.019 ± 0.004)
4	(0.972 ± 0.007)	(0.954 ± 0.006)	(0.948 ± 0.004)	(0.949 ± 0.004)	(0.949 ± 0.004)	(0.956 ± 0.003)

Table 3.2: Neutron flux per source particle in each RHE cell. The reported uncertainties are the statistical errors, computed ad described in Section 3.3.

3.3 Assessment of the uncertainty associated to dosimetry

To obtain a dosimetry as precise as possible it would be appropriate to consider differences in the dose delivered to the RHEs due to the different positions in the multi-well plate. In fact, moving away from the particle source, the particle flux in the samples decreases. Variations in the neutron flux along the longitudinal axis of the column where investigated. An input file with the reactor geometry and the multi-well plate positioned in the thermal column, was run. Weight Windows were properly set (as described in Section 3.2) and a neutron flux tally (F4:n, see Section 3.4) was calculated in each RHE cell. Results per source particle are shown in Table 3.2, numbering RHE cells as in Figure 3.5, where increasing numbers indicate RHE rows further away from the reactor core. From Table 3.2 it is possible to verify that, on average, there is a difference of about 17% between the neutron flux received by RHEs closest to the core and the farthest.

To obtain dose-effect curves as precisely as possible, RHE samples positions in the multi-well plate during the irradiation should be distinguished during the biological procedures that quantify the irradiation effects. However, in this first set of experiments, this classification was not possible for practical reasons. Thus, for the same irradiation conditions, dose delivered to the samples was averaged over all the positions in the multi-well. This flux variability introduced an uncertainty in the dose to be associated to a certain measure. To take it into account, we compute the standard deviation of the average. Therefore, in the next Sections each final result ($\overline{X}$) is associated to

the statistical error, σ_{stat}, and the standard deviation of the mean, $\pm\sigma_{mean}$:

$$\overline{X} \pm \sigma_{stat} \pm \sigma_{mean} \tag{3.4}$$

The statistical error (σ_{stat}) was computed by propagation of the MCNP statistical error:

$$\sigma_{stat} = \frac{1}{N}\sqrt{\sum_{i=1}^{N} \sigma_{x_i}^2} \tag{3.5}$$

where N is the number of tallies (N=24) and σ_{x_i} is the statistical absolute error associated to the i-th result (x_i), calculated multiplying the result by the correspondent MCNP relative error. This error represents the precision of the Monte Carlo calculations, that is the uncertainty in giving tally results due to statistical fluctuations in the scored quantities, and it is not physically meaningful, because in principle it can be lowered by increasing the number of particles in the run.

Conversely, the standard deviation of the mean is related to the differences in tally results obtained in RHE located in different wells of the multi-well plate. Therefore, it estimates the actual uncertainty due to the assumption that the same average dose is absorbed in all the samples. For this reason, the error bar in the dose axis is the dose-effect curves described in Chapter 5 is determined by the standard deviation of the mean. Which was calculated as:

$$\sigma_{mean} = \frac{\sigma}{\sqrt{N}} \tag{3.6}$$

where:

$$\sigma = \sqrt{\frac{\sum_{i=1}^{N}(x_i - \overline{X})^2}{(N-1)}}$$

is the sample standard deviation, chosen over the population standard deviation because of the small value of N in our case (N=24).

3.4 Dose from charged particles

The calculation of absorbed dose was initially divided in two steps: charged particle dose and photon dose. The former includes the energy deposition due to charged particles produced by neutron interactions with the elements in the skin, the latter includes both background photons and those produced in the skin by ${}^1H(n,\gamma){}^1H$ neutron interaction. For what concerns the charged component, different types of tallies can be set-up, depending on the assumption of Charged Particle Equilibrium (CPE). This assumption was investigated in our specific geometry. Thus, before entering in the simulation details, it is useful to describe the main quantities involved, the main types of tallies used and the conditions in which they are reliable.

The energy imparted in a volume V is defined as:

$$\epsilon = (E_{in})_n + (E_{in})_c - (E_{out})_n - (E_{out})_c + \sum Q \tag{3.7}$$

where $(E_{in})_n$ and $(E_{in})_c$ are the energies associated respectivley to the neutral particles and the charged particles entering the volume, $(E_{out})_n$ and $(E_{out})_c$ are the energies of the neutral particles and the charged particles leaving the volume and $\sum Q$ represents the net energy deriving from transformations of mass to energy and vice versa that occur in V.

The absorbed dose in a volume dV, having a mass dm, is defined as the expectation value of the energy *imparted* in the volume per unit mass [32]:

$$D = \frac{d\epsilon}{dm} \tag{3.8}$$

Therefore, it expresses the amount of energy absorbed by a medium per unit mass, as a result of radiation exposure, and it is measured in Gy (1 Gy = 1 J/Kg). The biological effects of the radiation are connected to dose, because this quantity measures the energy actually deposited in the volume of irradiated tissue. However, dose cannot be directly computed unless some conditions hold.

Another important quantity to be considered is the kerma. It is defined only for indirectly ionising radiations (neutrons and photons) as the expectation value of the energy *transferred* in a volume dV, having a mass dm, per unit mass [32]:

$$K = \frac{d\epsilon_{tr}}{dm} \tag{3.9}$$

The energy transferred in a volume V is, in turn, defined as:

$$\epsilon_{tr} = (E_{in})_n - (E_{out})_n^{nr} + \sum Q \tag{3.10}$$

where: $\sum Q$ is defined as in Equation 3.7, $(E_{in})_n$ is the energy of the neutral particles entering V and $(E_{out})_n^{nr}$ is the energy of the neutral particles leaving V, excluding the radiative losses by charged particles while they are in the volume.

Therefore, kerma represents the energy transferred to charged particles generated in the irradiated medium per unit mass, regardless of where or how they dissipate that energy, but excluding exchanges of energy between themselves. It is measured in Gy and it can be subdivided into two components depending on how the secondary charged particles loose the acquired energy:

$$K = K_c + K_r \tag{3.11}$$

The radiative kerma, K_r, refers to the component of the energy transferred to charged particles dissipated in radiative losses, while the collision kerma, K_c, refers to the component dissipated by excitation and ionisation in the volume. The latter can be expressed in terms of the net energy transferred, defined for a volume V as:

$$\begin{aligned} \epsilon_{tr}^n &= (E_{in})_n - (E_{out})_n^{nr} - (E_{out})_n^r + \sum Q = \epsilon_{tr} - (E_{out})_n^r \\ \epsilon_{tr}^n &= (E_{in})_n - (E_{out})_n + \sum Q \end{aligned} \tag{3.12}$$

where $(E_{in})_n$, $(E_{out})_n^{nr}$, $\sum Q$ are defined as in Equation 3.10, while $(E_{out})_n^r$ is the energy emitted as radiative losses by the charged particles originated in V. This quantity represents the energy transferred to the secondary charged particles that is not dissipated in radiative losses, but only by excitation and ionisation in the considered volume. Therefore the collision kerma can be written as:

$$K_c = \frac{d\epsilon_{tr}^n}{dm} \tag{3.13}$$

In condition of Charged Particle Equilibrium (CPE), the dose absorbed in a certain volume by an indirectly ionising radiation is equal to the collision kerma. In fact, CPE condition is valid in a volume V if each charged particle

leaving the volume is replaced by another particle of the same type and energy entering in V [32]. Thus, in CPE $(E_{in})_c = (E_{out})_c$, and the energy imparted (Equation 3.7) becomes:

$$\epsilon = (E_{in})_n - (E_{out})_n + \sum Q = \epsilon_{tr}^n$$

Comparing Equation 3.8 with Equation 3.13, the dose becomes:

$$D \overset{\text{CPE}}{=} K_c \tag{3.14}$$

The collision kerma is related to the energy fluence of the incident indirectly ionising radiation by [32]:

$$K_c = \int_{E_0}^{E_{max}} \Psi(E) \left(\frac{\mu_{en}}{\rho}\right)_{E,Z} dE \tag{3.15}$$

where:

- Ψ is the energy fluence (J/m^2);
- $\left(\frac{\mu_{en}}{\rho}\right)_{E,Z}$ is the mass absorption coefficient (m^2/Kg), that depends on the energy of the incident radiation and the atomic number of the irradiated material.

Thus, dose delivered by neutrons in a certain volume, where CPE is valid, can be expressed in terms of kerma factors $(F_n)_{E,Z}$ as follows [32]:

$$D = K_c = \int_{E_0}^{E_{max}} \Psi(E) \left(\frac{\mu_{en}}{\rho}\right)_{E,Z} dE = \int_{E_0}^{E_{max}} \Phi(E)\ (F_n)_{E,Z}\ dE \tag{3.16}$$

where:

- $\Phi(E)$ is the neutron flux (in cm^{-2});
- $(F_n)_{E,Z} = E \left(\frac{\mu_{en}}{\rho}\right)_{E,Z}$ are the kerma factors for neutrons and are tabulated as a function of the neutron energy E and the atomic number Z of the irradiated element.

The MCNP tallies to calculate doses are identified as F4, F6 and +F6. F4 tally is a track-length estimator of the flux (in particles/cm^2) in a specified cell:

$$F_4 = \int_V \int_t \int_E \Phi(\vec{r}, E, t)\ dE\ dt\ \frac{dV}{dt} \tag{3.17}$$

where $\Phi(\vec{r}, E, t)$ is the particle flux, which is the product of the particle density and the particle velocity. The code estimates this integral by summing WT_l/V for all particle tracks in the cell, where:

- W is the particle weight;
- T_l is the track length (in cm);
- V is the cell volume (in cm^3).

This tally can be modified through the FM multiplier card. It allows to obtain quantities of the form:

$$FM = C \int \Phi(E)\ R(E)\ dE \tag{3.18}$$

where C is an arbitrary multiplicative normalisation constant and R(E) is a response function, taken from MCNP libraries. If R(E) is a microscopic cross section, with a proper value of C, MCNP can calculate the total number of reactions of interest occurring in a cell. Considering a reaction type X that involves an element B, the reaction rate per gram in a volume V is:

$$R_X = \Sigma_X\ \Phi\ V = \sigma_X\ \Phi\ m_B\ \frac{N_A}{A} \tag{3.19}$$

where:

- Φ is the particle flux;
- σ_X is the microscopic cross section of the process of interest;
- m_B is the relative mass of the element B with respect to the total mass of the material where the reactions take place;
- A is the mass number of the element B;
- N_A is the Avogadro number, that is $6.022 \cdot 10^{23}$.

Thus, coupling an F4 tally (flux, in cm^{-2}) with an FM card in the form:

$$\begin{array}{c} \text{Fn4:particle} \\ \text{FMn4 (C M R)} \end{array} \tag{3.20}$$

it is possible to obtain the reaction rate per gram of a specific reaction, identified by R and that involves the element B of which is made the fictitious material M. In this case C will be:

$$C = m_B \, \frac{N_A}{A} \, \left(\frac{source\ particles}{s} \right) \cdot 10^{-24} \tag{3.21}$$

where 10^{-24} is the conversion factor from barns to cm^2 and the $\left(\frac{source\ particles}{s}\right)$ normalises the results for the true intensity of the source.

The tally F4, coupled with FM card, also allows obtaining the energy deposited in a volume, when all the reaction products are absorbed in that cell. In this case, the normalisation constant C in Equation 3.21 is multiplied by the Q-value of the reaction. To obtain the dose in Gy, it is necessary also the conversion factor $(1.6 \cdot 10^{-10})$ to transform MeV/g in J/Kg.

In this case, C constant becomes:

$$C = m_B \, \frac{N_A}{A} \, \left(\frac{source\ particles}{s} \right) \cdot 10^{-24} \cdot Q \cdot (1.6 \cdot 10^{-10}) \tag{3.22}$$

It is also possible to calculate a dose component in CPE coupling the F4 tally with tabulated kerma factors through the DE (energies) an DF (corresponding kerma factors) cards. MCNP calculates the fluence and multiplies the kerma factor according to the energy range of the particles.

F6 tally is a track-length estimator of the energy deposition averaged over a cell:

$$F_6 = \rho_a/\rho_g \int_V \int_t \int_E H(E) \Phi(\vec{r}, E, t) \; dE \; dt \; \frac{dV}{dt} \tag{3.23}$$

where H(E) is the heating response, ρ_a is the atom density and ρ_g is the gram density. The quantity scored by MCNP to estimate this integral is:

$$W \cdot T_l \cdot \sigma_T(E) \cdot H(E) \cdot \rho_a/m$$

where m is the cell mass and $\sigma_T(E)$ is the microscopic total cross section. The F6 result is in MeV/g and the heating response function depends on

the particle type for which the tally is calculated. +F6 tally (in MeV/g) is a collision heating tally which scores the energy deposition in the specified cell due to all particles transported in the problem. F6 includes the energy of secondary non-transported particles that are created in the tally cell, excluding photon energy. Therefore its estimate of the dose is valid only when CPE conditions are verified in the tally volume.

As shown above, neutron dose calculations using F6 tallies or F4 tallies, coupled with FM cards or with DE and DF cards, provide correct estimates of the dose only if CPE is valid in the volume of interest. In particular, the first method provides an estimate of the dose thanks to an internal heating function (H(E)) which corresponds to a total collision kerma. Conversely, the other two methods allow obtaining individual components of the total dose by providing the proper kerma factors and the Q-values of the considered reaction.

The first part of this study consisted in the calculation of the dose due to secondary charged particles generated in neutron interactions, testing different tallies and verifying if in the RHE cells the assumption of equilibrium is justified. Secondary particles arising from neutron interactions in the skin have a relatively short range in tissue: about 9 μm, 5 μm and 11 μm for respectively alpha particles, ^{7}Li-nuclei (from $^{10}B(n,\alpha)^{7}Li$ reaction) and 583 keV protons (from $^{14}N(n,p)^{14}C$ reaction). RHE tissues have a thickness of the order of 100 μm, thus some particles may escape from the volumes of interest depositing part of their energy outside. In fact, this issue arose in previous studies on mono layer cell culture simulations of BNCT irradiation [33]. In that case, being the cell layer only 10 μm thick, equilibrium could not be assumed at all (see below).

The whole reactor model and multi-well geometry (as described in Section 3.1) was used, transporting neutrons and photons (*mode n p*): in this way, the photons generated were transported as well as neutrons, but secondary charged particles were not and all their energy was assumed to be locally deposited (CPE assumption). Dose components in the RHE (numbered as shown in Figure 3.5) were computed with different tallies: F6, +F6, F4 coupled with FM (F4 + FM) and F4 coupled with DE and DF cards (F4 + DE/DF). The following contributions were calculated:

a) 583 keV protons and 42 keV recoil ^{14}C arising from the $^{14}N(n,p)^{14}C$ reaction;

Tally	Particle	Flux per KW $(cm^{-2}s^{-1})$
f4	n	$(7.956 \pm 0.008 \pm 0.1) \cdot 10^7$
	γ	$(2.78 \pm 0.02 \pm 0.03) \cdot 10^6$

Table 3.3: Neutron and photon fluxes normalised by C_4 and averaged over all RHE cells. Associated errors are calculated as shown in Section 3.3. Errors refer to statistical uncertainty and standard deviation of the mean, as described in expression 3.4.

b) alpha particles, lithium nuclei and 0.48 MeV photons arising from the $^{10}B(n,\alpha)^7Li$ reaction;

c) neutron scattering on hydrogen nuclei $^1H(n,n')^1H$;

Moreover, F4:n tally was calculated in the same cells in order to obtain neutron fluxes. Since tallies are provided per source particle, scores must be multiplied by the real intensity of the particle source, corresponding to neutron/s emitted from the reactor core in each experiment. In our case, the number of neutrons emitted per second by the reactor core was calculated as [32]:

$$\left(\frac{n}{s}\right) = \frac{P}{Q} \cdot \overline{N} \tag{3.24}$$

where:

- P is the reactor power in MeV/s;
- $\overline{N}$ is the average number of neutrons emitted per fission, that is 2.5;
- Q is the Q-value of the fission reaction in MeV, that is 207 MeV.

The particles emitted in the source for 1 kW power are:

$$C_4 = 7.5 \cdot 10^{13} \left(\frac{n}{s}\right) \tag{3.25}$$

The photon and neutron fluxes, normalised per kW and averaged over the 24 positions, are shown in Table 3.3. Dose due to the charged secondary particles

arising from neutron reactions in tissue, including the $^{10}B(n,\alpha)^{7}Li$ reaction by means of the addition of 20 ppm (20 $\mu g/g$) of ^{10}B in the skin material, was computed through a neutron F6 tally (F6:n) in the RHE cylinders. The same evaluation was made without ^{10}B in the skin, thus computing the dose due to all the charged secondary particles in a neutron-only irradiation. Since F6 results are in MeV/g it is necessary to convert them in Gy through the proper conversion factor, thus the correct normalisation constant:

$$C_6 = \left(7.5 \cdot 10^{13}\ \frac{n}{s}\right) \cdot (1.6 \cdot 10^{-10})\ \frac{g}{MeV}\frac{J}{Kg} = (12 \cdot 10^{3})\ \frac{g}{MeV}\frac{Gy}{s} \quad (3.26)$$

Result of F6:n tallies, once normalised at a reference reactor power of 1 kW and averaged over all the RHE positions, are:

- $(1.448 \pm 0.002 \pm 0.02) \cdot 10^{-4}$ Gy/s with ^{10}B in the skin material;
- $(2.553 \pm 0.004 \pm 0.05) \cdot 10^{-5}$ Gy/s without ^{10}B.

In order to calculate separately the dose components, both F4+FM tallies and F4 neutron tallies coupled with DE and DF cards were computed. For the latter, tabulated kerma factors (in Gy/cm^2) for each material involved in the main neutron interactions were used. Scores were normalised through the C_4 constant calculated above. F4+FM tallies were computed as described in Equation 3.20 with C constants calculated as shown in Equation 3.22 and proper R functions, listed in Table 3.4. An exception in the C calculation was made for the $^{1}H(n,n')^{1}H$ scattering, for which the Q-value of the reaction was omitted in the expression 3.22. In fact, it is not possible to define the energy deposited for neutron scattering on hydrogen nuclei because the energy transfer is a function of the incident neutron energy. Therefore, in this case, energy deposition (in MeV) was considered in the R composed parameter by means of the heating function (R= -4). Moreover, in the calculation of the C constant related to the dose component due to $^{10}B(n,\alpha)^{7}Li$ reaction, a ^{10}B concentration of 20 ppm was assumed and a weighted averaged Q-value over the two reaction branches was calculated as follows:

$$\overline{Q} = P_1 \cdot Q_1 + P_2 \cdot Q_2 = 0.94 \cdot 2.31\ MeV + 0.06 \cdot 2.79\ MeV = 2.34\ MeV$$

Values of the C constants, calculated for each neutron reaction of interest, are shown in Table 3.4.

Reaction	C	R
^{10}B(n,α)^{7}Li	0.034 $\left(\frac{Gy}{s} \cdot \frac{cm^2}{barn}\right)$	107
^{14}N(n,p)^{14}C	13.408 $\left(\frac{Gy}{s} \cdot \frac{cm^2}{barn}\right)$	103
^{1}H(n,n')^{1}H	$7.324 \cdot 10^3$ $\left(\frac{Gy}{MeV\ s} \cdot \frac{cm^2}{barn}\right)$	2 -4

Table 3.4: Parameters for the F4+FM tallies of interest. The R function used for ^{1}H(n,n')^{1}H dose component is a composed one: it includes the heating function (R=-4) and the elastic scattering function (R=2).

F4+FM tallies thus calculated provide the neutron kerma, which, in CPE, is equal to the delivered dose. For this reason, F4+FM tallies and F4 tallies coupled with kerma factors have to provide the same score. Normalised and averaged results, over all RHE cells, are shown in Table 3.5.

Table 3.5 shows, as expected, that there are no differences between results calculated with F4+FM tallies and the ones obtained through F4 tallies coupled with DE and DF cards, for each dose component. In particular, the difference in results related to the $^{10}B(n,\alpha)^{7}Li$ reaction dose component is of about 1%. A percentage difference of 1.5% can be obtain comparing the results related to the $^{1}H(n,n')^{1}H$ reaction, whereas for what concern the $^{14}N(n,p)^{14}C$ reaction, results differ by 0.6%. Moreover, the total neutron dose component in presence of ^{10}B, calculated with F6:n tally, is comparable to the sum of the neutron scattering on hydrogen dose component, the protons one from the $^{14}N(n,p)^{14}C$ reaction and the $^{10}B(n,\alpha)^{7}Li$ one. Therefore all these tallies can be used to perform calculations of the dose from charged particles, when CPE is valid. Tally F6:n does not allow computing a specific component of the dose, as do F4+FM and F4+DE/DF tallies, but it only provides the total dose from charged particles generated by neutron interactions in tissue (excluding dose related to electrons generated by secondary photons). Therefore, F4+FM and F4+DE/DF tallies are in general preferred, especially because they allow weighting the boron component for the true boron concentration measured in a given experiment. Finally, it is worth noting that the dose absorbed by the skin samples due to the $^{10}B(n,\alpha)^{7}Li$

Dose component	Dose rate per kW (Gy/s)		
	F4 + FM	**F4 + DE/DF**	**F6 with ^{10}B in tissue**
$^{10}B(n,\alpha)^{7}Li$	$(1.175 \pm 0.001 \pm 0.02) \cdot 10^{-4}$	$(1.186 \pm 0.001 \pm 0.02) \cdot 10^{-4}$	-
$^{1}H(n,n')^{1}H$	$(3.064 \pm 0.006 \pm 0.1) \cdot 10^{-6}$	$(3.110 \pm 0.006 \pm 0.1) \cdot 10^{-6}$	-
$^{14}N(n,p)^{14}C$	$(2.206 \pm 0.002 \pm 0.03) \cdot 10^{-5}$	$(2.220 \pm 0.002 \pm 0.03) \cdot 10^{-5}$	-
total n	$(1.426 \pm 0.001 \pm 0.02) \cdot 10^{-4}$	$(1.439 \pm 0.001 \pm 0.02) \cdot 10^{-4}$	$(1.448 \pm 0.002 \pm 0.02) \cdot 10^{-4}$

Table 3.5: Comparison between dose components, averaged over all RHE cells, calculated with F4+FM tallies and F4 tallies coupled with DE and DF cards (that is through the tabulated kerma factors multiplied by the neutron flux). Total neutron dose component in presence of ^{10}B in the skin material, calculated with a F6 tally, is reported in the last column. Errors are expressed as described in expression 3.4.

reaction, with a boron concentration of 20 ppm, is about 82% of the total dose. Thus, from a radiobiological point of view, a BNCT irradiation is more effective than a neutron-only one in causing tissue damage, because in the first case most of the dose is delivered by high-LET radiations (alpha particles and ^{7}Li-nuclei).

To test if the dose values calculated in CPE assumption are reliable, another calculation strategy was carried out. In fact, the only way to calculate energy deposition without assuming CPE, is to transport separately every secondary particle emitted. This is not possible with only one simulation, because the transport of secondary particles in the reactor geometry would be too expensive in terms of calculation time. The geometry was then restricted to only one well (in particular the 1.1 well, Figure 3.5), including culture medium, RHE tissue and filter. Secondary particles due to boron and nitrogen were isotropically generated in the skin tissue and transported using the *mode a p h #* card, where *a* represents alpha particles, *p* represents photons, *h* represents protons and # represents heavy ions (lithium nuclei in this case). Different input files were prepared in order to calculate the contribution to the total dose due to:

a) 583 keV protons and 42 keV recoil ^{14}C arising from the $^{14}N(n,p)^{14}C$ reaction;

b) alpha particles arising from the $^{10}B(n,\alpha)^{7}Li$ reaction;

c) lithium nuclei arising from the $^{10}B(n,\alpha)^{7}Li$ reaction;

For each dose component, a different homogeneous and isotropic source in the RHE volume was created, with the proper energy distribution. For point a), a 583 keV monoenergetic, uniform and isotropic proton source was created in the RHE cylinder. Problem mode was turned to *mode h p* and F6:h and F6+ tallies were calculated in the RHE. Since recoil ^{14}C nuclei deposit almost all their energy locally, their contribution per source particle to this dose component was simply calculated dividing ^{14}C energy (42 keV) by RHE mass ($5.79 \cdot 10^{-3}$ g).

The alpha component, point b), was computed generating a uniform, isotropic alpha source with the proper energy distribution. The $^{10}B(n,\alpha)^{7}Li$ reaction occurs with two different branches and the energy of the emitted alpha particle is branch-dependent (as shown in Chapter 1). For this reason, it was simulated a source emitting alpha particles with two different energies: 1.78 MeV (in 6% of cases) and 1.47 MeV (in 94% of cases). Both F6:a and F6:p were required, as well as +F6 tally. The same strategy was used to calculate the dose component at point c), for lithium nuclei with two different energies: 1.01 MeV (in 6% of cases) and 0.84 MeV (in 94% of cases). Also in this case F6:#, F6:p and +F6 tally were required and in both cases problem mode was set to *mode a p h #*. Importantly, the default charged particle energy cutoff was modified, via the *cut:pl* card, where *pl* is the particle type. In fact, if the energy of a particle falls down to the cutoff, then the particle is killed by MCNP and all its energy is locally deposited. Thus, if the particle source has an energy lower than the default cutoff, then all particles are killed immediately after the generation from the source. For protons the default energy cutoff is at 1 MeV, for alpha particles is at 4 MeV and for heavy ions is at 5 MeV. In our simulations they were set at the lowest energies allowed by MCNP, in order to follow particles as much as possible. In particular, for alpha particles and lithium nuclei it was set to 1 keV, while for protons to 10 eV. Below the cutoff, MCNP allows the transport, switching to nuclear models for the calculations.

As said before, tallies are provided per source particle, so it is necessary to multiply each score by the real intensity of the related particle source. In this case, the intensity of a specific particle source corresponds to the total reaction rate (in the RHE volume) of the neutron reaction producing that particle type. Reaction rates were obtained with the entire reactor, by

Reaction	Reaction Rate (s^{-1})	Source particle	Tally	Dose rate per kW (Gy/s)
$^{10}B(n,\alpha)^{7}Li$	(101.7 ± 0.7)	α	F6:a	$(8.18 \pm 0.06) \cdot 10^{-5}$
		^{7}Li	F6:#	$(4.70 \pm 0.03) \cdot 10^{-5}$
$^{14}N(n,p)^{14}C$	(1414 ± 9)	protons	F6:h	$(2.22 \pm 0.02) \cdot 10^{-5}$
		^{14}C	-	$(1.45 \pm 0.01) \cdot 10^{-6}$

Table 3.6: Total reaction rates per unit of reactor power in the RHE volume and normalised doses for each dose component. Also the ^{14}C contribution result is normalized by the corrispondent reaction rate. Results referred to the $^{10}B(n,\alpha)^{7}Li$ reaction are calculated for 20 ppm of ^{10}B. Since results refer only to one RHE cell, associated errors are only the statistical ones. Error associated to the ^{14}C result was deduced assuming the respective relative error equal to the one related to the corrisponding reaction rate.

setting proper F4+FM tally. Table 3.6 shows total reaction rates results for each reaction of interest and normalised dose components.

After normalising each result for the correspondent total reaction rate, alpha and lithium contributions to the dose were summed in order to obtain the total $^{10}B(n,\alpha)^{7}Li$ reaction contribution to the charged particles dose. Dose components related to the $^{10}B(n,\alpha)^{7}Li$ reaction are expressed per 20 ppm of ^{10}B. Similarly, proton and carbon contributions were summed to obtain the total $^{14}N(n,p)^{14}C$ reaction component.

To understand if the CPE condition can be considered valid in this specific problem, results were compared to those computed with the F4+FM and F4+kerma factors in the same well (Table 3.7).

Results in Table 3.5 show that there are no substantial differences between dose components calculated with F4+FM tallies and the ones calculated using tabulated kerma factors: 1% for the $^{10}B(n,\alpha)^{7}Li$ reaction component and 4% for the $^{14}N(n,p)^{14}C$ one.

It can be noticed that the difference is slightly bigger for the proton component than for the alpha and lithium dose. This is because the range in tissue of 583 keV protons is larger than the alpha and lithium one, so more particles from the $^{14}N(n,p)^{14}C$ reaction may escape the RHE volume. This

Reaction	Dose rate per kW (Gy/s)	
	NOT CPE	CPE
$^{10}B(n,\alpha)^{7}Li$	$(1.288 \pm 0.006) \cdot 10^{-4}$	$(1.30 \pm 0.01) \cdot 10^{-4}$
^{14}N(n,p)^{14}C	$(2.36 \pm 0.02) \cdot 10^{-5}$	$(2.45 \pm 0.02) \cdot 10^{-5}$

Table 3.7: Comparison between dose components (in the 1.1 RHE cylinder) calculated without CPE assumption (second strategy) and with CPE assumption (first strategy). Since results refer only to one RHE cell, associated errors are only the statistical ones.

differences could be taken into account in future calculations performed in CPE assumption adding this small correction factor.

Since there are no substantial differences between these dose components computed in CPE and the correspondent ones calculated without the CPE assumption, in this specific geometry it is possible to assume that CPE condition is verified for what concern high-LET charged particles. Since transporting all the secondary charged particles in a problem may result expensive both in computer time and in complexity of the simulation, this result support the choice of computing total charged dose by F6 or single contributions by F4+DE-DF. This is not possible when mono-layer cell cultures experiments are simulated. In that case, assuming charged particles produced by boron entirely absorbed in cells leads to 14% overestimation of the dose, while assuming protons produced by nitrogen entirely absorbed in cells leads to 30% overestimation. It was thus very important to investigate the dose deposition in this new model to produce a reliable dosimetry.

3.5 Photon dose component

The main dose component due to photons in BNCT includes 2.2 MeV photons from $^{1}H(n,\gamma)^{2}H$ generated in the RHE and in the culture medium, background prompt photons from neutron interaction with the surrounding materials, gamma produced in the fission reactions and 478 keV photons arising from the $^{10}B(n,\alpha)^{7}Li$ reaction in 94% of cases. As said before, the F6 tally for neutrons always supposes a local deposition of the energy of

Particle	**Dose rate per KW** (Gy/s)		
	F6	**+F6**	**F4+DE/DF**
n	$(1.448 \pm 0.002 \pm 0.02) \cdot 10^{-4}$	-	$(1.439 \pm 0.001 \pm 0.02) \cdot 10^{-4}$
γ	$\mathbf{(0.164 \pm 0.002 \pm 0.003) \cdot 10^{-4}}$	-	$\mathbf{(0.165 \pm 0.002 \pm 0.03) \cdot 10^{-4}}$
n + γ	$\mathbf{(1.612 \pm 0.003 \pm 0.02) \cdot 10^{-4}}$	$\mathbf{(1.611 \pm 0.002 \pm 0.02) \cdot 10^{-4}}$	$\mathbf{(1.604 \pm 0.003 \pm 0.05) \cdot 10^{-4}}$

Table 3.8: Gamma and neutron dose components averaged over all RHE samples, obtained with F6, +F6 and F4+DE/DF tallies (results of this section are in bold). In the last row F6:n and F6:p were summed and compared with the +F6 result. Results are per unit of reactor power. Errors are expressed as described in Expression 3.4.

secondary non-transported particles produced in the cell of interest, except the photon energy. If photons are transported (by the card $mode : n, p$) their contribution to the total dose in a cell can be scored with a F6:p tally. This includes all the energy transferred to secondary electrons, assumed locally deposited. For this reason, F6 tally may overestimate the real dose delivered to the volume of interest, especially when the volume is small compared to range of secondary particles in the specified material: electrons may in fact leave the cell where they are generated depositing their energy elsewhere. It provides a realistic score only in condition of electron equilibrium in the considered volume.

Using the entire reactor geometry, a photon F6 tally (F6:p) and a photon F4+DE/DF tally were calculated in RHE cells to obtain the dose due to all photons in the problem, assuming electron equilibrium. Moreover a +F6 tally was required, working as control. In fact, for what said before, in *mode n p* F6:n tally includes all energy deposition due to secondary particles produced by neutron interactions but not the photon contribution, which is computed by the F6:p tally. Thus, the sum of F6:n and F6:p must be equal to the +F6 tally. Dose rates per unit of reactor power, normalised respectively by C_6 constant (Equation 3.26) and C_4 constant (Equation 3.25) and averaged over all RHE cells, are shown in Table 3.8.

The sum of F6:n and F6:p is consistent with the +F6 result, as expected. Moreover F4+DE/DF result differs from F6 of just about 1%, therefore also for photon dose calculations these two tallies are equivalent.

In our specific geometry it is shown in Section 3.4 that CPE can be as-

sumed valid in the RHE volumes for charged particles produced by neutron interactions. If electron equilibrium was also valid, it would be sufficient to require a +F6 tally in RHE cells to calculate the total dose in the skin (with the addition of proper boron concentrations in the tissue material). However, this assumption is not obvious for the secondary electrons produced by photon interactions in the materials around RHE samples. This is because electron range in tissue is considerably longer than that of the heavier charged particles, also considering that in the RHE samples the spectrum of photons can span a wide energy range. It is thus necessary to investigate this condition transporting also secondary electrons and using a different tally. The most suitable tally for this purpose is the *F8 tally. It is a *pulse height tally* that provides the energy deposition (in MeV) due to photons and electrons in the cell of interest. The quantity scored by this tally is the net $W \cdot E$ in the cell, where W represents the particle weight and E its kinetic energy. In particular, when a particle crosses a surface entering in the cell, or when it is created inside it, the quantity $W_i \cdot E_i$ is scored. Conversely, when the particle is leaving the cell (or dies in it, for example because it reaches the lower limit of the energy cutoff, the quantity $W_i \cdot E_j$ is subtracted to the score. This type of tally does not work properly with non analog transport. For example, it gives negative scores due to knock-on electrons or variance reduction techniques. In this case, the tally score is not reliable. Moreover multipliers, such as the FM card, are not allowed [34, 35]. Setting the problem mode including photons and electrons (*mode p e*), *F8:e, *F8:p and *F8:p,e give the photon contribution to the total dose in a specific volume accounting for precise dose deposition of the secondary electrons. It is worth noting that simulation of electrons is perhaps the most difficult task in case of complex systems, characterised by small tally volumes located far away from the primary particle source. To obtain a calculation as precisely as possible, different parameters and different transport modes were investigated on the basis of different studies present in literature [36, 37].

Electron transport is complex because of its own nature: while neutral particle interactions are characterised by isolated collisions, electrons lose energy almost continuously during their path in matter, through several collisions. Following electrons in each single collision during their path requires long calculation time. As other codes, MCNP uses condensed history transport for electrons. Collisions can be described by multiple-scattering theories, such as the Goudsmit-Saunderson theory for angular deflections and the

Landau/Blunck-Leisegang theory of energy-loss straggling, that are based on several approximations [34]. Condensed history transport is based on clustering the effects of many individual collisions in single energy steps properly chosen so that the multiple-scattering theories are valid [34]. In particular, steps must be long enough to encompass several interactions, but short enough to ensure a small energy loss compared to the kinetic energy of the electron. Energy steps are related, on average, to length steps by:

$$E_{n-1} - E_n = -\int_{S_{n-1}}^{S_n} \frac{dE}{dS}\, dS = R_n \tag{3.27}$$

where E_n, S_n are, respectively, the energy and the total path length of the electron at the end of the n-th step, $\left(-\frac{dE}{dS}\right)$ is the total stopping power (that depends on the electron energy and the crossed material) and R_n is the n-th step path length. Path lengths are predetermined, at the beginning of the run, so that it remains valid the condition:

$$\frac{E_{n-1}}{E_n} = k \tag{3.28}$$

where k is a fixed value, equal to $2^{-1/8}$, that cannot be modified by the user. The electron interaction data (such as stopping power, probability distributions for angular deflection and for the production of secondary particles etc.) are calculated at the beginning of a run and tabulated on a energy grid, whose energy values respect the relation (3.28) [34, 38]. Electron steps determined in this way are called *major steps*, have path length s_n and are divided into m smaller steps called *substeps*, each s_n/m long. Energy loss and straggling are sampled from the respective probability distributions at the beginning of each major steps, whereas angular deflection and production of secondary particles take place at the end of each substep. The energy loss is considered constant during the same major step and at the end of each substep electron energy is recalculated on the basis of the current energy loss rate [38]. However, the energy straggling has to be considered in energy loss calculations, thus it is possible that electron energy sequence does not correspond to any of the energy grid determined by Equation 3.28. For this reason, an energy indexing is necessary, in order to assign the correct transport parameters to the electron (see below for further details) [38]. A new major step is started, i.e. a new energy group is assigned to the electron, when all the m substeps are completed or when the transported electron

reaches a geometric boundary or its energy falls below the lower limit of the step energy range (for example due to a secondary photon production at the end of some substep). The number m of substeps for each major step depends only on the considered material and MCNP sets it by default on empirical basis. These default values can be modified by the user, to adapt the simulation of the electron trajectory to the specific geometry of the problem. In particular, in a very small region there could be not enough substeps for an accurate simulation of the electron trajectory because the electron direction is sampled at the end of each substep, therefore also energy depositions may not be precisely computed: a more accurate angular deflection sampling may cause the electron to leave the region of interest earlier or stay in it longer than expected. In this case, the user is suggested to increase the number of substeps for each energy step in the material of interest, to let electrons make at least 10 substeps in that region [34, 35]. This can be achieved through the ESTEP option in the material card, setting ESTEP = m' where m' is the desired number of substeps per energy step [34, 35]. To calculate the correct value of m' for a specific material, it is possible to consult the Table 85 in the MCNP output, where a quantity called *e-step range*, as a function of the electron energy, represents the size of the energy step in g/cm^2. Therefore, the length of a substep in cm can be obtained as:

$$\frac{e - step\ range}{\rho m'} \tag{3.29}$$

where ρ is the material density in g/cm^3. Thus, if at least a total number N of substeps are desired in the shorter linear dimension SS (in cm), the minimum value of m' required is equal to:

$$m' = \frac{e - step\ range}{\rho} \cdot \frac{N}{SS} = \frac{e - step\ range}{SS_N \cdot \rho} \tag{3.30}$$

where SS_N is the substep length (in cm) desired in the material of interest in order to have at least N electron substeps within. The same procedure holds also for heavier charged particles transported in this problem. However, in the same material, they have a higher stopping power comparing to electrons, that means a smaller path length of the substeps, and so the rule to have at least 10 substeps is respected even in the small regions of the geometry (see below).

Electron transport in MCNP has been improved gradually in the versions

released over the years. In the 6.1 version of the code there are four different algorithms for the electron transport, i.e. different energy-indexing modes: the bin-centred algorithm, the ITS algorithm, the Energy and Step-Specific Method (also known as energy-loss straggling logic) and the Single Event algorithm that is a completely different strategy [37]. Previous versions allowed only the first two (MCNP4 and MCNPX) or three (MCNP5) algorithms, all being condensed history methods of transport, and electrons could be transported only down to 1 keV. The new Single Event method, coupled with the ENDF/B VI.8 cross sections database, transports electrons step by step down to 10 eV. The bin-centred mode assigns the electron transport parameters (energy loss, multiple scattering angle etc.) calculated starting from cross-sections at the upper limit of the energy bin in the middle of which the current electron energy falls. The ITS algorithm assigns the transport parameters corresponding to the upper energy of the energy bin whose upper boundary is the closest to the electron energy [39, 38]. Several authors investigated the differences in dose distribution calculations with this two algorithms, using as a benchmark codes such as EGSnrc or PENELOPE. For example, both Reynaert et al. [39] and Schaart et al. [38] found an overestimation of the electron energy in assigning transport parameters using the bin-centred algorithm, leading systematically to a lower energy loss rate comparing to the ITS algorithm. This overestimation leads to an underestimation of the scattering power, thus to a smaller angular deflection. Moreover, in the ITS mode, on average, the length of the substeps is shorter (because of the higher energy loss rate) and this allows a more accurate electron transport with respect to the bin-centred algorithm [39]. Shaart et al. also showed that using the bin-centred algorithm there can be discrepancies with the experimental data of up to 15% of the maximum dose [38]. However, also ITS mode presents some transport inaccuracies to which the user must pay attention. In fact, step-size and angular artefacts can occur. The former emerges when the geometry is composed by very small cells, comparable with the size of a single substep, which is relevant in our problem. In this case, neither angular deflection nor energy loss are computed until the end of the substep, which also correspond to about the cell boundaries where a new energy step is started. Thus, the multiple-scattering theory is not respected and a non-physical step-size dependent energy deposition occurs, as described by Hughes [40]. This kind of artefact can be partially removed by increasing the number of substeps per energy step, as shown above (Equation 3.30). Angular artefacts are caused

by the limitations in the complex representation of angular deflections and they mostly occur at high electron energies and with high-Z materials [41].

With the release of MCNP5 the new energy-loss straggling logic algorithm was introduced, in addition to the previous two modes. Regardless of the indexing algorithm, in previous versions of MCNP the Landau straggling distribution was sampled assuming that the electron assigned to the n-th energy group has an energy E_n and all the parameters needed for the sampling were computed for each step at the beginning of the run. With the energy-loss straggling logic, instead, the Landau straggling distribution is sampled using the current electron energy and the actual step length. In fact, in both ITS and bin-centred indexing methods it often happens that the electron is reassigned to a new energy group, because of a geometric boundary crossing. In this case the energy-loss straggling is sampled again, even if the range related to that group (R_n) has not been completed. With the bin-centred algorithm this also happens when the electron loses a considerable amount of energy in a substep. Hughes demonstrated that this new approach allows reducing significantly the step-size artefacts comparing to the bin-centred and ITS treatments [40]. The problem of the angular artefacts, however, remains and requires further improvements.

The Condensed History transport method is, obviously, an approximation of the real electron transport designed for electron energies higher than 1 keV, and it does not work well at lower energies. For example, Koivunoro et al. [36], simulating electron dose distributions in a water phantom, demonstrated large discrepancies between MCNP5 and the gold standard codes EGSnrc and PENELOPE for electron energies below 1 MeV (especially between 50 and 100 keV). The Single Event method provides a more accurate low-energy transport, thanks to the ENDF/B VI.8 database, which contains specific data for lower energies (such as the Electron-Photon-Relaxation library eprdata12). This method is based on direct sampling of microscopic data distributions, without multiple-scattering theories, resulting in a more realistic *collision by collision* transport [41].

By default, MCNP6 uses the Energy and Step-Specific Method of transport with the energy-loss straggling logic for electron energies down to 1 keV. In order to employ the Single Event method it is necessary to reduce the energy cutoff by means of the *cut:e* card [34, 35]. With the new library it is possible to transport electrons down to 10 eV (and photons down to 1 eV), but it is not recommended to reach such a low value [42]. This is because

it is possible to get to a condition in which electrons can no longer deposit energy through interactions in the material they are crossing. In fact, at very low energies, depending on the material, electron scattering without energy loss is the most likely interaction, overhanging also bremsstrahlung processes. Thus, for energies close to 10 eV, the electron may continue scattering without losing energy never reaching the energy cutoff, thus never finishing its history. For this reason it is suggested to setting the cutoff no lower than 12 eV [42]. Reducing the energy cutoff requires also to specify the use of the new eprdata12 library. When the cutoff is reduced by the user, Condensed History method is applied down to 1 keV and below this energy, down to the cutoff, the Single Event method is applied. User can modify the energy at which the transport method switches into the Single Event mode by means of the 15-th entry of the *phys:e* card. It is recommended not to transport electrons with the Condensed History method down to energies lower than the default [42]. Antoni et al. [37] studied the effects of raising the boundary energy between the two transport methods on dose distributions in water. They used different monoenergetic electron beams (at 50 keV, 100 keV, 500 keV, 1 MeV and 3 MeV) and set the starting Single Event energies always equal to the beam energy, comparing results with those obtained using only the Condensed History approach and with those obtained with EGSnrc and PENELOPE. Results show a remarkable agreement between the reference codes and MCNP6 using the Single Event transport up to 100 keV. Moreover, both step-size and angular artefacts almost disappear with this setting, demonstrating a more accurate transport comparing to Condensed History at low beam energies. On the contrary, at higher energies (both 500 keV, 1 MeV and 3 MeV) the Single Event method fails, showing an important shift in the dose-peak compared to PENELOPE calculations. In these cases, the default Condensed History with substeps properly adapted to the problem, turns out to be the most accurate [37]. The cited paper concludes that the best setting for electron dose calculations in water (and thus in tissue) is the default Condensed History mode with appropriate ESTEP and with the 15-th entry of the *phys:e* equal to 100 keV.

On the basis of the cited work [37] we calculated the photon dose component in our specific geometry comparing results obtained by transporting electrons in Single Event mode up to 100 keV and by Condensed History default mode, with different number of substeps per energy step. The comparison between different ESTEP parameter values were based on the work

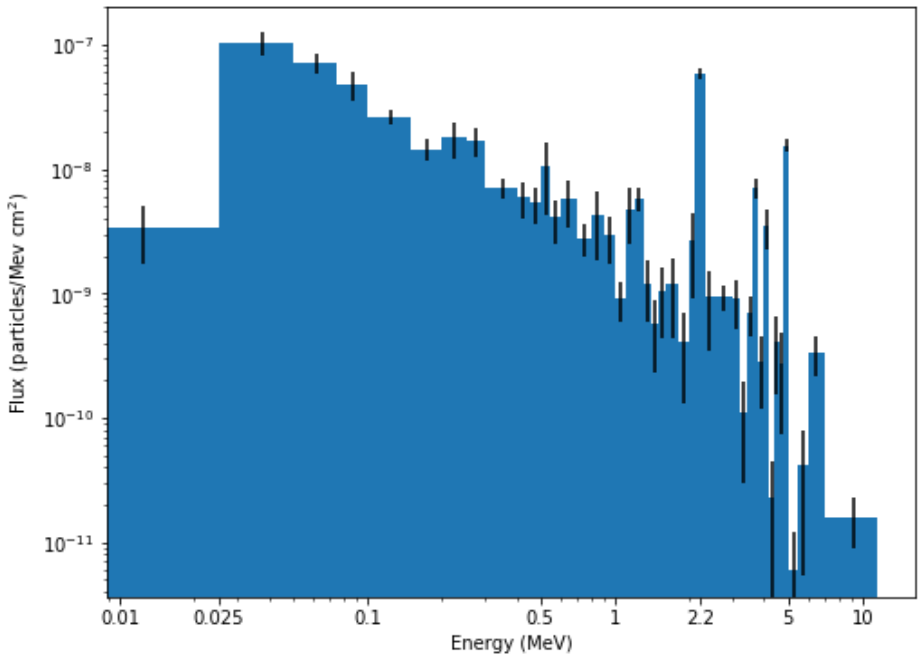

Figure 3.7: Average photon spectrum in RHEs.

of Koivunoro et al. [36]. They studied the influence of increasing this parameter in the gas cavity of a ionising chamber, the smallest tally region of their geometry, irradiated with different photon beams. They calculated ESTEP to have approximately 0.1, 10, 40 and 200 substeps at the mean electron energy in the gas cavity [36]. The absorbed dose in the gas cavity was in good agreement with PENELOPE with only 10 substeps. For higher values, the dose resulted underestimated. We adopted a similar sequence in the number of substeps: 10, 40, 80 and 200 substeps in the RHE volume. To calculate the correct number of substeps in RHE cell it is necessary to know the energy spectrum of the electrons generated. A two-step simulation was applied, in order to lighten the calculation. First of all, photon and electron spectra were calculated in the RHE cells, using the whole reactor geometry and the KCODE source. The problem mode was set to *mode n p* and photon spectra in the RHE cells were computed by means of F4 tallies coupled with E card, which subdivides the total flux in different energy bins. Photon flux is given in particles/cm^2 per source neutron. The photon spectrum, averaged over all RHE cells, is shown in Figure 3.7.

Then the geometry was reduced to only one well of the multi-well plate

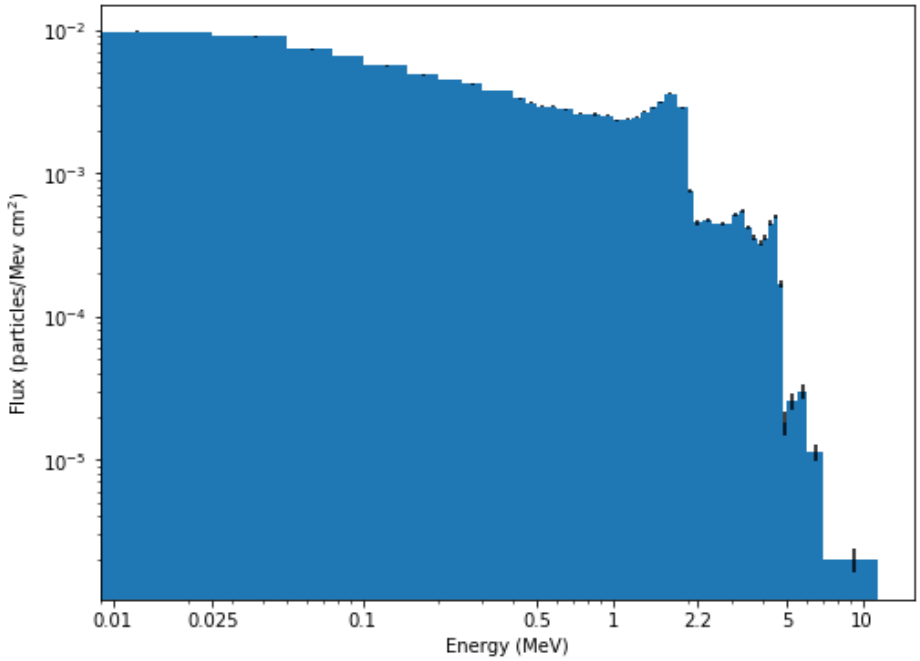

Figure 3.8: Electron spectrum in a single RHE.

and an isotropic photon source was implemented in it with an energy distribution derived from the photon spectrum in Figure 3.7. The problem mode was set to *mode p e* and the electron spectrum in the RHE cell was computed again with F4 tallies coupled with E cards. The obtained spectrum is shown in Figure 3.8 and represents only a rude estimate of the real spectrum. In fact, with this strategy electron produced in other regions of the geometry, that may reach the RHE volume varying the obtained spectrum, are not considered. However, in this case the purpose was only to get information on the electron average energies which can, in turn, influence the number of substeps to be set in the simulation.

Starting from the spectra in Figures 3.8 and 3.7, photon and electron weighted average energies were calculated as:

$$\overline{E}_i = \left(\frac{\sum_{k=1}^{m} \overline{\Delta E}_k \cdot \Phi_k}{\sum_{k=1}^{m} \Phi_k} \right)_i \tag{3.31}$$

where:

- i represents the particle type = photons (p) or electrons (e);

- k is the energy bin index = 1,2,. . . ,m ;

- $\overline{\Delta E_k}$ is the average energy of the k-th bin (in MeV);

- Φ_k is the flux component related to the k-th bin (in particles/cm^2).

It was obtained:

$$\overline{E}_p = (2.02 \pm 0.09)\ MeV$$
$$\overline{E}_e = (1.402 \pm 0.008)\ MeV$$

Photon weighted average energy is quite similar to the energy of photons produced by the $^1H(n,\gamma)^2H$ reaction. In fact, due to the high cross-section of the reaction at thermal neutron energies and the abundance of hydrogen in tissue, photons produced by this capture reaction constitute the main spectrum component, leading to a strong peak at 2.2 MeV (Figure 3.7).

Therefore the *e-step range*, correspondent to the energy value closest to $\overline{E_e}$, was selected from Table 85 in the MCNP output. According to Equation (3.30), different values of the ESTEP parameter in the skin were calculated, to obtain the sequence of the substeps number similar to the one used by Koivunoro et al. [36] in the smallest geometry region. Thus, in our case:

- SS = RHE tissue thickness[3] = 106 μm

- N = number of required substeps in SS = 10, 40, 80, 200

- ρ = 1.09 g/cm^3

obtaining the correspondent values for the ESTEP parameter:

$$m'_{10} \simeq 50$$
$$m'_{40} \simeq 200$$
$$m'_{80} \simeq 400$$
$$m'_{200} \simeq 980$$

[3]This is an average value obtained measurig the thickness of different sections referred to the same RHE sample (as describe in Section 5.3). This is a representative value that does not consider biological variability: different RHE tissues may have different thicknesses. However the variability range does not affect the results of the simulation because SkinEthic^{TM} ensures that samples have average uniform thickness.

Identical input files were created, differing from each other only for the ESTEP value, with a geometry composed only by the multi-well and a spherical, isotropic photon source of 2.02 MeV ($\overline{E}_p$) centred in the middle of the multi-well. The *F8:e tally was required in RHE volumes. Default Condensed History mode (energy-loss straggling logic) was used in these simulations and the computed energy depositions, averaged over all RHE cells, are shown in Table 3.9. In order to compare this method with the one suggested in [37], identical input files were created, differing from the previous ones only for the transport mode: the 15-th entry of the *phys:e* card was set to 100 keV, the second entry of the *cut:e* card was set to 20 eV (as suggested in [42]) and the *plib 12p* specifier was introduced in all the materials. In this way, it was possible to compare the effects in photon dose calculations of different ESTEP values both using default Condensed History transport and using the Single Event mode below 100 keV. Energy depositions, averaged over all RHE cells, are shown in Table 3.9. No significant differences were found, neither varying the ESTEP parameter with the same transport method, nor varying transport method with the same parameter. The highest percentage difference (in absolute value) between results obtained with the same transport method, but with different ESTEP values, was 3% for both Single Event and Condensed History results. A difference of 3% was also found between results obtained with $m' = 200$ but varying the transport method, while for $m' = 50$ the difference same was just of 1%. No differences at all were noticed between results obtained in the two transport modes with $m' = 980$ and $m' = 400$. Since transport in Single Event mode requires a significantly longer computer time, the default Condensed History method can be applied for this problem without making substantial errors, but setting an ESTEP value which allows at least 10 substeps in RHE tissues.

Evaluations on the correct ESTEP were made also for the charged particles transport described in Section 3.4, with the one-well only geometry. The related *e-step ranges* were taken from skin Table 85 in the outputs of dose calculations of lithium nuclei, alpha particles and protons transport. For protons the *e-step range* value was taken at a proton energy of about 600 keV. Whereas for alpha particles and lithium nuclei the *e-step ranges* were considered at weighted averaged energies over the two reaction branches:

ESTEP	Value per source particle (MeV)	
	CH	**SE**
50	$(2.46 \pm 0.04 \pm 0.04) \cdot 10^{-7}$	$(2.43 \pm 0.03 \pm 0.04) \cdot 10^{-7}$
200	$(2.48 \pm 0.04 \pm 0.05) \cdot 10^{-7}$	$(2.41 \pm 0.03 \pm 0.04) \cdot 10^{-7}$
400	$(2.46 \pm 0.04 \pm 0.04) \cdot 10^{-7}$	$(2.47 \pm 0.04 \pm 0.05) \cdot 10^{-7}$
980	$(2.40 \pm 0.03 \pm 0.04) \cdot 10^{-7}$	$(2.39 \pm 0.03 \pm 0.04) \cdot 10^{-7}$

Table 3.9: *F8:e results (Energy deposition in RHE tissues) averaged over all RHE volumes, obtained changing the transport method and the ESTEP parameter. CH refers to the default Condensed History method, whereas SE stands for the combined Single Event below 100 keV- Condensed History method above. Errors are expressed as described in expression 3.4.

$$\overline{E_\alpha} = (P_1 \cdot E_1 + P_2 \cdot E_2)_\alpha = (0.94 \cdot 1.47 + 0.06 \cdot 1.78) MeV = 1.49 MeV$$
$$\overline{E_{Li}} = (P_1 \cdot E_1 + P_2 \cdot E_2)_{Li} = (0.94 \cdot 0.84 + 0.06 \cdot 1.01) MeV = 0.85 MeV$$

At least 10 substeps in the RHE cell were imposed (N = 10) and minimum values for m′ were calculated according to Equation 3.30:

$$m'_{Li} \simeq 0.0020$$
$$m'_\alpha \simeq 0.0540$$
$$m'_p \simeq 0.1048$$

Results for m' show that for all charged particles considered there are already at least 10 substeps by default (ESTEP = 3) in the smallest region of the problem, as suggested by MCNP developers [34]. For this reason, the default values were used.

As said before, electron transport is quite complex and expensive in terms of computer time and resources. Ideally, the most accurate calculation of the photon delivered dose in RHE tissues would involve the whole reactor geometry and a *mode n p e* turned on. In this way, all secondary photons

and electrons would be followed in their energy deposition in the whole geometry and no equilibrium assumption would be made. However, in very complex and big geometries, with a complex variance reduction technique and with tallies in small volumes far from the neutron source, MCNP is not able to perform such calculation for electrons. In fact, *F8:e tallies were always unreliable in the attempts of transport considering the whole geometry and coupled n, p, e transport. Other two different strategies can be applied to overcome this problem: (a) a spherical source and (b) the SSW/SSR source. The first strategy consists in a two-steps calculation: first of all photon current and spectrum are calculated in a sphere surrounding the region of interest in *mode n p*. Then the tally is used to build an inward photon isotropic spherical source in a different input file with only the geometry of interest. This second run transports only photon and electrons and it allows the correct calculation of *F8 tallies. This approach was used in previous calculations [33]. This source may create some problems in validation because it does not take into account the particle directions, in fact, it simulates a source uniformly distributed in the spherical shell, while the reality could be very different. The second strategy, which is a two step strategy as well, allows considering the real particle direction distributions and its validation is straightforward. It is based on the possibility to project the real source in one or more surfaces located closer to the tally, using *SSW* (Surface Source Write) and *SSR* (Surface Source Read) features. The SSW card writes a surface source binary file where information such as type, energy, weight and flight direction of particles crossing the specified surfaces are recorded. A second run contains the SSR instruction which reads the binary file produced, and comprises only the interesting region. This speeds up the calculation because the transport is carried out only in a reduced geometry. The SSW/SSR feature allows breaking a complex simulations into two different consecutive runs without losing any information about particles reaching the tally. Thus, despite being more expensive in terms of coding time and power calculation, this second strategy ensure more precise results, without any approximation needed. Therefore, we chose this strategy for the simulations of the photon dose component in RHE tissues. In particular, surfaces delimiting the thermal column were selected for the SSW card in the reactor geometry, which was run in *mode n p*. It is in fact important to select the surfaces in a way that the reduced geometry contains sufficient materials to allow for secondary generated electrons to reach the tally (Figure 3.9). More-

Tally	Particle	Flux per kW ($cm^{-2}s^{-1}$)	
		KCODE	**SSW/SSR**
F4	n	$(7.956 \pm 0.008 \pm 0.1) \cdot 10^7$	$(7.77 \pm 0.01 \pm 0.1) \cdot 10^7$
	γ	$(2.78 \pm 0.02 \pm 0.03) \cdot 10^6$	$(2.60 \pm 0.02 \pm 0.07) \cdot 10^6$

Table 3.10: Neutron and photon fluxes, per unit of reactor power computed with the KCODE source (Section 3.4) and with the SSW/SSR source. All results are normalised and averaged over all RHE cells. Errors are expressed as described in expression 3.4.

over, since *F8 tally does not work well with variance reduction techniques, SSW source was first obtained by removing the WW. Then the geometry was restricted to only the thermal column region and the new particle source was read my means of the SSR card. In order to transport electrons mode card was turned to *mode n p e*.

The preliminary necessary step was the validation of this source. For this purpose, F4 tallies on neutrons (F4:n) and on photons (F4:p) were required and compared with the correspondent tallies obtained with the KCODE source. Results reported in Table 3.10 show discrepancy mostly in photon fluxes: about 2% between F4:n tallies and 7% between F4:p tallies, so this source was not satisfactory. This discrepancy is mainly due to the low amount of particles reaching the SSW surfaces, limiting the number of particles to simulate with the SSR card. To increase the number of particles reaching the SSW surfaces, a different strategy was adopted.

Thus, unitary cell importances were set only in the restricted geometry, while the SSW source was obtained with the file containing the WW variance reduction. All tallies previously computed with the whole reactor geometry were chosen as reference results for the validation and they were re-calculated with the SSW/SSR strategy. Results, normalised and averaged over all RHE cells, are shown in Table 3.11 and Table 3.12, where columns labelled as KCODE and SSW/SSR represent respectively results obtained with the KCODE and the ones obtain with the SSW/SSR strategy.

Tables 3.11 and 3.12 clearly show that there are no substantial differences between results obtained through the single-step simulation and the ones obtained with the two-step SSW/SSR strategy: the higher percentage

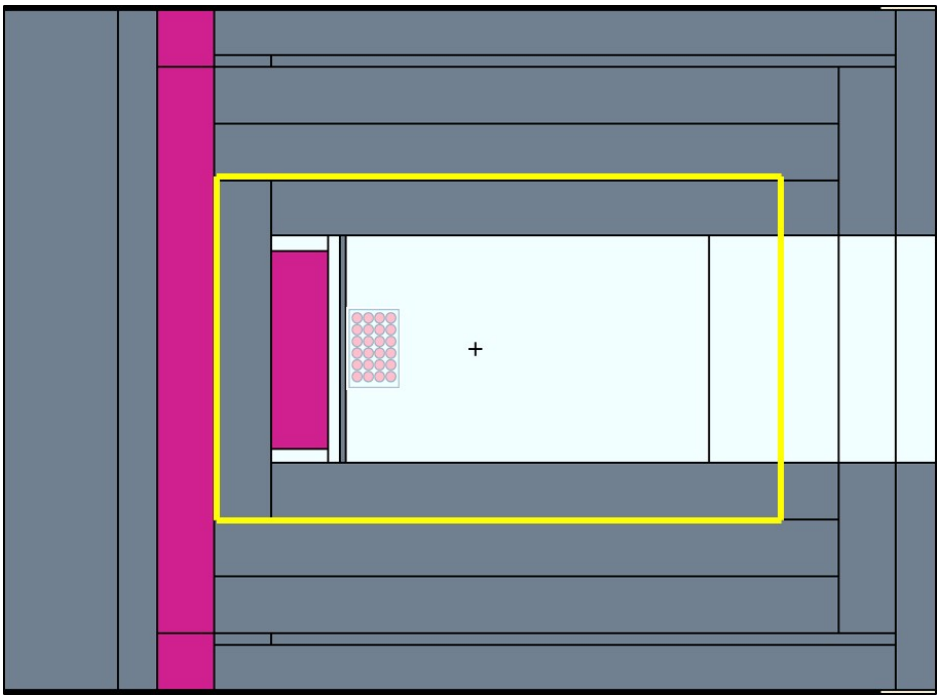

Figure 3.9: Surfaces (in yellow) delimiting the thermal column that were selected to write the surface source file during the first step of the SSW/SSR strategy (XY plane). Yellow surfaces also delimit the restricted geometry used during the second step of the strategy.

Tally	Particle	Flux per kW ($cm^{-2}s^{-1}$)	
		KCODE	**SSW/SSR**
F4	n	$(7.956 \pm 0.008 \pm 0.1) \cdot 10^{7}$	$(8.053 \pm 0.004 \pm 0.1) \cdot 10^{7}$
	γ	$(2.78 \pm 0.02 \pm 0.03) \cdot 10^{6}$	$(2.79 \pm 0.05 \pm 0.03) \cdot 10^{6}$
		Dose rate per kW (Gy/s)	
		KCODE	**SSW/SSR**
F6	n	$(1.448 \pm 0.002 \pm 0.02) \cdot 10^{-4}$	$(1.464 \pm 0.002 \pm 0.02) \cdot 10^{-4}$
	γ	$(1.64 \pm 0.02 \pm 0.03) \cdot 10^{-5}$	$(1.633 \pm 0.008 \pm 0.02) \cdot 10^{-5}$
+F6	n + γ	$(1.611 \pm 0.002 \pm 0.02) \cdot 10^{-4}$	$(1.592 \pm 0.003 \pm 0.02) \cdot 10^{-4}$

Table 3.11: Dose rate components and fluxes computed with the KCODE source (Section 3.4) and with the SSW/SSR source. All results are normalised and averaged over all RHE cells. Errors are expressed as described in expression 3.4.

Reaction	Tally	Dose rate per kW (Gy/s)	
		KCODE	**SSW/SSR**
$^{10}B(n,\alpha)^{7}Li$	F4+FM	$(1.175 \pm 0.001 \pm 0.02) \cdot 10^{-4}$	$(1.1895 \pm 0.0006 \pm 0.02) \cdot 10^{-4}$
	F4+DE/DF	$(1.186 \pm 0.001 \pm 0.02) \cdot 10^{-4}$	$(1.2002 \pm 0.0006 \pm 0.04) \cdot 10^{-4}$
$^{1}H(n,n')^{1}H$	F4+FM	$(3.064 \pm 0.006 \pm 0.01) \cdot 10^{-6}$	$(3.02 \pm 0.03 \pm 0.08) \cdot 10^{-6}$
	F4+DE/DF	$(3.110 \pm 0.006 \pm 0.01) \cdot 10^{-6}$	$(3.14 \pm 0.03 \pm 0.1) \cdot 10^{-6}$
$^{14}N(n,p)^{14}C$	F4+FM	$(2.206 \pm 0.002 \pm 0.03) \cdot 10^{-5}$	$(2.233 \pm 0.001 \pm 0.03) \cdot 10^{-5}$
	F4+DE/DF	$(2.220 \pm 0.002 \pm 0.03) \cdot 10^{-5}$	$(2.247 \pm 0.001 \pm 0.03) \cdot 10^{-5}$
		KCODE	**SSW/SSR**
total γ component	F4+DE/DF	$(1.65 \pm 0.02 \pm 0.03) \cdot 10^{-5}$	$(1.64 \pm 0.01 \pm 0.02) \cdot 10^{-5}$

Table 3.12: Dose rate components computed with the KCODE source (Section 3.4) and with the SSW/SSR source. All results are normalised and averaged over all RHE cells. Errors are expressed as described in expression 3.4.

difference, in absolute value, is of about 1.2%. Moreover, the total photon component calculated with F4+DE/DF tally differs from the F6:γ value of just 0.4%, therefore also using the SSW/SSR strategy both tallies correctly evaluate this dose component when electron equilibrium is valid. Thus, the SSW/SSR source was validated and it was used to compute *F8:e tallies in RHE cells. Results (in MeV) were multiplied offline, in order to obtain dose rates per unit of reactor power (in kW), by the constant:

$$C_8 = \frac{(1.6 \cdot 10^{-10}) \cdot (7.5 \cdot 10^{13})}{5.79 \cdot 10^{-3}} = 2.07 \cdot 10^6 \frac{Gy}{MeV \cdot s} \tag{3.32}$$

where:

- $(1.6 \cdot 10^{-10}) \frac{g}{MeV}$ is the conversion factor from MeV/g to Gy;
- $(7.5 \cdot 10^{13}) s^{-1}$ is the neutron source intensity at 1 kW (Equation 3.24);
- $(5.79 \cdot 10^{-3}) g$ is the RHE mass, calculated starting from the RHE cell volume reported in the MCNP output as $m_{RHE} = \rho_{RHE} \cdot V_{RHE}$.

This technique presents another advantage: photon dose rate includes all photons delivering dose in RHE tissues, regardless of their origin. In particular, having added to the RHE material also 20 ppm of ^{10}B, also 480 keV photons emitted by ^{7}Li excited nuclei in 94% of the reactions are transported and contribute to the tally. The background photon dose rate component is correctly included, which is normally the most difficult component to obtain for the reasons described above.

The mean gamma contribution to the total dose rate, per unit of reactor power, was computed by averaging *F8:e results (multiplied by C_8) over all RHE cells, obtaining:

$$d_\gamma = (1.27 \pm 0.02 \pm 0.03) \cdot 10^{-5}\ Gy/s$$

Errors are expressed as described in expression 3.4.

This value differs from the result obtained with the F6:γ tally (listed in Table 3.11) by about 22%. This discrepancy clearly shows that *the electron equilibrium assumption is not valid*, thus the right gamma dose component can be obtained only through an *F8 tally, transporting the secondary electrons.

On the basis of what described in this chapter, all dose rate components per unit power and per ppm of ^{10}B in the skin are reported in Table 3.13. In

Component	Dose rate per kW (Gy/s)
$^{10}B(n,\alpha)^{7}Li$	$(5.876 \pm 0.006 \pm 0.09) \cdot 10^{-6}$
^{14}N(n,p)^{14}C	$(2.206 \pm 0.002 \pm 0.03) \cdot 10^{-5}$
$^{1}H(n,n')^{1}H$	$(3.064 \pm 0.006 \pm 0.01) \cdot 10^{-6}$
total γ	$(1.27 \pm 0.02 \pm 0.03) \cdot 10^{-5}$

Table 3.13: Dose rate components per unit reactor power (in kW). The result for $^{10}B(n,\alpha)^{7}Li$ reaction component is expressed per ppm of ^{10}B in the skin. Errors are expressed as described in expression 3.4.

Chapter 5 dose-effect curves will be shown starting from these results: they will be normalised by the correct power, boron concentration, and irradiation time corresponding to each neutron irradiation.

Chapter 4

Calculation of absorbed dose - photon irradiation

Photon irradiation took place at Policlinico San Matteo of Pavia, exploiting their Best™ Theratronics equipment (Raycell® Mk2 X-ray blood irradiator) commonly used to sterilise blood bags for transfusions. This device is a lead shielded chamber containing two opposite X-ray sources of 160 kV (average photon energy of 60-80 keV), in the middle of which there is a removable lead drawer housing a holder for a two-liter canister, where samples are irradiated (Figure 4.1). The photon beams have a diameter of 20 cm in the middle of the canister, delivering to samples a nominal central dose rate of (8.9 ± 0.4) Gy/min. Commonly, blood bags are positioned inside the canister and, after a proper calibration, the delivered dose is determined by setting the irradiation time, based on the central dose rate.

The two-liter canister is a cylindrical plastic container of 9.7 cm in height and with a radius of 8.35 cm. During the calibration process a same-size tissue-equivalent phantom, made of polymethylmethacrylate (PMMA), is irradiated inside the canister with a ionisation chamber positioned at its centre, providing the dose rate absorbed in CE condition in the central position of the canister.

The canister can host also samples smaller than the blood bags. In this case, to maintain the CE, the samples are embedded in a PMMA phatom of reduced dimensions. In particular, another PMMA phantom 6.6 cm high is placed in the canister, and the multi-well with RHEs or flasks with cells cultures can be irradiated in the top of the phantom. The dose calibration is obtained with the same method, using the ionisation chamber in the centre

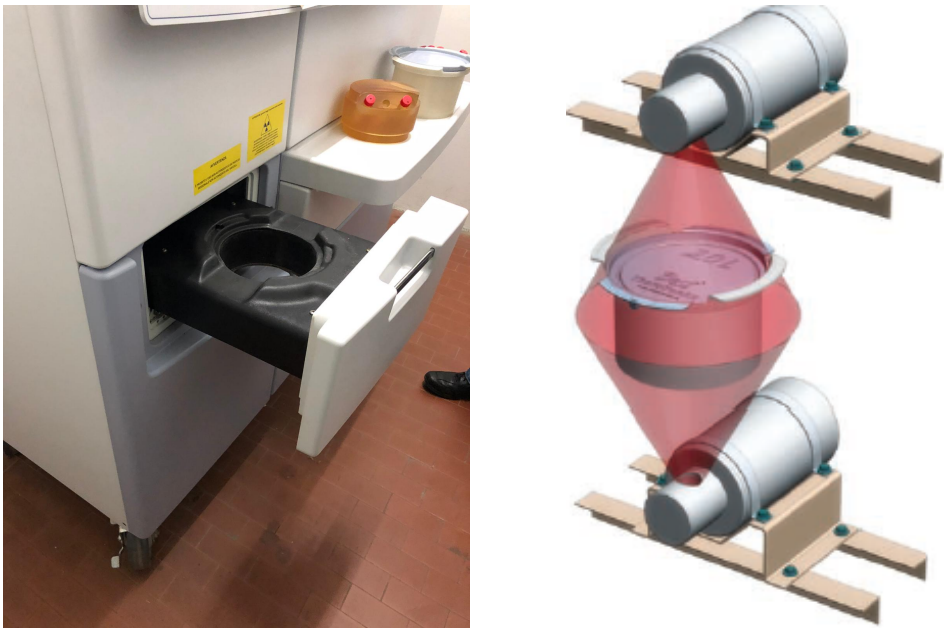

Figure 4.1: Photon irradiation set-up: removable lead drawer (on the left) and scheme of the canister irradiated by the X-ray sources (on the right, taken from Raycell® Mk2 informative brochure).

of the full-height phantom. For this reason, the nominal dose established by calibration may not be the real dose absorbed by the samples in the reduced geometry. First of all, in this configuration samples are not irradiated in the middle plane of the canister, where the dose rate is measured. Instead, they are positioned closer to the upper photon source. Secondly, while the blood bags are big enough to consider the CE condition valid in the irradiated volume, in samples with very small dimensions (ranging from a few to a hundred micrometers) it may be not respected, because the PMMA support is located only below the multi-well. Therefore, in these cases the CE assumption may consistently overestimate the dose in samples. Thus, the validity of the CE condition and the differences between the nominal central dose rate and the dose rate absorbed by RHE samples in the irradiation position were investigated with MCNP simulations.

Since the photon source intensity was unknown, it was not possible to directly calculate a dose rate in RHEs to be compared with the nominal one. However, the ratio between the nominal dose measured in the centre of the phantom and the dose absorbed by RHE samples in the irradiation position can be calculated, using MCNP tally results expressed per source particle.

Material	Density ($\frac{g}{cm^3}$)	Element/Formula
PMMA	1.19	$(C_5\ O_2\ H_8)_n$
Lead	11.34	100% Pb

Table 4.1: Materials present in photon irradiation simulations. The materials of the multi-well plate geometry were listed in Table 3.1.

If the irradiated samples actually absorbed the nominal dose rate during the photon irradiation, then the ratio between the dose per source particle in the ionising chamber and the one in the samples would be equal to 1.

Two different MCNP geometries were implemented: one representing the calibration measurement and one representing the RHEs irradiation set-up. The former was modelled as a PMMA cylinder 9.7 cm tall and with a radius of 8.35 cm, representing the phantom inside the canister, surrounded by a lead cylindrical ring (2 cm thick and 9.7 cm tall) representing the lead drawer in which the canister is placed during the irradiation. The ionisation chamber was realised as another PMMA cylinder (10 cm tall and with a radius of 1 cm) laid horizontally in the middle of the phantom (Figure 4.2).

The second configuration was modelled by removing a thickness of 3.3 cm from the top of the phantom cylinder and positioning the multi-well, as described in Section 3.1 in previous Chapter. In this second simulation, the cylinder representing the ionising chamber was removed (Figure 4.2). The materials comprised in the geometry are listed in Table 4.1.

In both cases two opposite point photon sources were implemented (Figure 4.3), 24.5 cm far from the upper and lower edge of the canister and with an angular opening (19°) so that they overlap in the centre of the phantom with a diameter of about 20 cm. The brochure of the Raycell® Mk2 irradiation system reports that the 160 kV X-Ray source has average photon energy between 60 and 80 keV. The energy distribution of the photon source was extrapolated from the spectrum reported in Figure 4.3, taken from G.Poludniowski et al. [43]. No variance reduction was necessary in these calculations; transport of secondary electrons was turned on.

Before computing the quantities of interest, some preliminary considerations were necessary. First, it was verified that the default ESTEP value for the skin allowed to have at least 10 substeps in RHE cells (the smallest

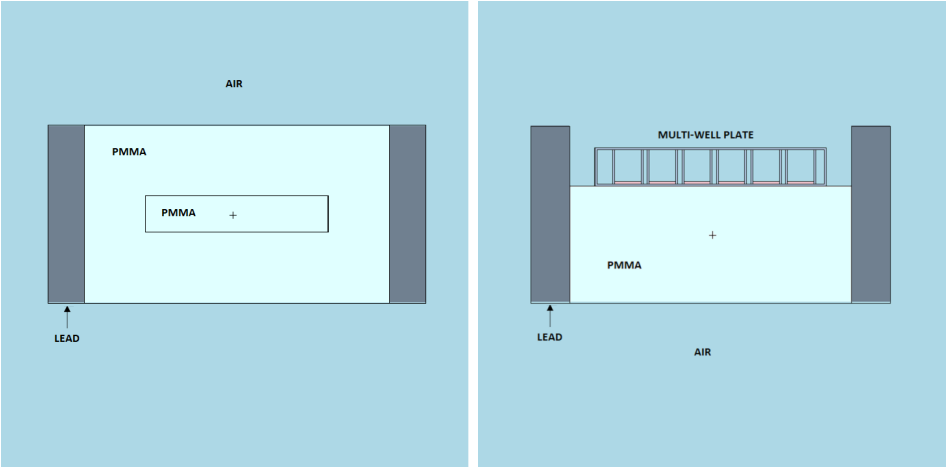

Figure 4.2: MCNP geometries. On the left, calibration geometry (XZ plane): lead cylindrical ring (grey) and PMMA phantom with the ionising chamber in the middle (light blue). On the right, RHE irradiation set-up (YZ plane): multi-well plate as described in Section 3.1, previous chapter, culture medium (pink), lead cylindrical ring (grey) and PMMA phantom (light blue).

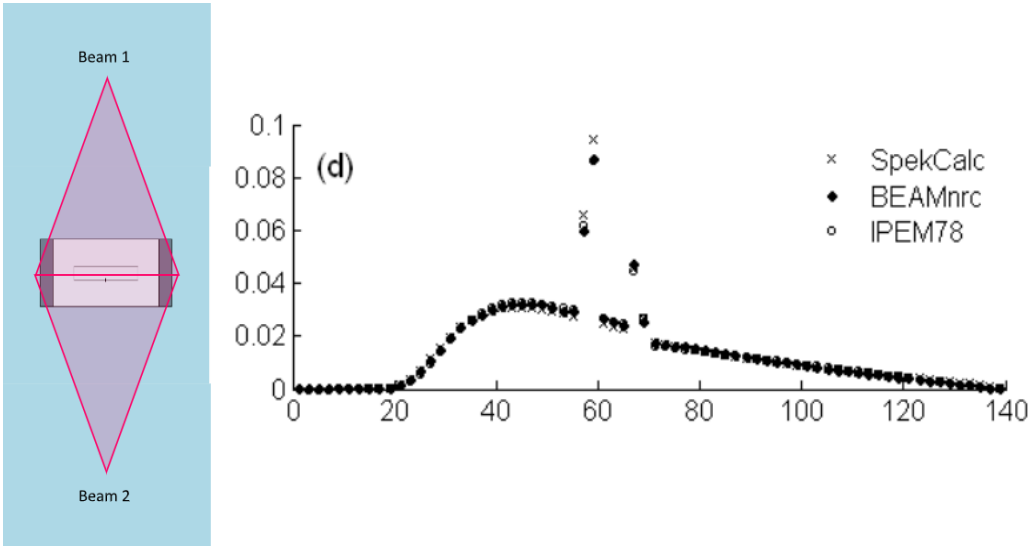

Figure 4.3: Left: scheme of the simulated photon source. Right: simulated source energy distribution, from [43].

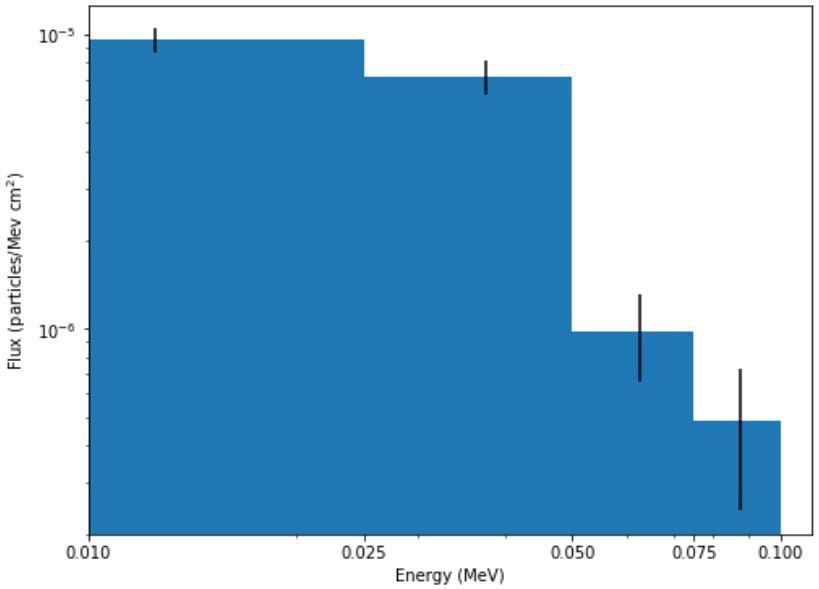

Figure 4.4: Electron spectrum in a central RHE.

regions of the geometry). Thus, the same procedure described in Section 3.5 of the previous Chapter was performed: electron flux was calculated in a central RHE cell and the mean weighted electron energy was computed, as in Equation 3.31, obtaining: $\overline{E} = (27 \pm 3)$ keV. Starting from this result, the *e-step range* was read in Table 85 (reported in the MCNP output file) and the minimum ESTEP value needed to have at least 10 substeps (m'_{10}) was calculated, according to Equation 3.30, obtaining: $m'_{10} \simeq 0.18$. Since the default value was 3, in this case it was adequate. Electron spectrum is reported in Figure 4.4.

The uniformity of the dose distribution in the phantom volume was studied using a rectangular Energy Deposition TMESH Tally. This is a particular feature of MCNP which calculates a certain quantity (in this case, the dose) in a grid superimposed to the problem geometry. The results can be graphically displayed over the geometry. In this case, a grid made up of cylindrical regions about 1 cm thick superimposed to the PMMA volume, where the photon dose deposited per particle source was calculated.

Results are shown in Figure 4.5 showing a difference in dose of about 20% between the central area and the bases of the phantom. This results anticipates the fact that the nominal dose cannot be taken as the actual dose absorbed by samples in the RHE irradiation position.

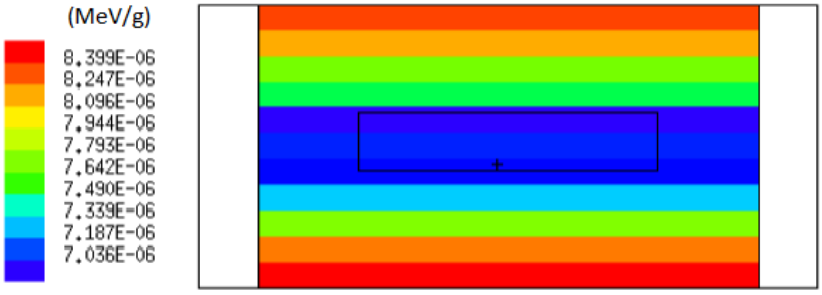

Figure 4.5: Vertical distribution of the photon dose in the PMMA phantom. The legend (on the left) expresses doses in MeV/g/source particle.

As described in Section 3.5 of the previous chapter, F6 photon tally calculates the dose delivered in a volume depositing the energy of secondary electrons in the point where they are created, even when electrons are transported. Conversely, *F8:e, *F8:p and *F8:p,e tallies provide the precise energy deposited by electrons in a certain volume. A photon F6 tally and an electron *F8 tally were required in the ionising chamber cell. F6 tally was multiplied by the conversion factor from MeV/g to Gy. *F8:e tally was multiplied by the constant:

$$C = \frac{(1.6 \cdot 10^{-10})}{37.39} = 4.29 \cdot 10^{-12} \frac{Gy}{MeV}$$

where $(1.6 \cdot 10^{-10}) \frac{g}{MeV}$ is the conversion factor from MeV/g to Gy and 37.9 g is the mass of the ionising chamber cell. Results of F6 and *F8 tallies are reported in Table 4.2.

The same tallies were calculated in the second set-up, in each RHE cell and averaged over the 24 samples, providing the mean dose absorbed in samples with CE assumption and the deposition of electron energy in skin without CE assumption. F6 results were multiplied by the conversion factor from MeV/g to Gy; *F8 results were multiplied by:

$$C = \frac{(1.6 \cdot 10^{-10})}{(5.79 \cdot 10^{-3})} = 2.77 \cdot 10^{-8} \frac{Gy}{MeV}$$

where $(5.79 \cdot 10^{-3})g$ is the RHE mass, calculated starting from the RHE cell volume reported in the MCNP output as $m_{RHE} = \rho_{RHE} \cdot V_{RHE}$.

Tally	Dose per source particle (Gy)	
	Ionising chamber	**RHEs**
F6:p	$(1.124 \pm 0.005) \cdot 10^{-15}$	$(1.40 \pm 0.02 \pm 0.02) \cdot 10^{-15}$
*F8:e	$(1.13 \pm 0.01) \cdot 10^{-15}$	$(1.35 \pm 0.02 \pm 0.02) \cdot 10^{-15}$

Table 4.2: Doses per particle source, calculated with the CE assumption (F6:p) and without (*F8:e), in the ionising chamber and in RHE samples. Since results referred to RHE samples are averages over all RHE cells, the associated errors are expressed as described in expression 3.4. Errors related to ionising chamber results are only statistical errors.

Table 4.2 shows no substantial difference between the dose computed by F6 and *F8 in the ionising chamber volume as expected because the assumption of electron equilibrium was reasonable in this set-up. On the other side,the difference between F6 and *F8 in RHE samples is about 4%, demonstrating that the equilibrium is not granted in this configuration. The electron transport is thus necessary to take into account the amount of energy deposited by secondary particles outside the volume of the samples. More significantly, a difference of about 24% is obtained comparing the F6:p results in RHE cells and in the ionisinig chamber. Hence, the skin samples absorb a dose higher than the nominal one due to the irradiation position, which is closer to the upper photon source. Combining the results, the ratio between the actual dose absorbed by RHE and the dose absorbed by ionising chamber is 1.20: the nominal dose set by calibration must be corrected by this factor.

Finally, the effects of the Single Event transport mode below 100 keV was investigated also in this simulation. The 15-th entry of the *phys:e* card was set to 100 keV, the second entry of the *cut:e* card was set to 20 eV, the *plib 12p* specifier was introduced in all the material specifications and the F6 and *F8 tallies were computed as described above. Averaged and normalised results are reported in Table 4.3. No substantial differences were found between the two transport methods. Thus, for the sake of computation time, the default electron transport mode can be used in this configuration.

Tally	Dose per source particle (Gy)	
	CH	**SE**
F6:p	$(1.40 \pm 0.02 \pm 0.02) \cdot 10^{-15}$	$(1.41 \pm 0.02 \pm 0.1) \cdot 10^{-15}$
*F8:e	$(1.35 \pm 0.02 \pm 0.02) \cdot 10^{-15}$	$(1.35 \pm 0.02 \pm 0.02) \cdot 10^{-15}$

Table 4.3: Doses per particle source in RHEs, calculated with (F6:p) and without (*F8:e) the CE assumption in RHE cells with Single Event transport mode below 100 keV (SE) and with the default Condensed History mode (CH). All results are normalised and averaged over all RHE cells. Errors are expressed as described in expression 3.4.

In conclusion, photon/electron transport in the photon irradiation set-up show that:

1) dose is not uniform along the canister axis: at the central region of the canister dose is 20% lower than at its bases;

2) electron equilibrium does not hold in RHE samples: the actual absorbed dose is 4% lower than that calculated with CE assumption;

3) the dose absorbed by RHE samples is 20% higher than the nominal dose set by the calibration procedure.

Chapter 5

Radiobiological evaluations

The SkinEthic^{TM} Reconstructed Human Epidermis (RHE) model was selected as the radiobiological model to study healthy skin response to the dose delivered in BNCT irradiation. Obviously, the best scenario would be an *in-vivo* model, that would allow a longer follow-up after irradiation and that would provide the most complete physiological model for the monitoring of the radiation effects. However, research with animals requires a long authorisation process and dedicated funds. To comply with the *3 R principle*[4], it is advisable to work with *in-vitro* models whenever is possible. In this respect, RHE model is more comparable to the *in-vivo* human tissue than a mono-layer and mono-type cell culture and the irradiation response can at least reflect the complexity of the structure and the different cell types composing the tissue.

In the study to assess the dose-effect relation, it is necessary to produce a precise dosimetry (previous chapters) and to establish the effects to be studied and the methods to measure them. This Chapter is dedicated to the preliminary studies dedicated to this second part of the work. In particular, it describes the techniques used to point out the effects of the irradiation in tissues, the issues related to the analysis and the new measurements that we found necessary to produce the curves. RHE tissues were irradiated with neutrons only, with neutrons in presence of boron and with photons, which are used as reference radiation.

The availability of robust radiobiological data is very important for estab-

[4]The 3 R Principle: Reduction, Replacement, Refinement Created in 1959, is the basis for the ethical approach applied to animal studies in Europe and North America. Its provisions serve as a basis for all research projects involving the use of animals.

lishing safe and accurate dose prescriptions for the planned treatment. The long-term goal is to calculate photon-equivalent doses, in order to compare BNCT effects with those of conventional radiotherapy, based on the observed endpoints in normal skin. These evaluations represent the first step to build Normal Tissue Complication Probability (NTCP) curves, to feed computational dosimetry models, as an alternative to the classical fixed-RBE model. For example, the *photon iso-effective dose model* proposed by González and Santa Cruz [12] is based on equalling a specified effect due to BNCT and due to photon irradiation, thus considering the whole dose-effect curves instead of a single fixed point. It was already extended to use NTCP for mucosa based on the experimental results using a hamster model in Argentina [44].

Morphological and structural changes induced in RHE by irradiation were investigated in histological preparations. Treated RHE were sectioned and stained; then, we measured the thickness of the sections and of each layer. As previously mentioned, irradiation effects in skin can be observed from a few hours to also about 50 weeks post-irradiation. With RHE model it is not possible to reach such a long observation time because the life of the tissues is guaranteed only for a week. However, within a week from the irradiation, it is possible to understand if there is a temporal evolution for acute damages. To this end, different observation times from irradiation were selected: immediately after the irradiation (T0), after two days (T2), after five days (T5) and after seven days (T7). The qualitative analysis of the histological sections allowed some considerations about boron concentration evaluation and stimulated work plans for the future.

Another test was the measurement of the cell viability by MTT assay. When monolayer cell cultures are irradiated, the survival is measured by the clonogenic assay, which measures the capacity of cells to survive the irradiation and to produce new colonies. With RHE, it was impossible to apply this method. Thus, as a first approach, we measured the cells that at the observation time were metabolically active. MTT provides an estimate of the immediate damage in the tissue, intended as the loss of the constituent elements of the tissue itself (i.e., its cells). However, cells still alive at the observation time may be unable to proliferate due to damages induced by the irradiation, going into apoptosis (programmed cell death) at the end of their cell cycle. These cells are classified as alive by MTT assay. For this reason, it is important to assess also the capacity of the tissue to proliferate; to this end have prepared RHE samples for BrdU assay, that is a specific test

for proliferation capacity.

5.1 Cell viability as a function of the dose

A dose-effect curve describes the relationship between the dose delivered to the target and a specified biological endpoint, commonly cell survival in *in-vitro* studies. Survival is plotted as a function of the dose and different cell survival models are available to describe the survival behaviour. One of these is the *linear quadratic model*, describing the cell killing in terms of single radiation tracks that produce lethal lesions, with a yield proportional to the dose, and of two independent radiation tracks that produce DNA lethal damages, with a yield proportional to the square of the dose:

$$S = e^{-\alpha D - \beta D^2} \tag{5.1}$$

where α and β are constants depending on the radiation type. Curves associated with high-LET radiations present a survival fraction behaviour that is linear (in semi-logarithmic scale), with a constant slope given by α parameter and β parameter equal to zero. Conversely, curves associated with low-LET radiations present a shoulder at lower dose, determined by the quadratic term. As described in Section 1.2, the BNCT radiation field is composed by radiation types with different LET, due to the mechanisms of neutron energy release in tissue. Depending on the composition of the beam, the dose absorbed due to neutron irradiation can lead to linear or linear-quadratic curves. Usually, in presence of boron and with a thermal beam, survival curves due to BNCT are fitted with a linear model. Instead, curves obtained with a gamma rays irradiation are expected to follow a linear-quadratic trend.

5.2 Irradiation protocols

Neutron irradiation experiments were performed positioning the samples in the Thermal Column of the TRIGA Mark II reactor of the University of Pavia, at different powers and for different irradiation times (Table 5.1). Photon irradiation took place at Policlinico San Matteo (Pavia), exploiting its Best™ Theratronics equipment (Raycell® Mk2 X-ray blood irradiator) commonly used to sterilise blood bags for transfusions. Both irradiation set-ups are described in Chapters 3.4 and 3.5 as they were simulated by MCNP6

for dose calculations.

RHE are shipped by Episkin Company upon request; they prepare the number of samples required, which are delivered one month after request. When the batch arrives, the RHE tissues are removed from the agarose-nutrient solution and placed in the multi-well plate with 1 ml of SkinEthic Maintenance Medium (shipped together with the tissues) for one night. After they are kept overnight in the incubator, experiments can be performed. Samples dedicated to BNCT irradiation undergo the boron administration protocol described in Section 2: they stay in contact with BPA-enriched medium at a concentration of 80 ppm for 4 hours, then they are washed with a saline solution (PBS) to remove residues of BPA. In order to reduce as much as possible differences in the protocol between samples, all other samples are also washed with PBS. After that, culture medium is replaced with fresh maintenance medium and samples are transported to the irradiation facility. Samples with boron and without boron are irradiated with neutrons in the same multi-well plate. Thus, they pass through the same external conditions and they receive, on average, the same neutron fluence. In this way, differences in dose-effect curves can be reasonably attributed only to the $^{10}B(n,\alpha)^{7}Li$ dose component. Samples irradiated with photons are positioned in the central wells of the multi-well plate to deliver a dose as uniform as possible to each RHE. For each irradiation, some samples are selected as the control (indicated as *CTRL*). They undergo the same procedure as the other samples (except for boron administration, but receiving the PBS washing), including the transport at the irradiation facility, where they are not irradiated (Figure 5.1). Therefore, they allow estimating the damages of tissues due to factors other than radiation and provide the normalisation conditions to assess the irradiation effects. Samples irradiated with neutrons (both neutrons only and neutron in presence of boron) are transferred, immediately after the exposure, in a new multi-well plate containing fresh culture medium. In fact, the exposure to neutrons causes the activation of some of its components, such as Cl and Na. Radioactive medium must be stored at the reactor and plates with fresh medium are carried to the biology laboratories for the radiobiological analysis.

In the set of experiments described in this work, neutron dose was assessed in order to span a reasonable range. It is not trivial to plan a set of dose values because in BNCT the dose depends especially from boron component, and boron concentration can vary up to 300%, as shown in Chapter 2. Moreover,

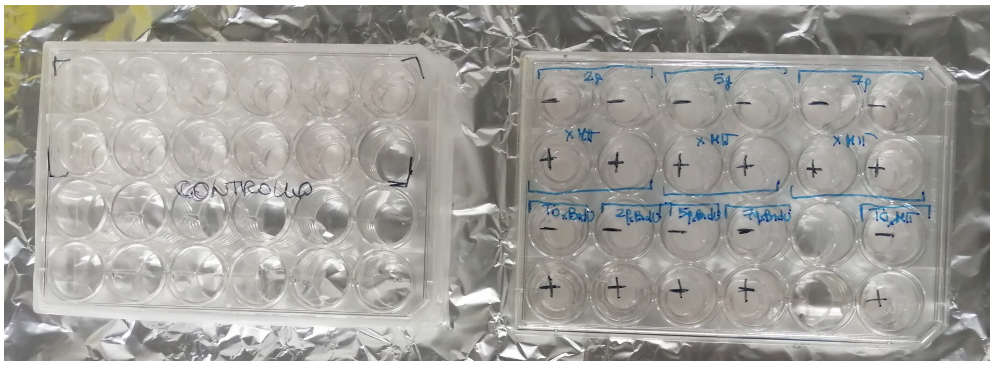

Figure 5.1: Multi-well plates containing samples before neutron irradiation. The marks on each well indicate the assay to be performed and the observation time. Control samples are in the plate on the left: they do not undergo irradiation, but they are washed and transported at the irradiation facility.

boron concentration in samples irradiated in a specific experiment are known only few days after the irradiation itself. Thus, reactor power and irradiation times were decided *a-priori*, and then dose was calculated using the dose rate components obtained by simulation (Chapters 3.4 and 3.5).

Table 3.13 reports the dose rate of each dose component in BNCT and neutron-only irradiation, per unit of reactor power. Considering the boron concentration in samples, the power at which reactor worked and the irradiation time for each irradiation performed, the total dose is:

$$D_T = (d_B \cdot B + d_p + d_s + d_\gamma) \cdot T_{irr} \cdot P \tag{5.2}$$

where

- d_B = dose rate per kW and per ppm of boron due to $^{10}B(n,\alpha)^7Li$ reaction (in Gy/kW·s);
- B = boron concentration in the sample obtained as described in Section 2 (in ppm);
- d_p = dose rate per kW due to 583 keV protons and 42 keV recoil ^{14}C arising from $^{14}N(n,p)^{14}C$ reactions (in Gy/kW·s);
- d_s = dose rate per kW due to hydrogen recoil nuclei from $^1H(n,n')^1H$ reactions (in Gy/kW·s);
- d_γ = dose rate per kW due to all photons in the problem;

$\mathbf{I}_n$	**P(kW)**	$\mathbf{T}_{irr}$ **(s)**
1	100	600
2	100	1200
3	250	1200
4	250	2400

Table 5.1: Irradiation time and reactor power for each neutron irradiation of RHE samples. The irradiation number (I_n) is a practical indexing to identify the experiments.

- P = reactor power (in kW);

- T_{irr} = irradiation time (in s).

Table 5.2 reports the total absorbed dose for each neutron irradiation experiment. Results are divided into two columns: *BNCT* and *Neutron Only*. The first refers to the dose delivered to samples that underwent BPA administration, whereas the second refers to dose delivered to samples irradiated without boron. The latter is obtained from equation 5.2 imposing boron concentration equal to 0. The indexing used in Table 5.1 and Table 5.2 were used together with Table 2.1 in Chapter 2 to calculate dose. For example, samples that absorbed 53 ± 4 ppm of boron were irradiated for 600 s with a reactor power of 100 kW and received a total dose of 21.0 ± 0.3 Gy.

For what concerns photon irradiation, nominal doses were corrected on the basis of the results of the simulations described in the previous Chapter. Table 5.3 shows the corrected absorbed dose in each irradiation session.

5.3 Histological analysis

5.3.1 Material and methods

Histology is the branch of biology which studies the microscopic structure of biological tissues and the functional and structural relationship between their individual components. The microscope is the main tool used to make direct observation of the morphological and structural characteristics of the tissues and samples must be treated in several ways before they can be observed [45]. First of all, they must undergo the fixation process. It consists

I_n	Dose component (Gy)				Total dose (Gy)	
	$^{10}B(n,\alpha)^7Li$	$^{14}N(n,p)^{14}C$	$^1H(n,n')^1H$	total γ	BNCT	Neutron Only
1	(18.7 ± 0.3)	(1.32 ± 0.02)	(0.1839 ± 0.008)	(0.76 ± 0.02)	(21.0 ± 0.3)	(2.27 ± 0.03)
2	(33.1 ± 0.5)	(2.65 ± 0.04)	(0.37 ± 0.02)	(1.52 ± 0.03)	(37.7 ± 0.5)	(4.54 ± 0.05)
3	(21.2 ± 0.3)	(6.6 ± 0.1)	(0.92 ± 0.04)	(3.81 ± 0.08)	(32.5 ± 0.3)	(11.4 ± 0.1)
4	(137 ± 2)	(13.2 ± 0.2)	(1.84 ± 0.08)	(7.6 ± 0.2)	(160 ± 2)	(22.7 ± 0.3)

Table 5.2: Total dose components in neutron irradiation. Column labelled with *BNCT* indicates the total dose in neutron irradiation in presence of boron. Column labelled with *Neutron only* refers to the total dose in irradiation without boron. These are obtained as the sum of $^{14}N(n,p)^{14}C$, $^1H(n,n')^1H$ and total γ dose components. Reported errors are standard deviations of the mean over the RHE samples in the wells. I_n indicates the corresponding combination of power and irradiation time listed in Table 5.1 and the corresponding mean boron concentration in samples treated with BPA listed in Table 2.1 of Chapter 2.

Irradiation number	Dose (Gy)
1	6.0 ± 0.3
2	12.0 ± 0.6
3	24 ± 1
4	36 ± 2
5	108 ± 5

Table 5.3: Doses absorbed by RHE samples in photon irradiation. Reported errors correspond to relative errors of 5%, as indicated in Raycell® Mk2 informative brochure.

in a treatment with chemical compounds (such as alcohol and formalin) that avoids or retards the decomposition process, fixing the tissue structure components in the chemical state and in the position in which they are found *in vivo* [46]. Then, samples are included in more resistant materials such as paraffin wax [45], which acts as a support for the sectioning of the tissues. To be viewed under an optical microscope, the tissues must be sectioned and the sections must be thin enough to allow the light transmission. Thickness ranging from few micrometers and dozens of micrometers can be obtained using a microtome. To be included, samples must be dehydrated because substances used in the inclusion process are apolar, whereas cells are composed predominantly by water, which is polar. To ensure the paraffin wax penetration in the samples it is thus necessary to remove the water [46]. Commonly dehydration is obtained through a series of solution with an ascendant concentration of alcohol, followed by a washing in xylene to remove alcohol residues. The last step is the staining of sections. In fact, biological tissues have in most cases little inherent contrast, resulting almost transparent under the microscope light. Staining can be used also to underline structures or particulars of interest. To show the general structure of the tissues hematoxylin and eosin staining is one of the most widespread techniques. It is a bichromatic staining, based on the different pH value of different tissues and organelles constituting the cell. In particular, the nucleus is acid and it is coloured in blue/purple by the hematoxylin, which is a basic dye, while the cytoplasm and organelles are basic an they are coloured by the eosin (that is acid) in shades of pink, more or less intense [46]. Since paraffin wax is water-repellent and both hematoxylin and eosin are aqueous dyes, it is necessary to remove the paraffin from the samples with xylene or some non-toxic solvent of vegetable origin. Then samples are re-hydrated through a descending scale of alcoholic solutions and stained with hematoxylin and eosin. Finally, through an ascending scale of alcoholic solutions samples are dehydrated again in order to fix the staining and preserve the samples over time, washed from alcohol with xylene and mounted on glass slides with cover-slips using a balsam as an adhesive [46].

The purpose of our histological analysis was to understand the characteristics of the model, to explore differences between batches and to observe morphological or structural changes induced by the irradiation in skin. To evaluate these changes we measured the total sections thickness, the thickness of the dead layer (stratum corneum) and the thickness of the whole vital

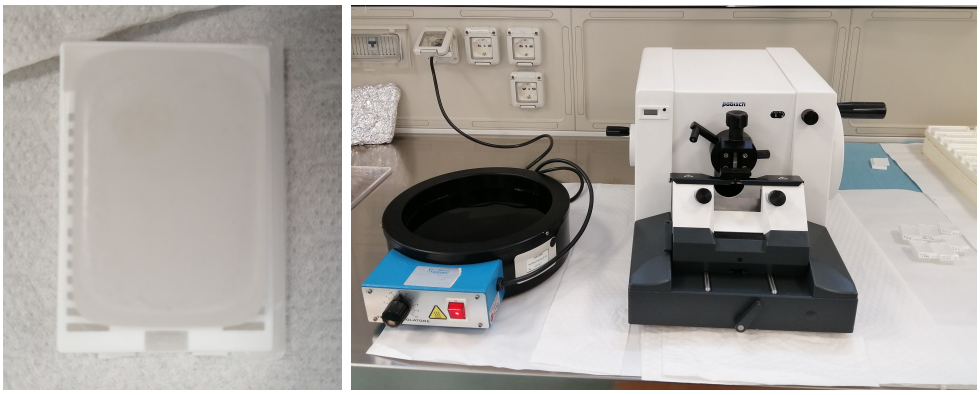

Figure 5.2: Example of RHE tissue included in paraffin wax (left) and microtome used for samples sectioning (right).

layer (which includes the basal, the spinous and the granular layers), for each delivered dose and at each observation time (including non-irradiated control samples).

After irradiation, samples were maintained in the fresh culture medium, changed every 24 hours, until the desired observation times, when they were fixed in formalin. After fixation, tissues were included in paraffin wax. The fixation process lasted three days. In the first two days samples were dehydrated through a series of solutions ascending in concentration of alcohol, used for different times: 50-50 alcohol-water solution for 1 hour, 70-30 for an hour and a half, 80-20 overnight, 95-5 for two hours and absolute alcohol for 3 hours. Then samples were washed in xylene for 30 minutes, deposited in appropriate trays containing melting paraffin wax at 48 °C for 1 hour and at 58 °C overnight. Then the trays were cooled to let the paraffin wax solidify and the sample to be detached from the support structure. Once removed from the plastic support, the included samples were sectioned with the microtome, cutting transverse slices 6 μm thick, in a way that each section showed all skin layers, and finally laid on glass slides (Figure 5.2).

After dried, samples were stained with hematoxylin and eosin (Figure 5.3). The ascending and descending scales of alcoholic solutions were prepared and hematoxylin was filtered to remove possible impurities or thickenings that could alter the staining. Slides were first immersed in xylene two times for 3 minutes to dissolve the paraffin wax and then in a solution 50-50 absolute alcohol and xylol for 2 minutes. After that, slides passed through the descending scale of alcoholic solutions (from a solution 100% alcohol to a

Figure 5.3: Left: example of a staining procedure step. Right: example of transverse sections of a RHE, stained with H&E stain.

solution of only 100% distilled water). At the end of this scale, samples were maintained for 10 minutes in hematoxylin, washed under running water for 10 minutes, maintained in eosin for 10 seconds and washed in distilled water for a few seconds. Then samples were treated with the ascending scale of alcoholic solutions (from 100% distilled water to 100% alcohol) and washed in xylene two times, the first one for 2 minutes and the second one for about 10-15 minutes. Finally, glass slides with stained samples were covered with cover-slips using a balsam as an adhesive (Figure 5.3).

Glasses were observed at the Olympus trinocular optical microscope with magnification 40x. Pictures of sections were acquired with the Olympus digital camera positioned in the appropriate microscope ocular. Then pictures were transferred to a computer where they were analysed with the image processing program ImageJ[5] [47]. This software allowed measuring the physical thicknesses of interest in RHE tissues after a proper calibration procedure. To calibrate, a picture of a ruler was taken at the microscope, with the same magnification of the sections images (40x). A known distance on the ruler picture was entered in the calibration program tool in order to set the right pixel/length scale (Figure 5.4). Once calibrated, the software provides directly a measurement of the selected distance in the desired unit.

[5]ImageJ is a software developed by the National Institutes of Health of the United States

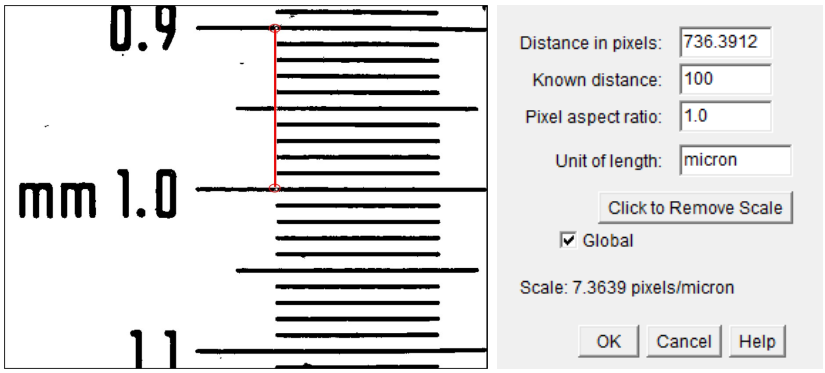

Figure 5.4: Calibration process of the ImageJ software [47]. Left: picture of the reference ruler (40x). Right: program calibration tool. The red line (left) represents the physical length to be measured. The value is manually entered in the field *known distance* on the right to calibrate.

Possible inaccuracies in the calibration procedure are due to the width of the ruler notches; moreover, the segment traced to set the calibration, was drawn by hand. These inaccuracies entail a systematic error in measurements, quantified as:

$$\Delta_{rel} = \frac{(L_{max} - L_{min})}{L} = 0.04 \tag{5.3}$$

where L is the measurement of the calibration segment and L_{max}, L_{min} are respectively the maximum and minimum possible lengths, considering the notches width.

The first measurement was the thickness of the polycarbonate filter and the average RHE thickness using different samples in a batch. These dimensions were used as representative evaluations for MCNP dosimetry simulations (Chapter 3 and Chapter 4). Results are expressed as:

$$\text{mean} \pm \text{standard deviation of the mean} \pm \text{systematic error}$$

We obtained:

- Total RHE thickness = $(106.2 \pm 2.0 \pm 0.3)\mu$m;
- Polycarbonate filter thickness = $(17.44 \pm 0.3 \pm 0.06)\mu$m;

The standard deviation of the mean shows that inside the same batch the variability is very low. Moreover, the Company ensures a certain regularity

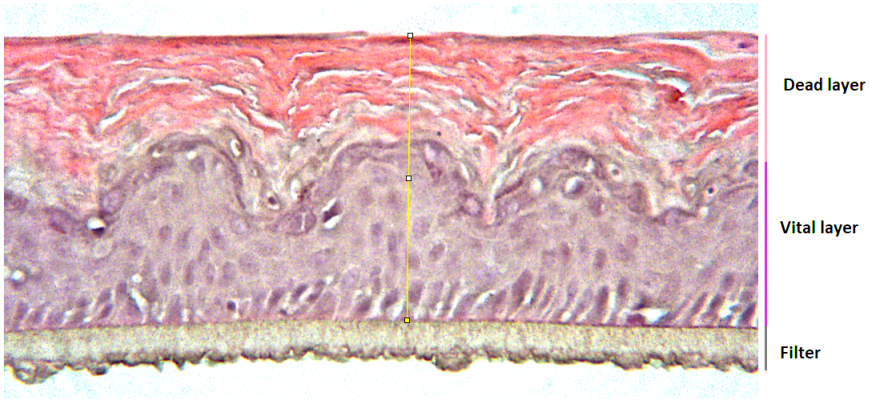

Figure 5.5: Example of a total RHE thickness measurement on a single RHE transversal section. The yellow line represents the physical distance to be measured.On the right, the dead layer, the vital layer and the filter are indicated as a reference.

between different batches, in order to have a reproducible model. However, biological variability may affect the total thickness and the thickness of each cell layer in samples of different batches.

For treated RHE, thickness was measured in different positions in the same section, averaging the results (Figure 5.5).

Then, thickness values of different RHE sections at the same observation time and treated with the same protocol were averaged again. This procedure gave the mean average thickness of each cell layer (vital and dead) and the mean total thickness for each RHE. The polycarbonate filter had a thickness quite regular in each sample, of about 15 μm.

5.3.2 Results

To explore the characteristics of the model and to compare different batches, non-irradiated samples at T0 observation time were observed. Figure 5.6 shows the histological sections corresponding to three different batches of the described experiments. Since for each experiment a different batch was used, batches are labelled with the same index used in Table 5.2: for example, samples of batch number 2, irradiated with neutron only, received a dose of 4.54 ± 0.05 Gy, while samples of the same batch receiving BNCT irradiation, absorbed a dose of 37.7 ± 0.5 Gy.

Batch number	Mean vital layer thickness (μm)	Mean dead layer thickness (μm)	Mean total thickness (μm)
2	$67.8 \pm 2 \pm 0.2$	$11.04 \pm 0.7 \pm 0.04$	$78.8 \pm 2 \pm 0.2$
3	$83.9 \pm 2 \pm 0.3$	$48.1 \pm 0.9 \pm 0.2$	$132.0 \pm 2 \pm 0.3$
4	$75.3 \pm 1 \pm 0.3$	$61.4 \pm 2 \pm 0.2$	$136.7 \pm 3 \pm 0.4$

Table 5.4: Average vital layer, dead layer and total thicknesses of non-irradiated (CTRL) samples belonging to different batches at T0. Results are expressed as described in Subsection 5.3.1.

The average thicknesses (excluding the filter) of CTRL samples are reported in Table 5.4.

Table 5.4 and Figure 5.6 show a certain variability between RHEs of different batches. For example, the sample in Figure 5.6-top has a predominant vital layer compared to the total thickness. Moreover, this has the smallest total thickness. On the contrary, the sample in Figure 5.6-bottom has a total thickness that is almost twice the first one, but about half of it consists of stratum corneum. The stratum corneum, among others functions, acts as a protective layer for the vital parts of the skin. The effects of the irradiation may be different according to the relative thickness of dead and vital layers. These differences among batches is important because all the results must be normalised to the corresponding control, especially when analysing irradiated samples at long observation times.

Then irradiated samples were analysed. The images for 4 observation times and for 6 dose values were inter-compared, for BNCT and neutron-only irradiation. Following, some examples are shown, chosen because they are representative of the observed effects.

Figure 5.7 and Figure 5.9 at T0, compared respectively with Figure 5.6, top and bottom, show that radiation effects at 0 days are not yet visible in samples: the vital layer has remained practically unchanged and the tissues appear well compact. Two days after irradiation, no substantial differences in the total structure of the tissues are noticeable, but the vital layers begin to decrease in thickness in both cases, in favour of an increase in the dead layers. Five days after the irradiation, considerable damages can be observed in samples that absorbed a high total BNCT dose: the RHEs are almost

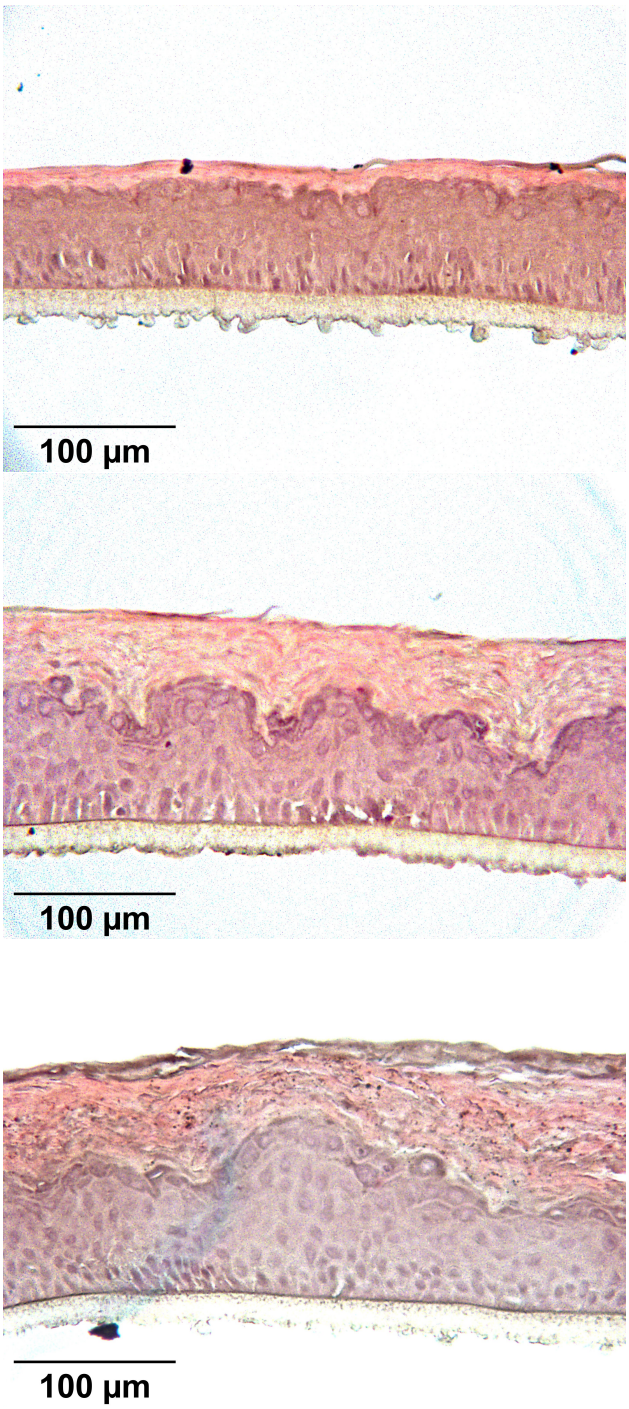

Figure 5.6: Histological sections of three non-irradiated samples at T0, belonging to: batch number 2 (top), batch number 3 (middle) and batch number 4 (bottom).

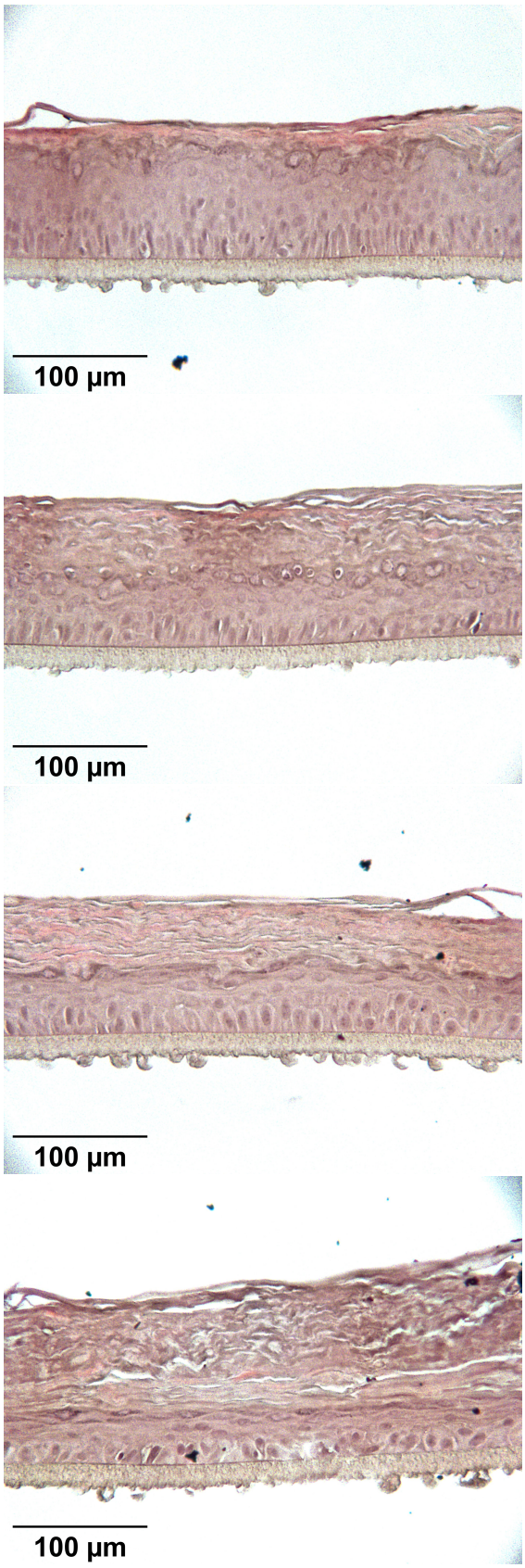

Figure 5.7: histological sections of samples irradiated with NO (4.54 ± 0.05 Gy). From top to bottom: observation time of 0, 2, 5 and 7 days.

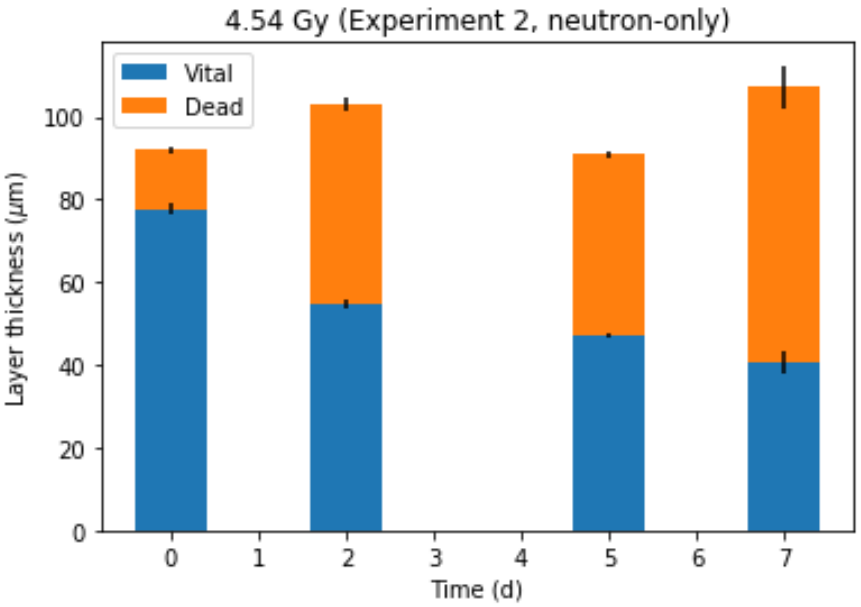

Figure 5.8: Vital layer (blue), dead layer (orange) and total (blue+orange) thicknesses, averaged over all the samples shown in Fig.5.7. Thickness are shown for different observation times (0, 2, 5 and 7 days).

totally deconstructed, with no vital layer and no division between layers, which merge into a single dead layer (Figures 5.9, T5 and Figure 5.10). On the contrary, at the same observation time, samples absorbing a neutron-only dose of 4.54 Gy appear more structured. The whole structure is still compact and the vital layer is well distinguishable, with thickness only slightly reduced (Figure 5.7, T5 and Figure 5.8). At T7 the same differences can be noticed: samples which underwent BNCT appear completely deconstructed and flaked (Figure 5.9, bottom), while vital layer is still distinguishable in the samples receiving neutron only irradiation (Figure 5.7, bottom). However, damages begin to be evident also in this case: the structure is less compact and the dead layer increases considerably at the expense of the vital one.

The same trend of morphological and structural changes described above was noticed in the other samples, at different doses. In particular, the thicknesses of the vital layer decreases as a function of the dose, while the thickness of the dead layers increases. Evident damages in the structure, which become chaotic and not well defined, consisting basically only of dead tissue, are visible at 5 and 7 days for all doses delivered. Tissues exposed to lower doses and with neutron only appeared less damaged than tissues receiving

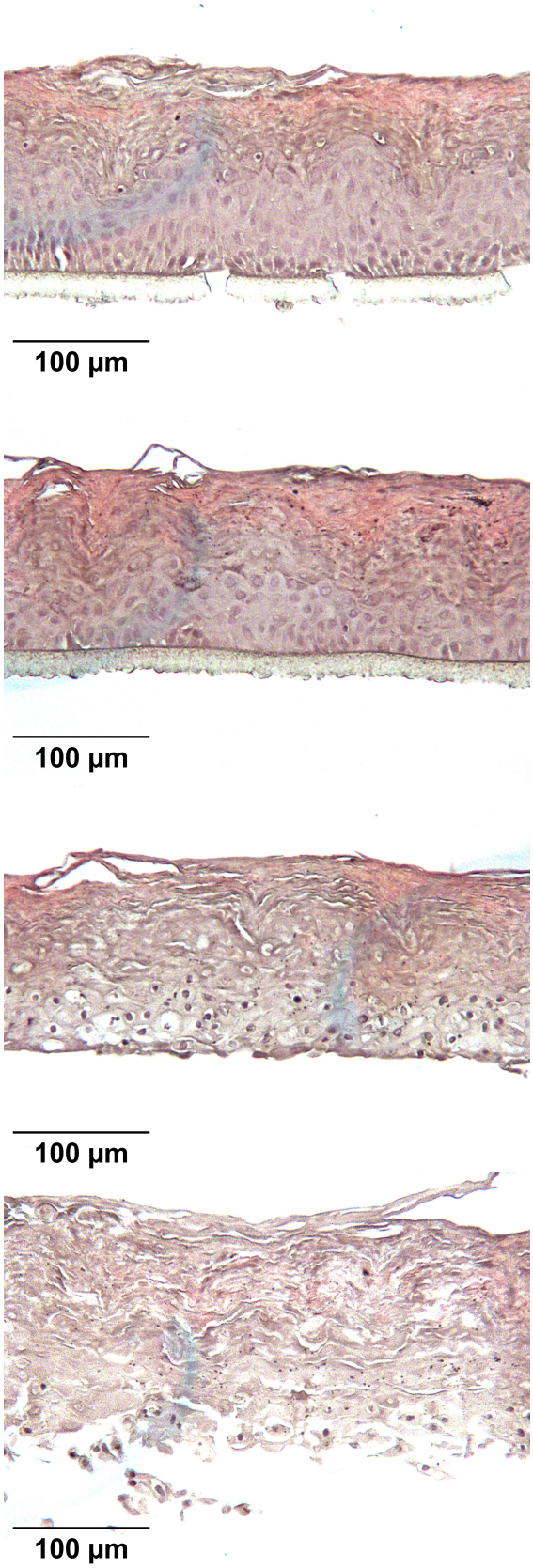

Figure 5.9: Histological sections of samples treated by BNCT (160.0 ± 2.0 Gy). From top to bottom: observation time of 0, 2, 5 and 7 days.

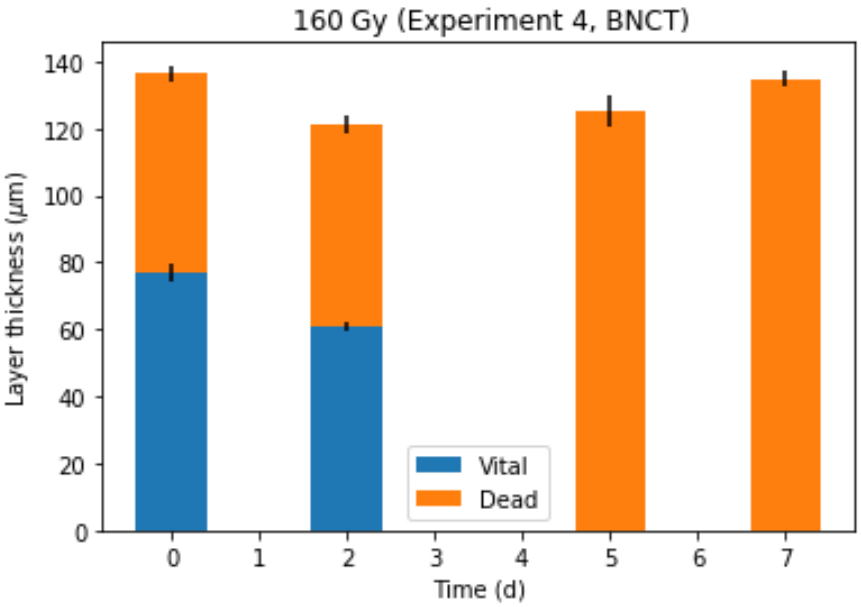

Figure 5.10: Vital layer (blue), dead layer (orange) and total (blue+orange) thicknesses, averaged over all the samples shown in Fig.5.9. Thickness are shown for different observation times (0, 2, 5 and 7 days).

higher BNCT doses (see below).

After this qualitative evaluation, further studies are necessary. First, the histology of the samples irradiated with photons will be stained and analysed in the same way. Then, we aim at identifying a method to quantify these changes in morphology and structure, to obtain an objective evaluation of radiation damage in the healthy skin. In collaboration with biologists experts in skin, significant parameters will be plotted as a function of the dose to draw conclusions on the different effects produced in skin by photon, neutrons and neutrons in presence of boron at the same dose values.

5.4 MTT assay

5.4.1 Materials and Methods

The 3-(4,5-dimethylthiazol-2-yl)-2,5-diphenyl tetrazolium bromide (MTT) is a colorimetric assay that allows detecting living cells in biological samples, i.e. cells that are metabolically active [48]. Mitochondrial respiration is the

most important step of the cell metabolism. It consists of a set of reactions and processes during which nutrients, reduced by digestion to elementary components (such as simple sugars, amino acids etc.), are demolished into simpler molecules obtaining energy available to the cell in the form of adenosine triphosphate (ATP). Cells with active mitochondria are able to complete their respiration cycle, so they are active, living cells. MTT assay measures the mitochondrial respiration efficiency in biological samples, so it indirectly provides the cell viability too. In fact, it is based on the capacity of active mitochondria of reducing the MTT salt (that is yellow) in water-insoluble formazan crystals (purple), which can be dissolved in many solutions, such as DMSO, SDS, and isopropanol [48, 49]. Since mitochondria activity is constant for most viable cells, the number of crystals formed in a sample (and dissolved in the isopropanol solution) is proportional to the number of cells surviving the irradiation [48]. Thus, an increase in colour intensity of the solution is associated to an increase in living cells. On the contrary, in dying or suffering cells mitochondria are inactive (or weakly active) and MTT is not reduced, causing a lower colour intensity in the solution. Crystals amount can be determined by measuring the associated absorbance by means of a microplate reader. The absorbance is a physical adimensional quantity that represents the amount of light absorbed by an object irradiated with a certain photon source. It is defined as [50]:

$$A = -\log_{10}(I/I_0) \tag{5.4}$$

where I is the intensity of light transmitted through the sample and I_0 is the intensity of the light source, in the same position, detected without the sample.

A microplate reader is a spectrophotometer that allows irradiating the samples, positioned in a multi-well plate, with a source emitting photons in a selected wavelength (in the range of UV or visible). Photon detectors (for example photomultipliers, photodiodes or similar) are located on the opposite side of the light source and, after a measurement of the light intensity without the multi-well plate, the transmitted light through the interposed samples is measured. The instrument, connected to a computer, provides directly the absorbance of all samples in the multi-well plate, maintaining the corresponding position in a matrix of values.

MTT assay protocol was applied to a dedicated number of RHE samples,

irradiated and non-irradiated (CTRL), for neutron and photon dose and for each observation time. Concerning the experiment with photons, samples underwent the whole MTT protocol, but until now it was only possible to analyse the response of the CTRL samples. After irradiation, the medium was replaced every 24 hours and RHE tissues were maintained in the incubator until specified observation times, when the MTT assay was performed. At these times, samples were washed twice with PBS (Phosphate Buffered Saline), positioned in wells containing 300 μl of a solution 1 mg/ml of MTT in culture medium and maintained in incubator at 37 °C for 2.30 hours. After the incubation time, MTT solution was removed and samples were washed again two times with PBS to remove non reduced MTT residues. Then, 700 μl of isopropanol were added in each well, both under and above the well membrane (on which the RHE tissue lays), and the multi-well plate was kept in agitation for about 2 hours to dissolve the formazan crystals previously formed. This procedure also dissolves completely the RHE tissues. Pure isopropanol (700 μl) was positioned in empty wells, constituting the so-called blank wells. The average absorbance measured in correspondence of the blank wells represents the absorbed light by the plate material and the isopropanol solution. This value, averaged over all blanks, is a background that must be subtracted from the measurement of the treated RHE. After the crystals dissolution, well membranes were broken to properly blend the solution (Figure 5.11) and 200 μl were transferred from each well in a new multi-well plate (including the pure isopropanol and maintaining the position inside the plate). The plate was positioned in the *Bio-Rad Model 680 microplate reader* and absorbance measurements were performed at a wavelength of 540 nm. This spectrophotometer can emit light in the wavelength spectrum ranging from 400 nm up to 750 nm by means of a tungsten halogen lamp. Transmitted light is detected by 8 silicon photodiodes with a resolution of 0.001 in absorbance and a photometric range from 0 to 3.5 [51].

For each dose point, the viability was obtained as:

$$S = \frac{\sum_{i=1}^{N}(A_i - \overline{A}_b)}{N \cdot \overline{A}_{ctrl}} \tag{5.5}$$

where:

- A_i is the absorbance measured in correspondence of the well i;
- $\overline{A}_b$ is the average absorbance of the blanks;

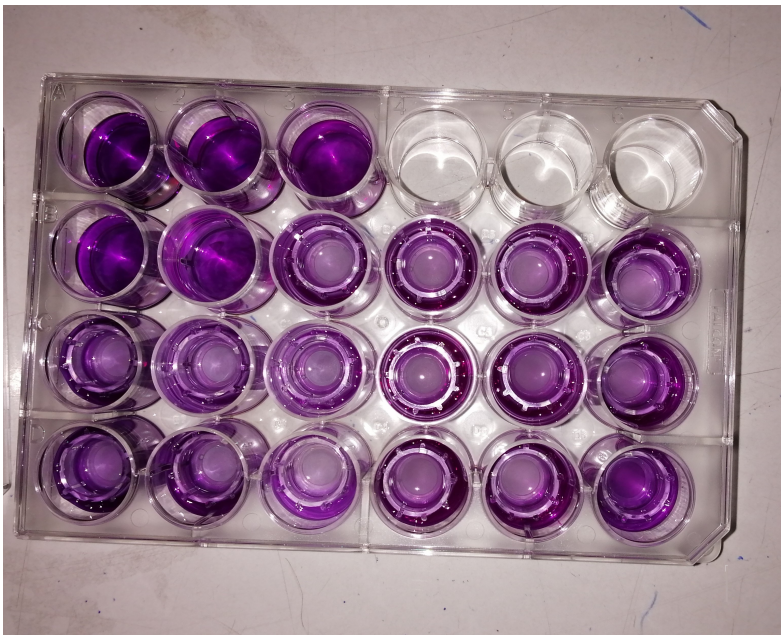

Figure 5.11: Example of MTT assay on RHE samples. Crystals are dissolved in isopropanol, leading to different shades of blue/purple. Some of the well membranes are already broken.

- N is the total number of samples, excluding the blanks and the control ones;

- $\overline{A}_{ctrl}$ is the average absorbance of the control samples.

5.4.2 Results

The first evaluation was the viability of the CTRL samples along the observation times for each batch. The results are reported in Figure 5.12. Results were normalised to 1 by dividing the absorbance by the value of the correspondent CTRL sample at T0. The behaviour of these curves shows that there is no clear trend of viability decrease as a function of time in 7 days. On the contrary, some batches showed a better viability in the longer observation times. This fact may be considered as a statistical biological variability between different samples. Values of viability showed that MTT measurement could be performed in this time range because the CTRL showed good response.

In the following curves, viability of treated cells was obtained by normal-

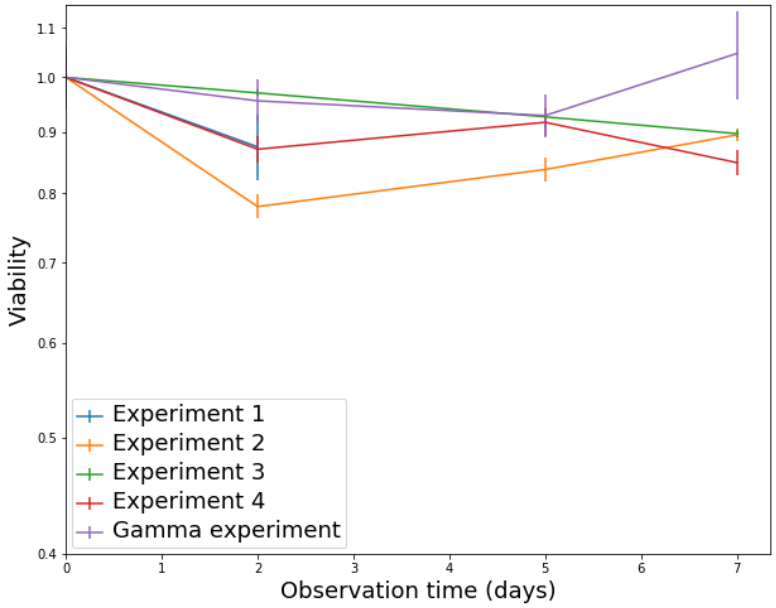

Figure 5.12: Viability of control samples, in neutron and photon experiments, along the observation times. Results are normalised to 1 at T0.

ising the measured absorbance by the absorbance of the corresponding CTRL (same treatment, same observation time), as described in Equation 5.5. This is important to take into account the batch differences and the damages of the samples due to the time from irradiation. The following curves represents thus the viability of the RHEs absorbing a given dose (Neutron Only or BNCT) at a given observation time, compared to the non-irradiated samples at the same time.

For each observation time viability results were condensed into two dose-effect curves: one related to the neutron only irradiation (NO) and one related to the neutron irradiation in presence of boron in samples (BNCT), shown in Figures 5.13.

Curves in Figure 5.13 do not reflect the same trend of the damage in tissues qualitatively observed in the histological samples, nor the well-known radiobiological effects of the neutron-only and the BNCT irradiation. First of all, the curves show a lower viability in samples irradiated with neutron-only, at all observation times. Secondly, viability at T0 and T2 increases for dose values higher than 37.7 Gy. However, histological observations (Subsection 5.3.2) confirm that BNCT is more effective than neutrons alone in causing damage in tissue, which increases with the absorbed dose. Therefore

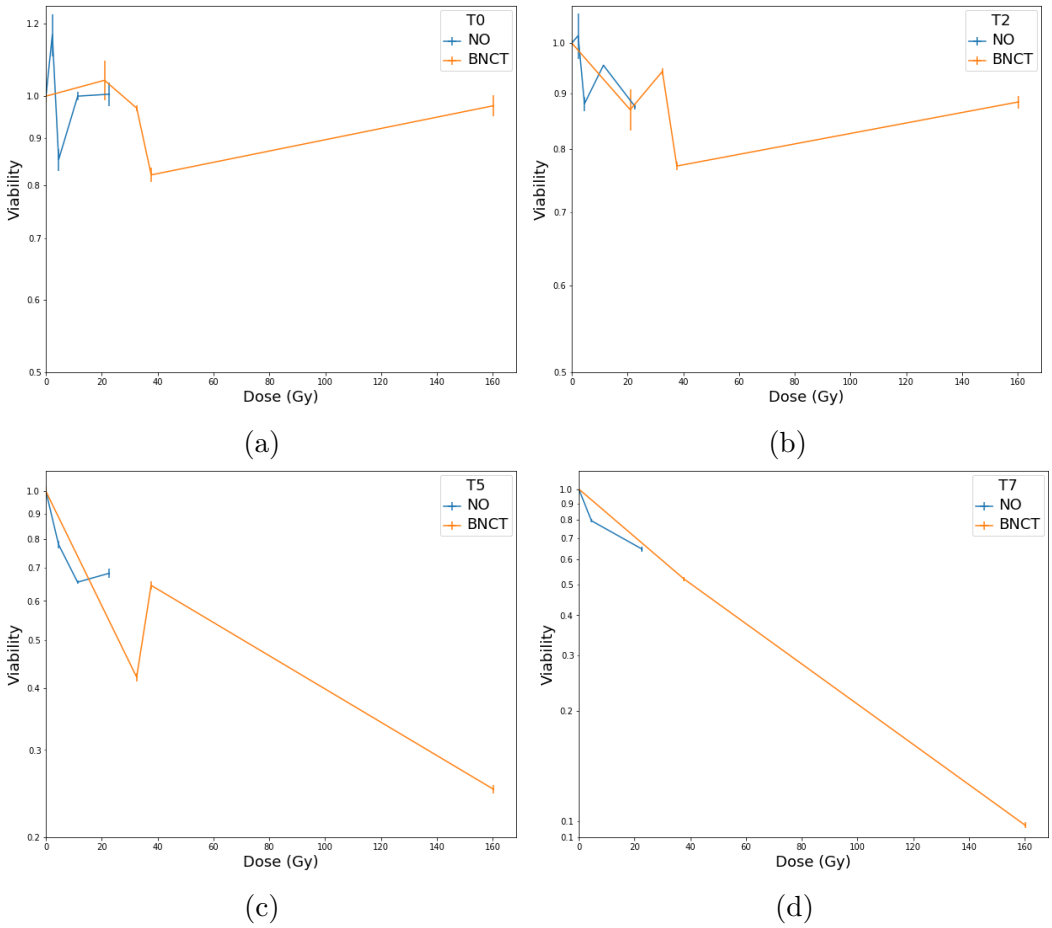

Figure 5.13: Viability of samples irradiated with neutron-only (NO) and with neutron in presence of boron (BNCT), obtained through the MTT assay, at different times: 5.13a at 0 days, 5.13b at 2 days, 5.13c at 5 days and 5.13d at 7 days.

the BNCT curve should be a monotonically decreasing function, with slope higher than that of the NO curve.

Hence the MTT curves thus obtained do not reflect the real tissue response. This led to questioning whether the dose values associated to each experiments were adequate. In particular, we analysed with more detail the boron concentration evaluations, which was possible after the observation of the histological sections of all the experiments.

Chapter 2 described how measurements were optimised to better represent the boron concentration and distribution in RHE samples. Since α particles and ^{7}Li-nuclei have a short range in tissue, with neutron autoradiography only tracks from the first 30-40 μm of the tissue laid on the CR-39 can be detected (see Chapter 1). Since the thickness of the stratum corneum, which faces the CR-39, can also be approximately 60 μm in CTRL samples, boron concentration measurements reported in Chapter 2 average over the stratum corneum alone. However, in the reasonable hypothesis that active cells in the inner layer uptake higher boron concentration, the described measurements may underestimate the actual boron concentration in these samples. To verify this hypothesis, a preliminary further analysis was made on one sample treated with BPA, to point out possible differences in boron distribution in the RHE layers. For this purpose, after boron treatment, RHE samples were frozen without any other inclusion material, which could drain boron out of the sample, and cut with a cryostat microtome, obtaining transverse sections such as the histological preparations. The thickness of sections was between 40 and 60 micron, as done before with other tissue taken from bioptic samples in animal experiments. Sections were laid on the CR-39 and irradiated in the Thermal Column of the rector. Before etching, CR-39 was used as an histological glass and stained with hematoxylin and eosin (as described in Section 5.3), to obtain the image of the layer structure in the same sections used to image boron distribution. The image of histology and the neutron autoradiografy were superimposed to verify which layer of the skin had absorbed more boron. Qualitative Results are shown in Figure 5.14.

Although it is only a preliminary evaluation requiring further work, Figure 5.14 clearly shows a region of about 50 μm with a higher concentration of tracks, corresponding to a higher concentration of boron in the vital layer of the RHE. Therefore, it constitutes a first confirmation of the initial hypothesis: boron measurements in RHEs made with the neutron autoradiography

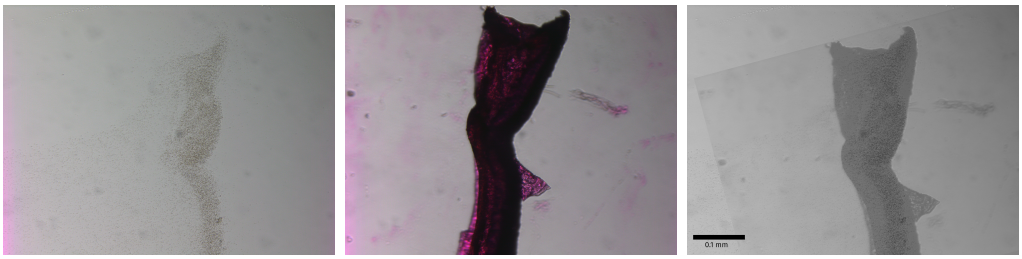

Figure 5.14: Left: qualitative neutron autoradiography of a non-irradiated transversal section of the RHE treated with boron, obtained with the cryostate microtome. Centre: Histology staining of the same sample. Right: overlap of the two images (histology and neutron autoradiography). The left profile of the autoradiography corresponds to the stratum corneum, while the right profile correspond to the vital layer and the filter. The area with higher tracks concentration corresponds approximately to the vital layer of the RHE.

technique may understimate the actual concentration in the samples. This hypothesis is also sustained by the analysis of boron concentration in comparison with the histological evaluation in all the batches. Highest concentration was found in the batch with the lowest stratum corneum. This supports the idea that, in that case, boron emerging from the vital layer was actually detected by neutron autoradiography.

For this reason, we plotted the viability as a function of the dose, recalculated assuming the same value of boron concentration, equal to the one measured in sample with the thinnest dead layer. The resulting curves are reported in Figure 5.15.

Curves in Figure 5.15 show a more adequate trend. In fact, BNCT curves at T5 and T7 decrease with the dose, even if at T0 and T2 they show fluctuations, still overall decreasing. Moreover, fixing a dose point for BNCT curves, it can be noticed that viability decreases as a function of time. This properly reflects the trend observed in histological samples. But BNCT curves still have a lower slope than NO curves. Although improved, these results are not representative of the tissue damage observed in histology, and further studies are obviously necessary to interpret the MTT results. First of all, it is necessary to acquire more points at higher doses for the NO curves and at lower doses for the BNCT ones, in order to obtain a more precise evaluation of their global trends. Moreover, assuming the same boron concentration, without considering that they come from different batches, is not

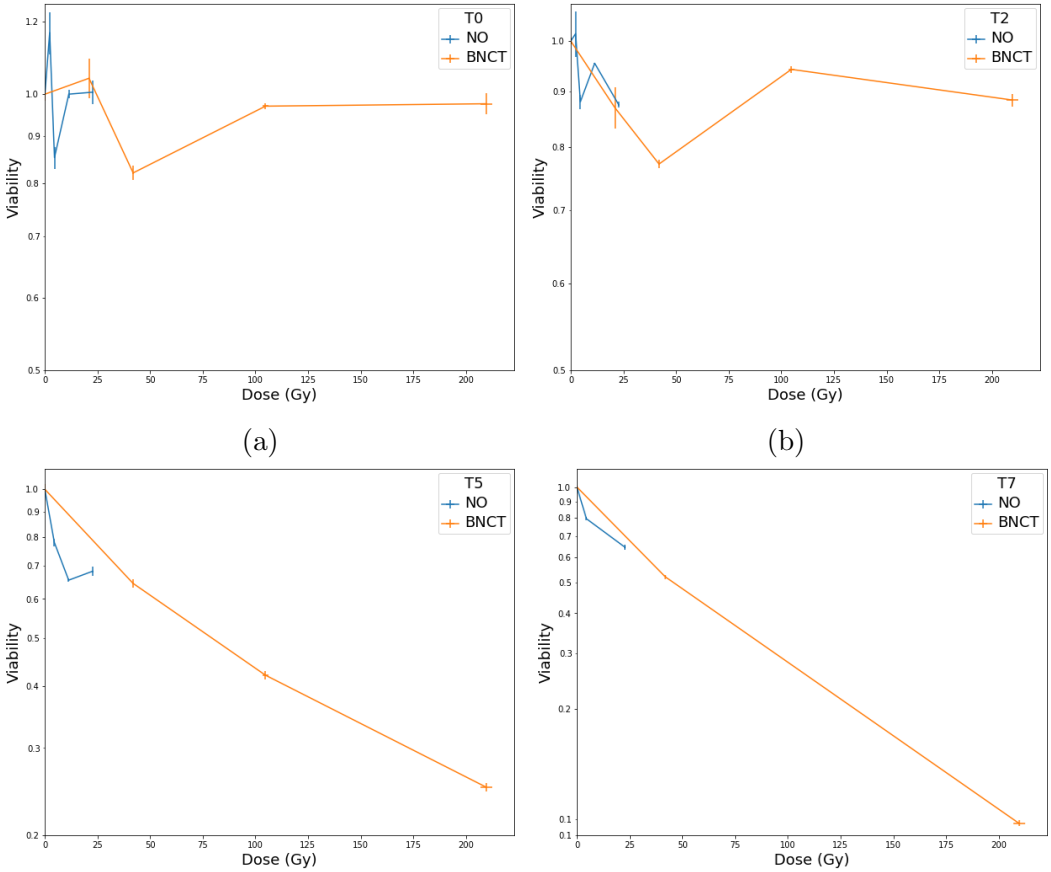

Figure 5.15: Viability of samples irradiated with neutron-only (NO) and with neutron in presence of boron (BNCT), obtained through the MTT assay, assuming a constant boron concentration in samples of 53 ppm, at different times : 5.15a at T0, 5.15b at T2, 5.15c at T5 and 5.15d at T7.

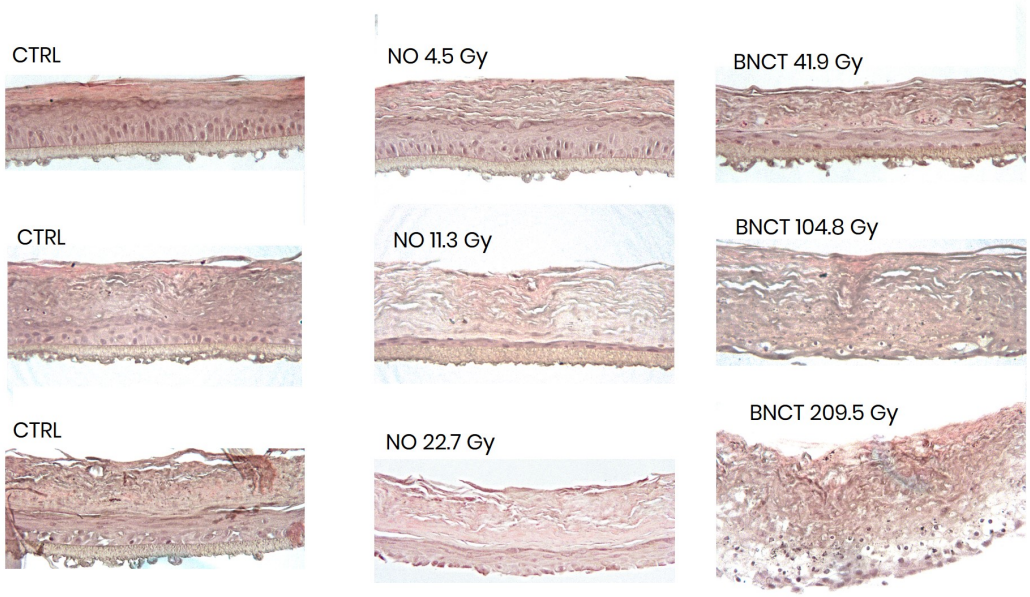

Figure 5.16: Histological sections of three different batches of RHE non-irradiated (CTRL), irradiated with neutrons (NO) and with neutrons after boron administration (BNCT). Absorbed dose is indicated. Observation time is 5 days.

precise enough. Therefore, actual boron uptake will be studied by optimising a method to point out boron in the different layers, in order to improve as much as possible the calculation of the dose delivered to RHEs.

Figure 5.16 shows a comparison of histological sections at the observation time of 5 days, showing that visible morphological alterations increase with dose, calculating BNCT dose with the same boron concentration.

It is worth noting that the MTT assay does not provide an evaluation of the damage in the tissues. In fact, it is able to reveal only the active cells at the time of the analysis, including those which, although active, have been damaged by radiation in their capacity of proliferation and which will go into apoptosis at the end of their cell cycle. For this reason, some RHE samples were prepared for the BrdU assay, that is a specific test to detect cells clonogenically active.

5.5 BrdU assay

The BrdU (Bromodeoxyuridine/ 5-bromo-2'-deoxiuridine) assay allows detecting proliferating cells in biological samples. It is based on the BrdU ability to bind the newly synthesized DNA of cells which are in the synthesis phase (S phase) of their cell cycle. In fact, BrdU is a synthetic nucleoside analog of the DNA precursor thymidine, which is composed by thymine (one of the DNA nucleobase) and the deoxyribose sugar. The DNA consists of a double helix of two complementary filaments. During the replication, that occurs in the S phase of the cell cycle, these are separated and each strand of the original DNA molecule serves as a model for the production of its complementary. The new molecule will consist of an original DNA strand and a newly synthesized strand. For this process, cells need to acquire from the outside all the elements necessary for the construction of the new DNA strands, such as nucleobases, sugars etc. If BrdU is added to the culture medium, S-phase cells will incorporate it into their DNA just as they would incorporate thymidine. BrdU will be transmitted to the daughter cells, halving with each duplication. The DNA-bounded BrdU can be detected by means of specific anti-BrdU monoclonal antibodies, able to recognise and bind to it. These antibodies are conjugated to a fluorophore that, when hit by light of a certain wavelength, exhibits fluorescence, thus providing an evaluation of the amount of proliferating cells in a cell culture or in tissue sections [52].

Some RHE samples for each dose and each observation time were dedicated and prepared to the BrdU assay, their analysis is presently underway. This assay is very important because it provides information that is more representative of the actual radiation damage in the RHE samples than the MTT results are. In fact, BrdU results provide an estimate of the amount of the cells in the sample that are not only vital, but also clonogenically active at the time of the compound administration, i.e. after the irradiation. Thus, damaged but active cells that will dye at the end of their cell cycle are not included in the BrdU response. Therefore, a consistent difference should be noticed between MTT and BrdU results. In particular, the BrdU should better reflect the histological observations in the skin, described in Section 5.3.2, showing a consistent damage in the structure and morphology of the samples as the dose and the observation time increases.

Chapter 6

Conclusions and future studies

This work represents a preliminary evaluation of the effects of BNCT in the healthy skin as a function of the dose. To this end, a Reconstructed Human Epidermis model (RHE) cultivated *in-vitro* was irradiated with neutron, with neutrons in presence of boron and with photons (reference radiation) at different doses. The work is motivated by the need of collecting robust biological data to develop dosimetry models, that are used to express BNCT mixed field dose in photon-equivalent units. In this way, it is possible to calculate safe and effective treatment plans based on the knowledge on dose-effects acquired in conventional radiotherapy. Skin is a very important tissue in BNCT, often limiting the dose that can be delivered to tumours. It is thus mandatory to produce accurate models to describe the effects of BNCT in comparison with those due to photon irradiation.

To study dose-effect relation, it is necessary to know as precisely as possible the dose absorbed by samples, and to assess the meaningful effects to be studied and the techniques to measure them. The Chapters 2, 3 and 4 of this thesis are dedicated to the first issue (dose), Chapter 5 describes the radiobiological evaluation of the effects.

Since the $^{10}B(n,\alpha)^{7}Li$ reaction is usually the most important component of the total absorbed dose in BNCT, it is fundamental to accurately assess the concentration of boron in the skin samples. Being the RHE a new model in BNCT, a protocol of boron administration was set-up, to optimise the uniformity of ^{10}B distribution in the sample. Measurements were performed by means of qualitative and quantitative neutron autoradiography. The results showed that the best uniformity and adequate boron concentration were obtained by exposing samples to the medium enriched with Boronopheny-

lalanine (BPA) for 4 hours.

For each BNCT treatment, boron concentration was measured in three RHE samples. Both qualitative imaging of boron distribution and quantitative determination of concentration were carried out. The results confirmed a high variability of boron uptake in different RHE batches: differences up to 300% were observed.

The dose absorbed by RHE models was computed with the MCNP6 code, modelling the TRIGA Mark II reactor and the gamma irradiator. BNCT dose calculation in the RHE is not trivial, for several factors: the mixed radiation field produced in tissue by neutron interactions, the background photon spectrum extending over a wide energy range, the small RHE dimensions, having a thickness between 100 and 150 μm, and the irradiation position quite far away from the neutron source. The dose calculation poses several challenges that must be addressed using computational strategies. First, it was necessary to set-up a robust variance reduction to allow efficient calculations, i.e. statistical convergence in acceptable calculation times. The second issue was the test of the validity of charged particle equilibrium (CPE) and electron equilibrium (CE) in the RHE. The CPE condition was found to be valid in the RHE volumes for charged particles arising from neutron interactions. Electrons required more efforts. In general, electrons are more difficult to be transported by MCNP because they require more calculation resources due to their frequent interactions. Furthermore, the electron dose calculation in MCNP does not allow any variance reduction technique. The electron calculation parameters were checked, in particular the default number of steps used in the condensed-history transport (ESTEP parameter). The default ESTEP value in the skin volume was analysed for both electrons and heavier charged particles. For electrons, having a larger range in tissue, the ESTEP must be increased to have an adequate electronic transport. Moreover, the influence of different ESTEP values on the dose calculation was investigated. No substantial differences were noticed for values higher than that established (less than or equal to 3%). Then, an evaluation of the most accurate electron transport method in the geometry was carried out. No substantial differences were noticed in doses computed using the default Condensed History transport method (with the adjusted ESTEP) and the Single Event method: a maximum percentage difference of only 3% was observed between the results. To allow the correct statistic in the RHE, a work on the simulation of the neutron/photon source was carried out. The source was transferred from

the reactor core to a series of surfaces surrounding the RHE samples using the SSW/SSR features of MCNP. In this way it was possible to transport secondary electrons from photons interaction and to calculate as precisely as possible the dose due to gamma in RHEs without the assumption of CE. On the basis of these results, total dose rates (charged particles from boron, nitrogen and hydrogen, gamma from background radiation and from capture in hydrogen) in samples were computed.

The X-ray irradiator, exploited to perform the photon irradiation of the RHE samples, is commonly used to sterilise blood bags, in which case CE is not an issue. In the RHE samples, the validity of the CE was studied. Moreover, the nominal dose delivered to the samples is determined on the basis of a calibration performed at the centre of the holder, while RHE are irradiated at the top. Dose variation along the holder was studied: results show that the dose varies consistently along the canister axis. Moreover, electron equilibrium does not hold in RHE samples. Overall, the actual dose absorbed in RHE is 20% higher than the nominal value; therefore, nominal photon doses were corrected by a factor of 1.20.

The results of these calculations highlight the necessity of an accurate evaluation of the physical conditions in the problem of interest, especially when dose is calculated in very small volumes. In fact, assuming equilibrium may cause large discrepancies between the calculated dose and the dose actually absorbed by the samples. For example, the assumption of the electron equilibrium in the RHE samples irradiated with neutrons only, leads to a 10% discrepancy compared to the correct value. These considerations becomes even more evident in smaller samples, such as monolayer cell cultures, for which this difference can be up to 30%. Such inaccuracies in the dose-effect curves, are propagated in the calculation of the RBE, and cause an incorrect evaluation of photon-equivalent dose, ultimately affecting the effectiveness of the treatment planning. Therefore, one of the most important results of this thesis is the assessment of an accurate dosimetry in the RHE samples.

To study the dose-effect relation in the skin, in addition to a precise dosimetry, it is necessary to determine the biological effects induced in the RHE tissues and to establish a method to measure them. Since the life of the samples is guaranteed only for a week, only acute effects can be observed after the irradiation. As a first approach, morphological and structural changes were investigated in the samples. Histological sections of irradiated and

control samples were prepared and a first quantification of the effect was realised by measuring the thickness of the vital and the dead layers. In fact, it was clear that the irradiation at high doses cause the decreasing of the vital layer and the deconstruction of the normal structure of the tissue. Moreover, cell viability was quantified by means of the MTT assay. The histological analysis and the MTT assay were performed at different times from the irradiation to explore the time evolution of the irradiation damage in the first days post-treatment.

To date, part of the experiment is still under analysis, for example the MTT of samples irradiated with photons. Samples were also prepared for the BrdU assay, which provides an estimate of the amount of proliferating cells in tissue, allowing a more representative evaluation of the actual tissue damage. Their analysis is presently underway.

The histological analysis of controls showed a certain variability in the RHE total thickness and in the layer thicknesses between samples of different batches, while no relevant differences were noticed between samples of the same batch. The vital layer thickness was found to decrease as a function of the dose for both neutron-only and BNCT irradiation, in favour of an increase in the dead layer one. Tissues exposed to lower doses and with neutron only appeared less damaged than tissues receiving high BNCT doses. Evident damages in the structure, which become chaotic and not well defined, consisting basically only of dead tissue, are visible at 5 and 7 days for all doses delivered. Until the second day from the irradiation, only a slight reduction of the vital layer was observed in most of the samples, without relevant damages in the structure.

These preliminary radiobiological evaluations, provided interesting insights for a further study on the distribution of boron in the tissue layers. In fact, the viability of cells have a behaviour non monotonically decreasing with dose. This posed the question whether boron measurement by neutron autoradiography was representative of the actual boron present in the inner depths of tissue sample. A qualitative neutron autoradiography was performed on transverse sections of RHE treated with BPA, actually showing a higher concentration of boron in the vital layer of the tissue. Although this is only a preliminary result, it suggests the necessity of a re-analysis of the radiobiological data, based on a more accurate evaluation of the boron concentration in the samples, and therefore on a more precise dosimetry. For example, the ^{10}B microdistribution in the RHE cell layers could be assessed

by means of high resolution imaging techniques, such as the one described by Kiger et al. [53]. Moreover, it will be necessary to perform some irradiation experiments at different doses to span more uniformly the dose range, in particular at lower dose values for BNCT treatment.

Together with a deeper evaluation of the results from the biological point of view, these experiments will produce complete dose-effect curves that can lay solid foundation for the construction of NTCP and photon iso-effective dose calculations.

Bibliography

[1] F Issa, JA Ioppolo, LM Rendina, J Reedijk, and K Poeppelmeier. *Boron and Gadolinium Neutron Capture Therapy*. Elsevier Amsterdam, 2013.

[2] Jeffrey A Coderre and Gerard M Morris. The radiation biology of boron neutron capture therapy. *Radiation research*, 151(1):1–18, 1999.

[3] Rolf F Barth, Jeffrey A Coderre, M Graça H Vicente, and Thomas E Blue. Boron neutron capture therapy of cancer: current status and future prospects. *Clinical Cancer Research*, 11(11):3987–4002, 2005.

[4] Rolf F Barth, Peng Mi, and Weilian Yang. Boron delivery agents for neutron capture therapy of cancer. *Cancer Communications*, 38(1):35, 2018.

[5] Masamitsu Ichihashi, Takafumi Nakanishi, and Yutaka Mishima. Specific killing effect of 10b1-para-boronophenylalanine in thermal neutron capture therapy of malignant melanoma: In vitro radiobiological evaluation. *Journal of Investigative Dermatology*, 78(3):215–218, 1982.

[6] H Fukuda, J Hiratsuka, C Honda, T Kobayashi, K Yoshino, H Karashima, J Takahashi, Y Abe, K Kanda, and M Ichihashi. Boron neutron capture therapy of malignant melanoma using 10b-paraboronophenylalanine with special reference to evaluation of radiation dose and damage to the normal skin. *Radiation research*, 138(3):435–442, 1994.

[7] Andres Juan Kreiner, Javier Bergueiro, Daniel Cartelli, Matias Baldo, Walter Castell, Javier Gomez Asoia, Javier Padulo, Juan Carlos Suárez Sandín, Marcelo Igarzabal, Julian Erhardt, et al. Present status of accelerator-based bnct. *Reports of Practical Oncology & Radiotherapy*, 21(2):95–101, 2016.

[8] Mona Zolfaghari and Mahmood Sedaghatizadeh. Design of thermal neutron beam based on an electron linear accelerator for bnct. *Applied Radiation and Isotopes*, 118:149–153, 2016.

[9] N Protti, S Bortolussi, Sabrina Stella, MA Gadan, A De Bari, F Ballarini, P Bruschi, C Ferrari, AM Clerici, C Zonta, et al. Calculations of dose distributions in the lungs of a rat model irradiated in the thermal column of the triga reactor in pavia. *Applied Radiation and Isotopes*, 67(7-8):S210–S213, 2009.

[10] G. Gambarini, S. Agosteo, P. Marchesi, E. Nava, P. Palazzi, A. Pecci, G. Rosi, and R. Tinti. Discrimination of various contributions to the absorbed dose in BNCT: Fricke-gel imaging and intercomparison with other experimental results. *Applied Radiation and Isotopes*, 53(4–5):765 – 772, 2000.

[11] D. R. White, R. V. Griffith, and I. J. Wilson. Report 46. *Journal of the International Commission on Radiation Units and Measurements*, os24(1):NP–NP, 04 2016.

[12] Sara J González and Gustavo A Santa Cruz. The photon-isoeffective dose in boron neutron capture therapy. *Radiation research*, 178(6):609–621, 2012.

[13] L Provenzano, H Koivunoro, I Postuma, JM Longhino, EF Boggio, RO Farías, S Bortolussi, and SJ González. The essential role of radiobiological figures of merit for the assessment and comparison of beam performances in boron neutron capture therapy. *Physica Medica*, 67:9–19, 2019.

[14] Silva Bortolussi, Ian Postuma, Nicoletta Protti, Lucas Provenzano, Cinzia Ferrari, Laura Cansolino, Paolo Dionigi, Olimpio Galasso, Giorgio Gasparini, Saverio Altieri, et al. Understanding the potentiality of accelerator based-boron neutron capture therapy for osteosarcoma: dosimetry assessment based on the reported clinical experience. *Radiation Oncology*, 12(1):130, 2017.

[15] SJ González, MR Bonomi, GA Santa Cruz, HR Blaumann, OA Calzetta Larrieu, P Menéndez, R Jiménez Rebagliati, J Longhino, DB Feld,

MA Dagrosa, et al. First bnct treatment of a skin melanoma in argentina: dosimetric analysis and clinical outcome. *Applied radiation and isotopes*, 61(5):1101–1105, 2004.

[16] FA Stewart, AV Akleyev, M Hauer-Jensen, JH Hendry, NJ Kleiman, TJ Macvittie, BM Aleman, AB Edgar, K Mabuchi, CR Muirhead, et al. Icrp publication 118: Icrp statement on tissue reactions and early and late effects of radiation in normal tissues and organs–threshold doses for tissue reactions in a radiation protection context. *Annals of the ICRP*, 41(1-2):1–322, 2012.

[17] Zheng Zhang and Bozena B Michniak-Kohn. Tissue engineered human skin equivalents. *Pharmaceutics*, 4(1):26–41, 2012.

[18] Christian Pellevoisin, Christelle Videau, Damien Briotet, Corinne Grégoire, Carine Tornier, Alain Alonso, Anne Sophie Rigaudeau, Charbel Bouez, and Nathalie Seyler. Skinethic™ rhe for in vitro evaluation of skin irritation of medical device extracts. *Toxicology in Vitro*, 50:418–425, 2018.

[19] L Cansolino, AM Clerici, C Zonta, P Dionigi, G Mazzini, R Di Liberto, S Altieri, F Ballarini, S Bortolussi, MP Carante, et al. Comparative study of the radiobiological effects induced on adherent vs suspended cells by bnct, neutrons and gamma rays treatments. *Applied Radiation and Isotopes*, 106:226–232, 2015.

[20] C. Ferrari, J. Bakeine, F. Ballarini, A. Boninella, S. Bortolussi, P. Bruschi, L. Cansolino, A. M. Clerici, A. Coppola, R. Di Liberto, P. Dionigi, N. Protti, S. Stella, A. Zonta, C. Zonta, and S. Altieri. In vitro and in vivo studies of boron neutron capture therapy: Boron uptake/washout and cell death. *Radiation Research*, 175(4):452–462, 2011.

[21] Jeffrey A Coderre, Eric H Elowitz, Manjeet Chadha, Richard Bergland, Jacek Capala, Darrel D Joel, Hungyuan B Liu, Daniel N Slatkin, and Arjun D Chanana. Boron neutron capture therapy for glioblastoma multiforme using p-boronophenylalanine and epithermal neutrons: Trial design and early clinical results. *Journal of neuro-oncology*, 33(1-2):141–152, 1997.

[22] MA Gadan, S Bortolussi, I Postuma, F Ballarini, P Bruschi, N Protti, D Santoro, Sabrina Stella, L Cansolino, A Clerici, et al. Set-up and calibration of a method to measure 10b concentration in biological samples by neutron autoradiography. *Nuclear Instruments and Methods in Physics Research Section B: Beam Interactions with Materials and Atoms*, 274:51–56, 2012.

[23] Ian Postuma, Silva Bortolussi, Nicoletta Protti, Francesca Ballarini, Piero Bruschi, Laura Ciani, Sandra Ristori, Luigi Panza, Cinzia Ferrari, Laura Cansolino, and Saverio Altieri. An improved neutron autoradiography set-up for 10b concentration measurements in biological samples. *Reports of Practical Oncology & Radiotherapy*, 21(2):123 – 128, 2016. 7th Young BNCT meeting.

[24] S Altieri, S Bortolussi, P Bruschi, P Chiari, F Fossati, Sabrina Stella, U Prati, L Roveda, A Zonta, C Zonta, et al. Neutron autoradiography imaging of selective boron uptake in human metastatic tumours. *Applied Radiation and Isotopes*, 66(12):1850–1855, 2008.

[25] George W Kabalka, Gary T Smith, Jonathan P Dyke, William S Reid, CP Desmond Longford, Tony G Roberts, N Kesavulu Reddy, Edward Buonocore, and Karl F Hübner. Evaluation of fluorine-18-bpa-fructose for boron neutron capture treatment planning. *Journal of Nuclear Medicine*, 38(11):1762–1766, 1997.

[26] L Menichetti, L Cionini, WA Sauerwein, S Altieri, O Solin, H Minn, and PA Salvadori. Positron emission tomography and [18f] bpa: a perspective application to assess tumour extraction of boron in bnct. *Applied Radiation and Isotopes*, 67(7-8):S351–S354, 2009.

[27] T Goorley, M James, Thomas Booth, F Brown, J Bull, LJ Cox, J Durkee, J Elson, Michael Fensin, RA Forster, et al. Initial mcnp6 release overview. *Nuclear Technology*, 180(3):298–315, 2012.

[28] S Bortolussi, N Protti, M Ferrari, I Postuma, S Fatemi, M Prata, F Ballarini, MP Carante, R Farias, SJ González, et al. Neutron flux and gamma dose measurement in the bnct irradiation facility at the triga reactor of the university of pavia. *Nuclear Instruments and Methods in Physics Research Section B: Beam Interactions with Materials and Atoms*, 414:113–120, 2018.

[29] S. Bortolussi, N. Protti, M. Ferrari, I. Postuma, S. Fatemi, M. Prata, F. Ballarini, M.P. Carante, R. Farias, S.J. González, M. Marrale, S. Gallo, A. Bartolotta, G. Iacoviello, D. Nigg, and S. Altieri. Neutron flux and gamma dose measurement in the bnct irradiation facility at the triga reactor of the university of pavia. *Nuclear Instruments and Methods in Physics Research Section B: Beam Interactions with Materials and Atoms*, 414:113 – 120, 2018.

[30] John R Lamarsh. *Introduction to nuclear reactor theory*. Addison-Wesley, 1966.

[31] LS Kothari and KS Singwi. Interaction of thermal neutrons with solids. In *Solid state physics*, volume 8, pages 109–190. Elsevier, 1959.

[32] F.H.Attix. *Introduction to Radiological Physics and Radiation Dosimetry*. WILEY-VCH Verlag GmbH & Co. KGaA, Weinheim, 2004.

[33] Matteo Ferrari. Characterization of the gamma dose component in the BNCT irradiation facility and dosimetry for in vitro experiments at the Triga reactor in Pavia. Master's thesis, Università degli studi di Pavia - Facoltà di scienze MM. FF. NN., Università degli studi di Pavia - Facoltà di scienze MM. FF. NN. 2012/2013, Supervisor Prof. Saverio Altieri, Co-supervisor Dott. Silva Bortolussi.

[34] Editor J.F.Briesmeister. *MCNP - A General Monte Carlo N-Particle Transport Code, Version 4C*, 2000 - LA-13709-M.

[35] Editor C.J. Werner. *MCNP User's Manual, Code Version 6.2*, 2017 - LA-UR-17-29981.

[36] Hanna Koivunoro, Teemu Siiskonen, Petri Kotiluoto, Iiro Auterinen, Eero Hippeläinen, and Sauli Savolainen. Accuracy of the electron transport in mcnp5 and its suitability for ionization chamber response simulations: A comparison with the egsnrc and penelope codes. *Medical physics*, 39(3):1335–1344, 2012.

[37] Rodolphe Antoni and Laurent Bourgois. Evaluation of the new electron-transport algorithm in mcnp6. 1 for the simulation of dose point kernel in water. *Nuclear Instruments and Methods in Physics Research Section B: Beam Interactions with Materials and Atoms*, 412:102–108, 2017.

[38] Dennis R Schaart, Jan Th M Jansen, Johannes Zoetelief, and Piet FA de Leege. A comparison of mcnp4c electron transport with its 3.0 and experiment at incident energies between 100 kev and 20 mev: influence of voxel size, substeps and energy indexing algorithm. *Physics in Medicine & Biology*, 47(9):1459, 2002.

[39] Nick Reynaert, Hugo Palmans, Hubert Thierens, and R Jeraj. Parameter dependence of the mcnp electron transport in determining dose distributions. *Medical physics*, 29(10):2446–2454, 2002.

[40] H Grady Hughes. Improved logic for sampling landau straggling in mcnp5. *Proc. Mathematics and Computation, Supercomputing, Reactor Physics, and Nuclear and Biological Applications, Palais des Papes, Avignon, France*, 2005.

[41] HG Hughes. Enhanced electron-photon transport in mcnp6 joint int. In *Conf. on Supercomputing in Nuclear Applications+ Monte Carlo'EDP Sciences*, page 03105, 2014.

[42] H Grady Hughes III. Quick-start guide to low-energy photon/electron transport in mcnp6. Technical report, Los Alamos National Lab.(LANL), Los Alamos, NM (United States), 2013.

[43] G Poludniowski, G Landry, F DeBlois, PM Evans, and F Verhaegen. Spekcalc: a program to calculate photon spectra from tungsten anode x-ray tubes. *Physics in Medicine & Biology*, 54(19):N433, 2009.

[44] SJ González, Emiliano César Cayetano Pozzi, A Monti Hughes, Lucas Provenzano, H Koivunoro, Daniel Germán Carando, Silvia Inés Thorp, MR Casal, Silva Bortolussi, Verónica Andrea Trivillin, et al. Photon iso-effective dose for cancer treatment with mixed field radiation based on dose–response assessment from human and an animal model: clinical application to boron neutron capture therapy for head and neck cancer. *Physics in Medicine & Biology*, 62(20):7938, 2017.

[45] HC Cook, JD Bancroft, and A Stevens. Theory and practice of histological techniques (2nd ed), Churchill Livingstone New York 1982.

[46] Pawlina Wojciech Ross, Michael H. *Histology: a text and atlas with correlated cell and molecular biology (7th ed.)*. Walters Kluwer 2016.

[47] Curtis T Rueden, Johannes Schindelin, Mark C Hiner, Barry E DeZonia, Alison E Walter, Ellen T Arena, and Kevin W Eliceiri. Imagej2: Imagej for the next generation of scientific image data. *BMC bioinformatics*, 18(1):529, 2017.

[48] Tim Mosmann. Rapid colorimetric assay for cellular growth and survival: application to proliferation and cytotoxicity assays. *Journal of immunological methods*, 65(1-2):55–63, 1983.

[49] Karl Buch, Tanja Peters, Thomas Nawroth, Markus Sänger, Heinz Schmidberger, and Peter Langguth. Determination of cell survival after irradiation via clonogenic assay versus multiple mtt assay-a comparative study. *Radiation oncology*, 7(1):1, 2012.

[50] Edwin M. Leidholdt John M. Boone Jerrold T. Bushberg, J.Anthony Seibert. *The Essential Physics of Medical Imaging-Third edition*. 2012.

[51] BIO RAD. *Model 680 Microplate Reader - Instruction Manual*.

[52] Frank Dolbeare. Bromodeoxyuridine: a diagnostic tool in biology and medicine, part i: Historical perspectives, histochemical methods and cell kinetics. *The Histochemical Journal*, 27(5):339–369, 1995.

[53] W.S.III Kiger, P.L. Micca, G.M Morris, and J.A. Coderre. Boron microquantification in oral mucosa and skin following administration of a neutron capture therapy agent. *Radiation Protection Dosimetry*, 99(1-4):409–412, 2002.

Ringraziamenti

Ringrazio prima di tutto la mia famiglia, per l'enorme sacrificio fatto, per il sostegno, per la stima, per i consigli e per le delizie romagnole che portavano su durante il figli-tour lombardo.

Ringrazio infinitamente Silva per l'enorme fiducia riposta in me, per la grande disponibilità e cortesia, per i tantissimi consigli (anche notturni), per l'enorme cura ed attenzione nei miei confronti, non solo lavorativa ma anche e soprattutto personale. Grazie per la grande professionalità, per avermi trasmesso la passione e l'entusiasmo nel lavoro e soprattutto nelle difficoltà che, ho imparato, aprono molte strade. Grazie per essere un vero Leader e una Persona vera.

Ringrazio altrettanto infinitamente Ian per l'incommensurabile pazienza, per la sua saggezza informatica (e non solo) a cui ho attinto innumerevoli volte, per l'enorme disponibilità e gentilezza, per l'interesse nei miei confronti sia lavorativo che personale. Grazie per la compagnia nei momenti di difficoltà, per aver condiviso con me la grande gioia del buon cibo, soprattutto durante il lockdown. Grazie per avermi accompagnato insieme a Silva in questo percorso.

Ringrazio Cinzia, Laura, Patrizia e Agostina per avermi accolto a braccia aperte nei loro laboratori e per avermi insegnato tanto su una materia così affascinante come la biologia. Grazie per la qualità del rapporto umano, per aver ascoltato tutti i miei dubbi e per avermi guidato con pazienza e disponibilità verso questo traguardo.

I would like to thank Dr. Sara J. Gonzalez because, even if we never met, she was always ready to give me valuable advice, especially on the dosimet-

ric and computational part of this work. Thank you for your kindness and helpfullness and for the trust placed in me.

Thank you very much to Eng. Juan Longhino for sharing his knowledge about the SSW/SSR strategy. Your advice allowed to complete the computational work in the best possible way.

Ringrazio Seta, per la sua salda sherpaggine, per le giornate passate ad ascoltare i miei dubbi e le mie delusioni, per avermeli sempre mostrati da un'altra interessante angolazione, accompagnandomi verso una scelta decisa e consapevole. Grazie per l'enorme compagnia e per avermi fatto riscoprire la bellezza del rugby.

Ringrazio Chiara per la sua gentilezza e disponibilità, per i consigli, per le chiacchierate e per la sua premura nei miei confronti.

Grazie a Marco per le lunghe chiacchierate interdisciplinari in laboratorio, per la gentilezza, per la sua grande passione per la scienza e la voglia di imparare sempre che mi hanno arricchito nei momenti passati insieme.

Grazie a Tom per avermi sempre capita, per la sua generosità e gentilezza. Grazie per la vera amicizia che è nata.

Grazie a Paola, Alice, Grace per essere state compagne di agonie e soddisfazioni.

Grazie a Michela ed Erika per essere state compagne di sventure e di appartamento, per le litigate costruttive, per l'aiuto, per la comprensione e per la compagnia, per le delizie culinarie della grande Puglia e per gli interessanti scambi di idee con sincera voglia di conoscere ed imparare. Grazie per la musica variopinta e per i "weee, che sta fascenn?" che riempivano inesorabilmente casa.

Ringrazio Dadi e la Rachi per avermi sempre accolto al mio ritorno in patria con sincero affetto, per tutti i giapponesi passati insieme e la vera amicizia tra noi.

Ringrazio Rambo, Ale, la Grace e l'Ali per la loro amicizia, per le serate che mi sono mancate tanto in questi anni, semplici, sincere e in compagnia.

Ringrazio la Iaia e l'Angy per le belle serate (anche a distanza), soprattutto per gli impossibili Sherlock durante il lockdown che mi hanno fatto compagnia.

Ultima, ma non ultima, grazie Francicara, perchè continui a sopportarmi, nonostante tutto, e a scegliermi ogni giorno, a modo tuo.